ABSTRACT

Title of Document: ENSEMBLE ASSIMILATION OF GLOBAL LARGE-SCALE PRECIPITATION

Guo-Yuan Lien, Doctor of Philosophy, 2014

Directed By: Professor Eugenia Kalnay,
Department of Atmospheric and Oceanic Science
Professor Takemasa Miyoshi,
Department of Atmospheric and Oceanic Science

Many attempts to assimilate precipitation observations in numerical models have been made, but they have resulted in little or no forecast improvement at the end of the precipitation assimilation. This is due to the nonlinearity of the model precipitation parameterization, the non-Gaussianity of precipitation variables, and the large and unknown model and observation errors.

In this study, we investigate the assimilation of global large-scale satellite precipitation using the local ensemble transform Kalman filter (LETKF). The LETKF does not require linearization of the model, and it can improve all model variables by giving higher weights in the analysis to ensemble members with better precipitation, so that the model will "remember" the assimilation changes during the forecasts. Gaussian transformations of precipitation are applied to both model background precipitation and observed precipitation, which not only makes the error distributions more Gaussian, but also removes the amplitude-dependent biases between the model

and the observations. In addition, several quality control criteria are designed to reject precipitation observations that are not useful for the assimilation.

Our ideas are tested in both an idealized system and a realistic system. In the former, observing system simulation experiments (OSSEs) are conducted with a simplified general circulation model; in the latter, the TRMM Multisatellite Precipitation Analysis (TMPA) data are assimilated into a low-resolution version of the NCEP Global Forecasting System (GFS). Positive results are obtained in both systems, showing that both the analyses and the 5-day forecasts are improved by the effective assimilation of precipitation. We also demonstrate how to use the ensemble forecast sensitivity to observations (EFSO) to analyze the effectiveness of precipitation assimilation and provide guidance for determining appropriate quality control. These results are very promising for the direct assimilation of satellite precipitation data in numerical weather prediction models, especially with the forthcoming Global Precipitation Measurement (GPM) sensors.

ENSEMBLE ASSIMILATION OF GLOBAL LARGE-SCALE PRECIPITATION

By

Guo-Yuan Lien

Dissertation submitted to the Faculty of the Graduate School of the
University of Maryland, College Park, in partial fulfillment
of the requirements for the degree of
Doctor of Philosophy
2014

Advisory Committee:
Professor Eugenia Kalnay, Chair/Advisor
Professor Takemasa Miyoshi, Co-Advisor
Professor James Carton
Professor Brian Hunt
Professor Kayo Ide

Acknowledgements

There are a number of people to whom I am greatly indebted.

First of all, I would like to express the deepest appreciation to Prof. Eugenia Kalnay and Prof. Takemasa Miyoshi for their continuous advising and support during my entire Ph.D. study. They always give me invaluable guidance, warm encouragement, and much freedom of exploring every interesting topic.

I would like to express my sincere gratitude to my committee members, Prof. James Carton, Prof. Brian Hunt, and Prof. Kayo Ide, for providing insightful comments on my dissertation.

I would particularly like to thank Dr. George Huffman for his precious guidance on the TMPA dataset. I would also like to deeply thank Dr. Daryl Kleist, Dr. Runhua Yang, and Dr. Henry Juang for their generous support on many details of the GFS model. Special thanks also to Tetsuro Miyachi who ported the GFS model to our Linux cluster in the department. Moreover, I truly appreciate Yoichiro Ota and Daisuke Hotta for providing their EFSO code.

I would also thank the funding agencies, NASA, NOAA, and the National Oceanographic Partnership Program (NOPP). I particularly thank to NASA for offering the usage of the Discover supercomputer on which most of the GFS-LETKF experiments have been conducted.

Finally, and most importantly, I owe my deepest gratitude to my parents, Chun Lu and Wen-Hua Lien. Without them, my graduate study in a foreign country would not have been possible. Also, thanks to this Earth, and people living atop.

Table of Contents

List of Tables

List of Figures

Chapter 1: Introduction

1.1 Review of assimilation of precipitation

Precipitation has long been one of the most important and useful meteorological quantities to observe. The traditional rain gauge measurement of precipitation can be traced back to the 19th century before the rawinsonde network was established (e.g., Jones and Bradley 1992). In recent years, more advanced precipitation estimations from a variety of remote sensing platforms, such as satellite and ground-based precipitation radar, have also become available. For example, the Tropical Rainfall Measuring Mission (TRMM) has been used to produce a set of high-quality, high-resolution global (50S–50N) precipitation estimates (Huffman et al. 2007) that have been widely used in many research areas. The Global Precipitation Measurement (GPM; Hou et al. 2008) mission is scheduled for launch in 2014 as the successor to TRMM. Because of the large impact that effective assimilation of precipitation could have in forecasting severe weather, many efforts to assimilate precipitation observations have been made (Bauer et al. 2011).

Both nudging and variational methods have been used previously to assimilate precipitation by modifying the model's moisture and sometimes temperature profiles as well, in order to either enhance or reduce short-term precipitation according to the model parameterization of rain (e.g., Tsuyuki 1996, 1997; Falkovich et al. 2000; Davolio and Buzzi 2004; Koizumi et al. 2005; Mesinger et al. 2006). They are generally successful in forcing the forecasts of precipitation to be close to the observed precipitation during the assimilation, but the resulting forecast perturbations

quickly decay when assimilation stops. For example, a nudging method was applied to the North American Regional Reanalysis (NARR), and achieved the objective of making the Eta NARR 3 hour forecasts essentially identical to the observed precipitation used to nudge the model (Mesinger et al. 2006). However, the Eta forecasts from the NARR were not superior to the operational forecasts beyond a few hours. Nudging the moisture was not effective presumably because it is not an efficient way to update the potential vorticity field, which is the "master" dynamical variable that primarily determines the evolution of the forecast in numerical weather prediction (NWP) models.

There are other important issues for precipitation assimilation in the variational framework. Precipitation processes parameterized by the model physics are usually very nonlinear and even discontinuous at some "thresholds" (Zupanski and Mesinger 1995). Therefore, it is problematic to create and use the linearized version of the forward model as required in the 4D-Var assimilation of precipitation variables (Errico et al. 2007). An inaccurate tangent linear model and adjoint model would yield a poor estimate of the evolution of finite perturbations and degrade the 4D-Var analyses. Considerable efforts have been made on improving the model's moist physics in order to improve the assimilation of precipitation remotely sensed by satellite or radar (e.g., Treadon et al. 2003; Li and Mecikalski 2010, 2012). Alternative moist physical parameterization schemes that are more linear and continuous have been used to reduce the nonlinearity problem (e.g., Zupanski and Mesinger 1995; Lopez and Moreau 2005). In addition, it is difficult to use the fixed (climatological) background error covariance to describe the relationship between

precipitation and other state variables, thus the dynamical variables may not be optimally updated. These problems lead to a widely shared experience that forecasts starting from analyses with precipitation assimilation lose their extra skill in forecasts of precipitation or other dynamical variables after just a few forecast hours (e.g., Tsuyuki and Miyoshi 2007; Davolio and Buzzi 2004; Errico et al. 2007). One notable exception is Hou et al. (2004) who used forecast tendency corrections of temperature and moisture as control variables in variational data assimilation in the assimilation of hurricane observed precipitation. They were able to show that large changes in precipitation had long-lasting positive impacts on a hurricane forecast, presumably because the release of latent heat corrected the potential vorticity.

There are even more difficulties associated the characteristics of the precipitation variable itself in both models and observations. First, the highly non-Gaussian distribution of the precipitation observations seriously violates the basic assumption of normal error statistics made in most data assimilation schemes. Transformations such as a logarithmic transformation have been applied to the precipitation assimilation (e.g., Hou et al. 2004; Lopez 2011, 2013) in order to overcome this issue. Although the logarithmic transformation is expected to alleviate the non-Gaussianity of positive precipitation, it is not necessarily optimal. Besides, the precipitation variable contains a great portion of zero values, which also leads to a major challenge. In the variational methods, there is often no sensitivity (i.e., the Jacobian of the observation operator is zero) where the observable is zero (Errico et al. 2007). Past studies have shown that it is very difficult to achieve improvement by assimilation of zero precipitation observations in the usually used methods (e.g., Tsuyuki and

Miyoshi 2007). However, as shown in Weygandt et al. (2008), the forced suppression of convection in areas with no radar echoes did show the importance of zero precipitation observations in correctly analyzing a convection system. Therefore, a proper use of zero precipitation data would be a very important task. Furthermore, the forward model errors mainly associated with the moist physical parameterizations and the observation errors may be large. The error characteristics in the retrieval products are almost unknown. All of these issues add to the difficulties of the precipitation assimilation in the realistic NWP configuration. For more details, Errico et al. (2007) provided a comprehensive review of the issues regarding the cloud and precipitation assimilation, and Bauer et al. (2011) reviewed the current status of precipitation assimilation in the modern NWP models.

1.2 Objectives

In this study, we propose to use the ensemble Kalman filter (EnKF) method to address some critical issues regarding the precipitation assimilation. Since the EnKF method does not require linearization of the model or any other modifications of the model physics as required in variational methods, we can thus get rid of the complex linearization problem and use the original moist physical for precipitation assimilation. Further, with the ensemble approach, an accurate precipitation parameterization should result in useful error covariances between the diagnostic precipitation and the other prognostic variables, so it should be able to more efficiently change the potential vorticity field and thus improve the longer-term model forecasts. Several pioneering experiments of precipitation assimilation using

the EnKF methods have already been conducted (Miyoshi and Aranami 2006; Zupanski et al. 2011; Zhang et al. 2013) with somewhat encouraging results.

For the non-Gaussianity issue, we propose to use a general variable transformation algorithm (i.e., Gaussian anamorphosis; Wackernagel 2003) to replace the traditional logarithm transformation. This method can transform any continuously distributed variable into a Gaussian distribution based on its empirical (climatological) distribution. In addition, we propose a new "quality control" criterion to accept observations based only on the model background. With this criterion, the precipitation observations are assimilated when there are enough background ensemble members having positive precipitation, regardless of the observed values. Therefore, it is possible to make use of some zero precipitation observations during the assimilation.

To test the above ideas, we first conduct precipitation assimilation experiments using a simpler system. The experiments are conducted within an identical-twin observing system simulation experiment (OSSE) framework, and a simplified but still realistic global circulation model (GCM), the Simplified Parametrizations, primitivE-Equation DYnamics (SPEEDY) model (Molteni 2003), is used. It is worth emphasizing that when we previously used the same OSSE framework, but without introducing the Gaussian transformation of precipitation and the new criterion for precipitation assimilation, analysis and forecast errors became significantly larger when precipitation was assimilated. Therefore, a success demonstration of precipitation assimilation with this simple system will be an essential first step before applying our ideas to more complicated systems.

After carrying out our proof of concept with the idealized settings, we decide to conduct similar precipitation experiments with a more realistic configuration. In this part of study, the TRMM Multisatellite Precipitation Analysis (TMPA) data are assimilated into a low-resolution version of the National Centers for Environmental Prediction (NCEP) Global Forecasting System (GFS). With the realistic model and real observations, more challenges emerge, such as the large model errors and the unknown observation error statistics. As a result, it becomes be much more difficult to obtain positive impacts by precipitation assimilation in this configuration. A detailed discussion about the challenges and possible solutions with the real model and observations will be provided in Chapter 5. We compute several statistics of precipitation from the point of view of data assimilation to investigate these issues. With these challenges and limitations in mind, the assimilation of global large-scale precipitation in a realistic model is demonstrated. Finally, a powerful tool, the ensemble forecast sensitivity to observations (EFSO; Kalnay et al. 2012; Ota et al. 2013), is applied to the precipitation assimilation, which allows us to discuss the problems form different aspects.

1.3 LETKF

In this study, we use the Local Ensemble Transform Kalman Filter (LETKF; Hunt et al. 2007) to perform the precipitation assimilation. The LETKF is a flavor of EnKF scheme that performs most of the analysis computations in ensemble space and in a local domain around each grid point. An EnKF finds an optimal analysis in a "subspace" of the forecasts in local regions (depending on the localization settings). For example, if a member produces a (locally) better precipitation field in the

background forecast compared to the observations, it will be (locally) weighted more in creating the ensemble mean analysis. The "weight" is calculated explicitly in the ensemble transform Kalman filter (ETKF) and as detailed below in the LETKF, but this interpretation is also valid in other ensemble data assimilation schemes such as the ensemble square-root filter (EnSRF) where the computation of the weights is implicit. As all other ensemble data assimilation schemes, the LETKF flow-dependent background error covariance $\mathbf{P}^b$ is inferred from the sample covariance among ensemble members. The background error covariance can be written as

$$\mathbf{P}^b = \frac{1}{K-1}\,\mathbf{X}^b(\mathbf{X}^b)^T\,, \tag{1.1}$$

where $\mathbf{X}^b = \left[\mathbf{x}^{b(1)} - \bar{\mathbf{x}}^b, \ldots, \mathbf{x}^{b(K)} - \bar{\mathbf{x}}^b\right]$ is the matrix whose columns are background ensemble perturbations (i.e., the departure of members from the ensemble mean), and K is the ensemble size. The dimension of $\mathbf{P}^b$ is exceedingly large in modern NWP models, thus it is not computed explicitly. Instead, when performing the LETKF analysis, $\tilde{\mathbf{P}}^a$, the analysis covariance *in ensemble space* is computed first (Hunt et al. 2007):

$$\tilde{\mathbf{P}}^a = [(K-1)\,\mathbf{I} + (\mathbf{Y}^b)^T\mathbf{R}^{-1}\,\mathbf{Y}^b]^{-1}\,. \tag{1.2}$$

After that, the mean weight vector $\bar{\mathbf{w}}^a$ and the weight matrix for the ensemble perturbation $\mathbf{W}^a$ are computed from:

$$\bar{\mathbf{w}}^a = \tilde{\mathbf{P}}^a\,(\mathbf{Y}^b)^T\mathbf{R}^{-1}(\mathbf{y}^o - \bar{\mathbf{y}}^b)\,, \tag{1.3}$$

$$\mathbf{W}^a = \left[(K-1)\,\tilde{\mathbf{P}}^a\right]^{1/2}, \tag{1.4}$$

where $\mathbf{Y}^b = \left[\mathbf{y}^{b(1)} - \bar{\mathbf{y}}^b, \ldots, \mathbf{y}^{b(K)} - \bar{\mathbf{y}}^b\right]$ is the matrix that consists of columns of background observation perturbations, $\mathbf{R}$ is the observation error covariance, and $\mathbf{y}^o$ is

the observation. The background (forecast) observation values are calculated through the observation operator: $\mathbf{y}^{b(i)} = H\left(\mathbf{x}^{b(i)}\right)$. Finally, the analysis ensemble mean and perturbations can be computed by applying the weights to the background ensemble:

$$\bar{\mathbf{x}}^a = \bar{\mathbf{x}}^b + \mathbf{X}^b \, \bar{\mathbf{w}}^a \,, \tag{1.5}$$

$$\mathbf{X}^a = \mathbf{X}^b \, \mathbf{W}^a \,. \tag{1.6}$$

In the LETKF, Equations (1.2)–(1.6) are computed locally for every model grid point with its nearby observations, which allows easy implementation of covariance localization and parallelization (Hunt et al. 2007). A computationally efficient code for the LETKF is available at the public Google Code platform from Miyoshi (http://code.google.com/p/miyoshi/), including the SPEEDY-LETKF system that couples the SPEEDY model with the LETKF codes.

1.4 Outline of this thesis

The dissertation is organized as follows. The methodology, including the Gaussian transformation and the special treatment of zero precipitation observations, are introduced in Chapter 2. Chapter 3 presents the results of the perfect-model OSSEs with the SPEEDY model and summarizes what we learn from the proof-of-concept experiments. Chapter 4 describes the development of the GFS-LETKF system in preparation for the real precipitation assimilation. Chapters 5–7 are three parts of the real precipitation assimilation experiments. In the part I (Chapter 5), the satellite precipitation dataset used in this study is introduced. Several statistical results of the precipitation variable between the model and the observations are presented to generally discuss the challenges and possible solutions of the real precipitation

assimilation. The part II (Chapter 6) presents a set of experiments showing positive impacts by assimilating real satellite precipitation data into the GFS model. The part III (Chapter 7) demonstrates how to use EFSO to provide guidance for determining appropriate quality control. The summary and future directions are provided in Chapter 8.

Chapter 2: Transformation of precipitation

2.1 Introduction

Most of data assimilation schemes, including the variational method and the EnKF method, assume Gaussian error distributions for both observations and the model backgrounds. If the error distribution is not Gaussian, the analysis could be not optimal. However, it is unavoidable that we need to use observations with a certain non-Gaussianity in the geophysical data assimilation. In particular, the precipitation-related variables are often very non-Gaussian. It becomes a severe problem when those variables are assimilated.

Bocquet et al. (2010) provided a comprehensive review of the methods to deal with the non-Gaussianity in various data assimilation schemes. The approaches that do not require Gaussian variables, such as the particle filter (van Leeuwen 2009), the maximum entropy method (Eyink and Kim 2006), and the rank histogram filter (Anderson 2010), are generally too expensive. Therefore, these methods have only been applied and tested with simpler systems. On the other hand, a much cheaper and feasible solution would be to do a variable transformation. When non-Gaussian observations are being assimilated, an appropriate transformation of observables can make the error more Gaussian with only a small additional cost. Either analytical or empirical formula can be used for the transformation. In this chapter, we will describe several transformations for precipitation assimilation, including the widely used logarithm transformation, and the Gaussian anamorphosis method we propose to use. In addition, the fact that precipitation can have zero value adds much complexity to

the problem. Several choices to deal with the zero precipitation value will also be discussed.

2.2 Logarithm transformation for the precipitation assimilation

The logarithm transformation

$$\tilde{y} = \ln(y + \alpha) \tag{2.1}$$

has been widely used in the precipitation assimilation. In the equation, y is original variable, $\tilde{y}$ is the transformed variable, and α is an arbitrary constant. The constant α is added to prevent the singularity at zero precipitation ($y = 0$). This constant can be tuned to optimize the results according to the specific problems, and is suggested to be 1 mm in Mahfouf et al. (2007). Using this transformation, Lopez (2011) successfully assimilated the NCEP stage IV precipitation analysis over the eastern United States, and Lopez (2013) presented experimental results of assimilation of the 6-hourly accumulated precipitation observations measured by the rain gauges at synoptic stations.

The logarithm transformation enhances the discrimination of small precipitation amounts, and damping the contribution of large precipitation amount, leading to a modification of the dynamical range (Mahfouf et al. 2007). It is also a sound choice if we assume that the magnitude of precipitation errors varies as a power law of the precipitation amount (Bauer et al. 2002), and the error distribution is close to a log-normal distribution (Errico et al. 2001). Therefore, we can reasonably assign a constant observation error for precipitation observations in the transformed space,

which is approximately valid when the original error is proportional to the precipitation amount.

2.3 Gaussian anamorphosis

The analytical transformation such the logarithm transformation [Equation (2.1)] is simple, but it is not guaranteed to be useful if the error associated with precipitation does not follow a log-normal distribution. It may be a good transformation for precipitation in some regions, seasons, or precipitation types, but a globally invariant analytical transformation may not be applicable to every case. Therefore, we choose an alternative method to define empirical transformations based on samples. A usual way to define these transformations (or "anamorphosis functions") is through the connection between the two cumulative distribution functions (CDFs) of the original variable (y) and the transformed variable ($\tilde{y}$):

$$\tilde{F}(\tilde{y}) = F(y) \text{ , or} \tag{2.2}$$

$$\tilde{y} = \tilde{F}^{-1}[F(y)] \text{ ,} \tag{2.3}$$

where F is the CDF of y, $\tilde{F}$ is the CDF of $\tilde{y}$, and $\tilde{F}^{-1}$ is the inverse function of $\tilde{F}$. By definition, the CDFs are bounded in $[0, 1]$. The CDF of the original variable (F) needs to be empirically determined from samples, and the CDF of the transformed variable ($\tilde{F}$) can be arbitrarily chosen so that the transformed variable can have any desired distribution. When we choose

$$\tilde{F}(\tilde{y}) = F^{G}(\tilde{y}) = \frac{1}{2}\left[1 + \text{erf}\left(\frac{\tilde{y}}{\sqrt{2}}\right)\right] \text{ ,} \tag{2.4}$$

which is the CDF of a standard normal distribution with zero mean and unit variance so that

$$F^{G^{-1}}(P) = \sqrt{2}\,\mathrm{erf}^{-1}(2P-1)\,, \tag{2.5}$$

it becomes an "Gaussian anamorphosis" (Wackernagel 2003):

$$\tilde{y} = F^{G^{-1}}[F(y)]\,. \tag{2.6}$$

In this way, the transformed variable ($\tilde{y}$) becomes a Gaussian variable. The use of the Gaussian anamorphosis has appeared in several geophysical data assimilation studies (e.g., Simon and Bertino 2009, 2012; Schöniger et al. 2012). We call this method "Gaussian transformation" (GT) hereafter in this dissertation.

An illustration of the Gaussian transformation of precipitation is shown in Figure 2.1. Figure 2.1a shows a typical probability density function (PDF) of precipitation, which is very non-Gaussian and contains a great portion of zero values that can be regarded as a delta function at zero. Figure 2.1c is the corresponding cumulative distribution of the precipitation PDF. Using the inverse CDF of the standard normal distribution $F^{G^{-1}}$, the cumulative probability value is converted back to the transformed variable $\tilde{y}$, whose CDF shown in Figure 2.1d and PDF in Figure 2.1b. Note that the transformation ensures a simple one-to-one relationship between the original variable and the transformed variable if their CDFs are *continuous*. However, it is apparent that the precipitation is not a continuous variable since it contains a large portion of zero values so that the CDF is discontinuous at zero. In the illustration, the dashed parts of lines in Figure 2.1b, c, and d are associated with those zero precipitation values. This issue regarding zero precipitation will be addressed and the figure will be further discussed in Chapter 2.5. Note that multimodal distributions would not pose any difficulty in defining the transformation.

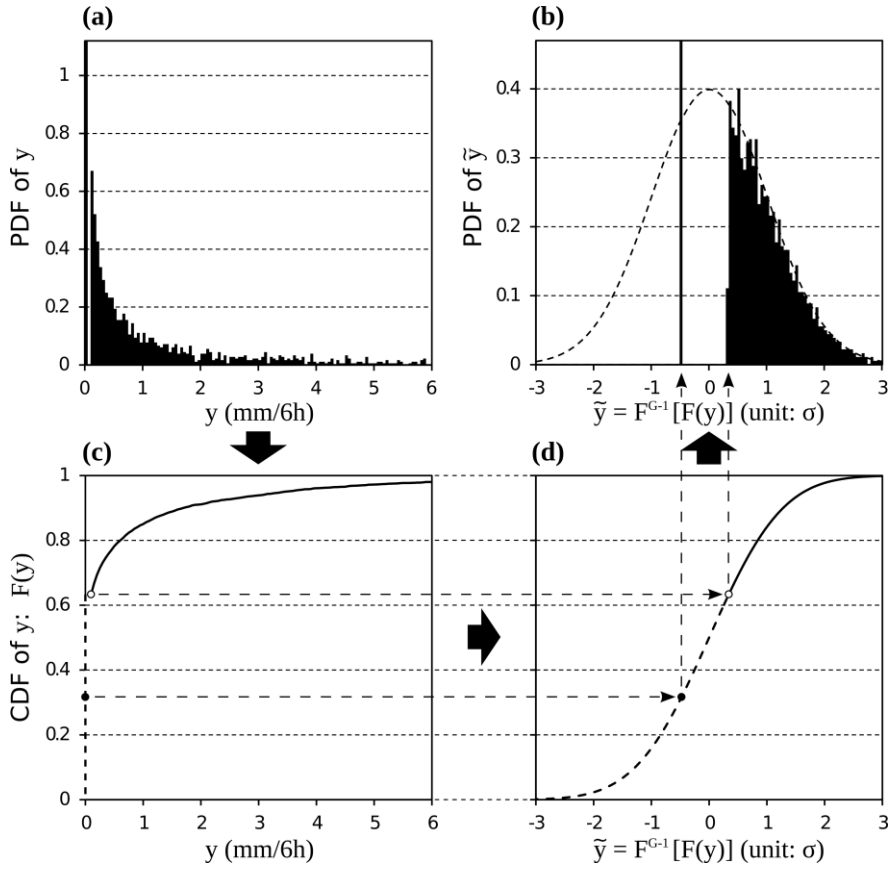

Figure 2.1: At a random grid point, the probability density function and cumulative distribution function of (a), (c) the original precipitation and (b), (d) the transformed precipitation based on the 10-year model climatology. The procedure of the Gaussian transformation is from (a) to (c), to (d), and to (b) as indicated by the arrows. The transformation of zero values is illustrated using dashed lines, which uses the "climatological median" method (CZ; see Section 2.5.1).

In this transformation method, the transformation of the extreme values needs to be specifically defined. If the value to be transformed is larger or smaller than all sample values used to construct the empirical CDF, there is a problem. In particular, $F^{G^{-1}}$ will transform zero and one to $-\infty$ and $+\infty$ respectively, which is also not

acceptable. Simon and Bertino (2012) indicated that using the tails of the distribution during the transformation can be a risk, and they proposed to use linear tails. In our study, since we will use large samples to construct the empirical CDF of precipitation, we choose a simpler way: all precipitation values with cumulative distribution less than 0.001 and greater than 0.999 are set to the values 0.001 and 0.999, respectively. Consequently, when the original values fall outside this range, they will be transformed to -3.09 and 3.09.

It is worth mentioning that this CDF-based transformation of precipitation has been used in some climate studies, though they are not related to the data assimilation. For example, the Standardized Precipitation Index (SPI) (McKee et al. 1993; Guttman 1999) commonly used to study drought is defined based on a similar method, while the time scale of precipitation accumulations they have focused is much larger than the 6 hours used in the data assimilation.

Last but not least, when we define the empirical CDF based on the climatological samples from models or observations, this method transforms the climatological distribution of the original variable into a Gaussian distribution as a whole, but not its error distribution at every estimate. Unfortunately, it would be impossible to define the transformation for every estimate because no enough samples can be obtained in this case. As a result, using the climatological samples would be the only practicable choice. Nevertheless, we think this method is still beneficial to the EnKF data assimilation, by assuming that *the error distributions from a variable with more Gaussian climatological distribution will also be more Gaussian*. The validity of this assumption is conceptually explored in Figure 2.2. The gray shaded area is the

climatological distribution. When we take an estimate in a random observation time and location, suppose the error distribution of this estimate is Gaussian (the orange line), then the actual error distribution will also be Gaussian (the red line) because the product of two Gaussian distributions is also a Gaussian distribution. Therefore, we believe that for a usual variable with continuous climatological distribution, this assumption is generally valid. Later in Chapter 5.4, we will use samples of the background ensembles generated from a realistic model to further verify the validity of this assumption.

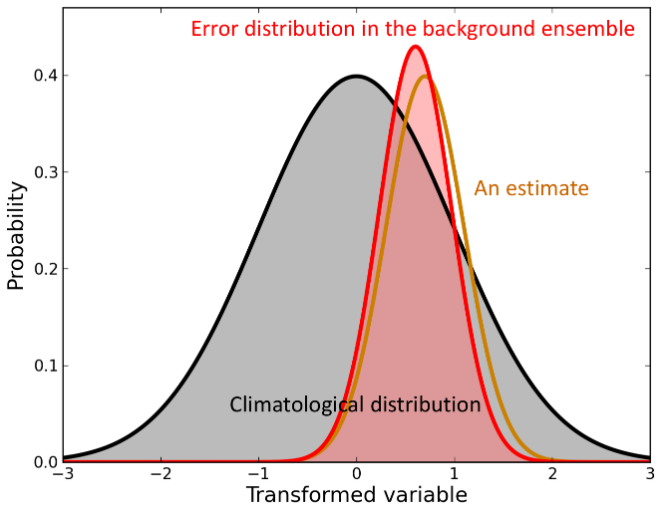

Figure 2.2: The probability density functions of the climatological distribution and the background error distribution at a random grid point and time.

2.4 Implementation with the LETKF

Once the transformation is defined, it is very easy to implement with the LETKF. Assume that the transformation used is $\tilde{y} = T[y]$, where $T[\,]$ can be either the logarithm transformation [Equation (2.1)] or the Gaussian transformation [Equation

(2.6)]. In the data assimilation calculation, the precipitation observations $\mathbf{y}_{(\mathrm{pp})}^{o}$ are replaced by the transformed observations:

$$\tilde{\mathbf{y}}_{(\mathrm{pp})}^{o} = T\left[\mathbf{y}_{(\mathrm{pp})}^{o}\right]. \tag{2.7}$$

Meanwhile, the transformation is also applied to the precipitation values in the model background:

$$\tilde{\mathbf{y}}_{(\mathrm{pp})}^{b} = T\left[\mathbf{y}_{(\mathrm{pp})}^{b}\right] = T[H(\mathbf{x}^{b})] = \tilde{H}(\mathbf{x}^{b}), \quad \tilde{H} = T \circ H, \tag{2.8}$$

thus it can be included in the observation operator H ($\circ$ stands for the function composition).

2.5 Treatment of zero precipitation

As mentioned in Chapter 2.3, there is an issue regarding the transformation of the zero precipitation values. It is actually a very critical problem because the probability of zero precipitation can amount to more than 50-80% in many datasets. A naïve approach would be to only transform the non-zero part of precipitation data. However, this is not practical in data assimilation because even if all zero precipitation observations are discarded, it is still possible to have zero values at the corresponding observation location in the background forecasts, which still need to be transformed before they are passed into the assimilation calculation. In ensemble data assimilation framework, this problem is even more apparent than in variational data assimilation since it is very likely that a random ensemble member would have zero precipitation at an observation location. Therefore, a heuristic solution to the transform of zero precipitation values is necessary.

Before introducing the solutions of the zero precipitation assimilation, a value, y_{trace}, meaning a measurable trace of precipitation, is defined here. In practice, we may regard those very tiny non-zero precipitation values in the model outputs or satellite retrievals as meaningless precipitation amounts; therefore, a condition is first imposed to the original precipitation values:

$$y \leftarrow \begin{cases} 0, & if\ y < y_{\text{trace}} \\ y, & if\ y \geq y_{\text{trace}} \end{cases}. \tag{2.9}$$

A proper choice of this value can improve the data assimilation results, since it removes the impact of meaningless tiny values. However, a value of y_{trace} that is too large would diminish the useful information contained in the small precipitation amounts.

2.5.1 Method 1: Climatological median

The zero precipitation is manifested as a delta function in the probability distribution (Figure 2.1a). Since any deterministic transformation of a delta function will still result in a delta function, it is be impossible to expand it into a continuous distribution and form a perfect Gaussian distribution in the transformed space by any deterministic method. Instead, we need to decide a specific value in the transformed variable to that all zero precipitation values are transformed. In other words, a value of cumulative probability $F(y)$ for zero precipitation ($y = 0$) needs to be assigned.

The first method is called "climatological median" of zeros (CZ). In this method, $F(0)$ is assigned to be the middle value of the zero precipitation cumulative probability:

$$F(0) = \frac{1}{2}P_c \tag{2.10}$$

$$\text{so that } \tilde{y}_{\text{zero}} = F^{G^{-1}}[F(0)] = F^{G^{-1}}\left(\frac{P_c}{2}\right), \tag{2.11}$$

where $P_c = F(y_{\text{trace}})$ is the zero precipitation probability in the climatology. This method has been illustrated in Figure 2.1. In this example, the probability of zero precipitation is about 63.4% (CDF = 0.634 for y_{trace}; open circles in Figure 2.1c and d), thus $F(0) = 0.317$ is assigned for all zero precipitation (solid circles) at that grid point. By this way, the zero precipitation in the transformed variable is still a delta function in its PDF (Figure 2.1b), but it is located at the *median* of the zero precipitation part of the normal distribution. Therefore, though not perfectly Gaussian, it is more reasonable than the original skewed distribution[1].

2.5.2 Method 2: Background median

On further thinking, this fixed transformation of zero precipitation determined from the climatological zero precipitation probability may not be a good solution. As illustrated in Figure 2.3a, when the boundary of positive precipitation and zero precipitation exists, the "real" background error distribution (red Gaussian curve) can cross this boundary, result in a distribution that only the positive precipitation part (red shaded area; right side to the boundary) is fitted into the Gaussian envelope while

[1] This approach to transforming zero precipitation does not maintain the properties of zero mean and unit standard deviation. However, this does not create problem in the data assimilation because such properties are essentially not required in the climatological

the zero precipitation part remains undetermined. We note the similarity of the gray shaded area and the red shaded area: they are both "parts of the Gaussian distribution", but the ratios of the zero precipitation areas to the whole Gaussian areas are different. In the CZ method, we determine the value of the transformed zero precipitation based on the gray shaded area; here we propose an algorithm called "background median" of zeros (BZ), in which we determine the value of transformed zero precipitation based on the red shaded area instead of the gray shaded area. We will also assign the zero precipitation to the median of the zero precipitation probability under the red Gaussian curve (red vertical thick line in Figure 2.3b), but now this probability is determined from the *background ensemble* (i.e., the number of the non-precipitating background ensemble members divided by the total member number), not the climatology. Since the red shaded area (real error distribution determined from the background members) is not fixed every time, the transformation of the zero precipitation using this BZ method will also be changing in every LETKF analysis time.

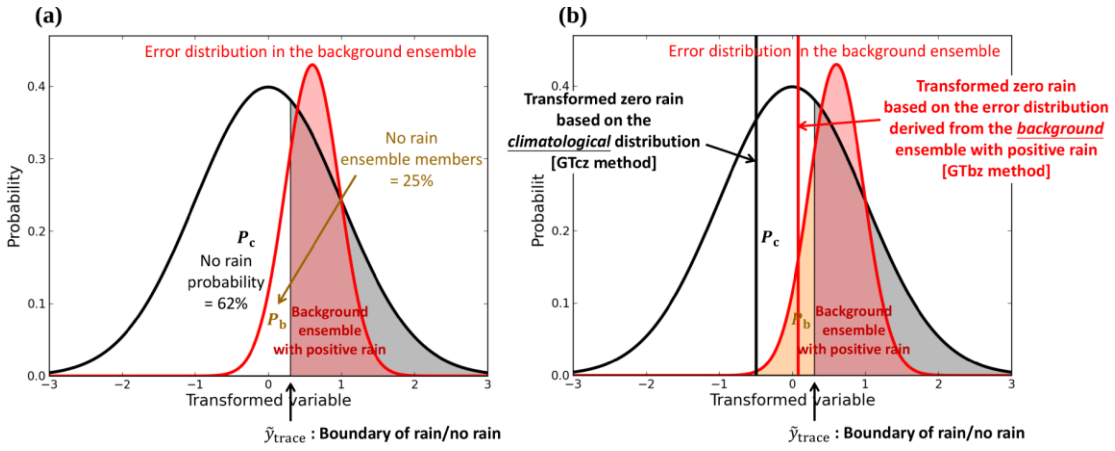

Figure 2.3: (a) The relation between the boundary of zero precipitation and positive precipitation (y_{trace}) and the zero precipitation probability in the climatology (P_{c}) and in the background ensemble (P_{b}). (b) The median of the zero precipitation probability in the climatology (black thick vertical line) and in the background ensemble (red thick vertical line).

Based on the concept expressed above, the new formulation of the zero precipitation transformation is derived as follows. As shown in Figure 2.3, the boundary of positive and zero precipitation is associated with two probability distributions, the climatological distribution and the background error distribution, through the zero precipitation probability in the climatology and in the background ensemble, respectively. Here we state again that both these two distributions are assumed to be Gaussian, where the climatological one is known but the one representing the background error distribution is unknown. Therefore, we can write the first equality in the form of inverse CDFs of normal distributions:

$$\tilde{y}_{\mathrm{trace}} = F^{G^{-1}}(P_{\mathrm{c}}) = F^{G'^{-1}}(P_{\mathrm{b}}) \,, \tag{2.12}$$

where $\tilde{y}_{\text{trace}}$ is the trace value of precipitation [i.e., the boundary of positive and zero precipitation; its original value, y_{trace}, is 0.1 mm $(6\text{h})^{-1}$ in our SEPPDY model experiments and 0.06 mm $(6\text{h})^{-1}$ in our GFS model experiments] in the transformed variable, $F^{G^{-1}}$ is the inverse CDF of a normal distribution with zero mean and unit standard deviation as we defined in Equation (2.5), and $F^{G'^{-1}}$ is the inverse CDF of an unknown normal distribution. $P_{\text{c}} = F(y_{\text{trace}})$ is the zero precipitation probability determined from the climatology; P_{b} is the zero precipitation probability determined from the background ensemble:

$$P_{\text{b}} = \frac{(\textit{number of background members with zero precipitation})}{(\textit{ensemble size})} . \qquad (2.13)$$

Assuming the unknown normal distribution representing the background error distribution has a mean $\bar{y}$ and a standard deviation σ so that $F^{G'^{-1}}(P_{\text{b}}) = \bar{y} + \sigma F^{G^{-1}}(P_{\text{b}})$, the Equation (2.12) becomes:

$$\tilde{y}_{\text{trace}} = F^{G^{-1}}(P_{\text{c}}) = \bar{y} + \sigma F^{G^{-1}}(P_{\text{b}}) . \qquad (2.14)$$

If we can solve these two unknown variables ($\bar{y}$ and σ), then we can determine the hypothesized background error distribution and therefore define the zero precipitation transformation by

$$\tilde{y}_{\text{zero}} = \bar{y} + \sigma F^{G^{-1}}\left(\frac{P_{\text{b}}}{2}\right) , \qquad (2.15)$$

the median of the zero precipitation probability in the background ensemble.

To solve these two unknowns, we construct the second equality through the expected value of the background error distribution. The expected values of the zero precipitation part and the positive precipitation part of the background error

distribution must be combined to form the expected value of the entire distribution, which is $\bar{y}$:

$$P_{\mathrm{b}}E[\tilde{y};\tilde{y}<\tilde{y}_{\mathrm{trace}}]+(1-P_{\mathrm{b}})E[\tilde{y};\tilde{y}\geq\tilde{y}_{\mathrm{trace}}]=\bar{y}\,. \tag{2.16}$$

, where $E[\,]$ means expected values. Assuming an exact Gaussian distribution for the zero precipitation part, the analytical representation of the $P_{\mathrm{b}}E[\tilde{y};\tilde{y}<\tilde{y}_{\mathrm{trace}}]$ is:

$$P_{\mathrm{b}}E[\tilde{y};\tilde{y}<\tilde{y}_{\mathrm{trace}}]=P_{\mathrm{b}}\bar{y}+\sigma\int_{-\infty}^{F^{G^{-1}}(P_{\mathrm{b}})}y\phi(y)dy\;,\;\;\phi(y)=\frac{e^{-\frac{y^2}{2}}}{\sqrt{2\pi}}\,. \tag{2.17}$$

On the other hand, the $(1-P_{\mathrm{b}})E[\tilde{y};\tilde{y}\geq\tilde{y}_{\mathrm{trace}}]$ term is computed using the discrete background ensemble members having positive precipitation, during the LETKF assimilation computation:

$$(1-P_{\mathrm{b}})E[\tilde{y};\tilde{y}\geq\tilde{y}_{\mathrm{trace}}]=\frac{1}{N}\sum_{i=n_1+1}^{N}\tilde{y}_i\;, \tag{2.18}$$

where N is the ensemble size and n_1 is the number of ensemble members with zero precipitation, assuming the member indices have been sorted in ascending order in terms of the precipitation values. Finally, we can represent the Equation (2.16) as:

$$P_{\mathrm{b}}\bar{y}+\sigma\alpha+\beta=\bar{y}\,, \tag{2.19}$$

$$\text{where }\alpha=\int_{-\infty}^{F^{G^{-1}}(P_{\mathrm{b}})}y\phi(y)dy=-\phi\left[F^{G^{-1}}(P_{\mathrm{b}})\right]\;,\;\;\beta=\frac{1}{N}\sum_{i=n_1+1}^{N}y_i\;. \tag{2.20}$$

From Equations (2.14) and (2.19), we can solve $\bar{y}$ and σ:

$$\bar{y}=\frac{\alpha\tilde{y}_{\mathrm{trace}}+\beta F^{G^{-1}}(P_{\mathrm{b}})}{\alpha+(1-P_{\mathrm{b}})F^{G^{-1}}(P_{\mathrm{b}})}\text{ , and} \tag{2.21}$$

$$\sigma=\frac{(1-P_{\mathrm{b}})\tilde{y}_{\mathrm{trace}}-\beta}{\alpha+(1-P_{\mathrm{b}})F^{G^{-1}}(P_{\mathrm{b}})}\,. \tag{2.22}$$

Plugging in these two values into Equation (2.15), we thus obtain the value to that zero precipitation should be transformed in this BZ method.

It is noted that this new formulation of the zero precipitation transformation will be ill-posed when the number of the positive precipitation members is too small. In particular, when there are no positive precipitation members, it is impossible to determine the zero precipitation transformation based on this method. However, later we will introduce a criterion that the precipitation observation is assimilated only when there are enough positive precipitation members in the background. By using this criterion the problem is automatically prevented. Another advantage of the BZ method is that the transformed value of the zero precipitation ($\tilde{y}_{\text{zero}}$) is always closer to the trace precipitation ($\tilde{y}_{\text{trace}}$), and it is even closer when there are more background members having positive precipitation.

2.5.3 Method 3: Random transformation

We may also propose a probabilistic method to transform the zero precipitation in order to expand the delta function into a continuous distribution; i.e., $F(0)$ is assigned to be a random value from a uniform distribution:

$$\tilde{y}_{\text{zero}} = F^{G^{-1}}(X)\ ,\ \ X \sim \mathcal{U}(0, P_{\text{c}})\ , \tag{2.23}$$

where $\mathcal{U}(0, P_{\text{c}})$ stands for a uniform distribution from 0 to P_{c}, the zero precipitation probability in the climatology. By this way, the zero precipitation part of the transformed PDF can be filled up nicely so a perfect (climatological) Gaussian variable can be generated. However, the idea of "random" observations does not have a sound theoretical basis and it may lead to additional sampling errors. We tested this

idea in our data assimilation experiments but its experimental impact was no better than the climatological (CZ) or background (BZ) median approaches. Therefore, this method will not be used in this dissertation.

2.6 Observation errors in the transformed space

When a variable transformation algorithm is used in the data assimilation, not only are the observables transformed (see Chapter 2.4), but the observation error associated with the transformed variable will also be different from the original error value. In theory, we should be able to estimate the observation error for the transformed variable based on the error for the original variable. It can be done by the transformation of the entire PDF from the original physical space to the transformed space, and estimating the new variance after the transformation. However, it is not an easy computation. Simon and Bertino (2012) proposed a computationally feasible method based on the Monte Carlo method, consisting of three steps. First, a number of perturbed observations are generated in the original physical space by specifying a known error distribution such as normal or log-normal distributions. Second, the transformation is applied to those perturbed observations. Third, the new variance is computed from the sample of the perturbed observations in the transformed space. This strategy can be particularly useful if the observation error of the original variable is well known.

However, it is noted that the shapes of the error distributions before and after the transformation should be different; i.e., if we assume a Gaussian error distribution in the original variable, then the transformed error distribution will not be Gaussian. Nevertheless, only the Gaussian error distribution can be used in data assimilation

schemes such as the LETKF, so we must approximate the transformed PDF with a Gaussian distribution represented by its variance. Considering again the idea of the transformation, by introducing the transformation, we should expect that the error distribution in the transformed space is more Gaussian than that in the original physical space (Figure 2.2). In that sense, the transformation of the error PDF, starting from a Gaussian distribution, would not be a proper approach. On the contrary, estimation of the error or the error model with the transformation variable alone, regardless of the original variable, should be a better direction.

In our study, when we conduct OSSEs in Chapter 3, since we know exactly the error magnitudes of the simulated observations, we take a similar strategy as Simon and Bertino (2012) to compute the transformed observation error from the original error value, but our method is much simpler: Only two samples, the observation value plus/minus one standard deviation, are considered. Conceptually,

$$\tilde{\sigma}^o \cong T[y^o + \sigma^o] - T[y^o] \cong T[y^o] - T[y^o - \sigma^o] , \tag{2.24}$$

where y^o is the original observation value, $T[\,]$ is the transformation, σ^o is the observation error for the original variable, and $\tilde{\sigma}^o$ is the observation error for the transformed variable whose squares appear in the diagonal elements of $\mathbf{R}$ in the data assimilation. We choose to determine the final $\tilde{\sigma}^o$ value by requiring both two estimates, $\tilde{\sigma}^{o+} = T[y^o + \sigma^o] - T[y^o]$ and $\tilde{\sigma}^{o-} = T[y^o] - T[y^o - \sigma^o]$, be at least 0.1 (unitless in the transformed variable) and then averaging them; namely,

$$\tilde{\sigma}^o = \frac{1}{2}[\max(\tilde{\sigma}^{o+}, 0.1) + \max(\tilde{\sigma}^{o-}, 0.1)] . \tag{2.25}$$

When we conduct real precipitation assimilation experiments in Chapters 6 and 7, since the precipitation observation errors are basically unknown, it would not be a

good idea to adopt this strategy. Instead, we will use simple constant values as the observation errors for the transformed precipitation (applied to both logarithm transformation and Gaussian transformation). We conducted many trials to obtain the best constant value experimentally. A more detailed discussion about the errors of the satellite precipitation retrievals can be seen in Section 5.1.2.

Chapter 3: Perfect-model experiments with SPEEDY model

3.1 Introduction

In this chapter, we show the results of precipitation assimilation experiments with the Simplified Parametrizations, primitivE-Equation DYnamics (SPEEDY) model (Molteni 2003). The experiments are conducted within an identical-twin observing system simulation experiment (OSSE) framework, so they are "perfect-model" experiments without considering model errors. We first use this simpler system to test our idea of the LETKF assimilation of global precipitation with the transformation techniques. There are many advantages in using a simpler system for a proof-of-concept study. It helps us to get rid of many uncertainties that we are not able to address at the first stage, and allows us to conduct experiments more quickly given the limited computing resources in order to do many sensitivity tests. Besides, the precipitation assimilation is a challenging topic even with such simpler systems. For example, when we previously used the same OSSE framework, but without introducing the Gaussian transformation of precipitation and other modifications described later in this chapter, the precipitation assimilation failed. Therefore, a success demonstration of precipitation assimilation with this simple system will be an essential first step before applying our ideas to more complicated systems.

3.2 The SPEEDY model

The SPEEDY model (Molteni 2003) is a simple, computationally efficient, but still realistic general circulation model that has been adapted for data assimilation

experiments (Miyoshi 2005) and widely used (e.g., Kang et al. 2011). The version of SPEEDY model used in this study is run at a T30 resolution with 7 vertical sigma levels. It has five state variables: the zonal (U) and meridional (V) components of winds, temperature (T), specific humidity (Q), and surface pressure (Ps). In addition to those state variables, the previous 6-hour accumulated precipitation (PP) is a diagnostic variable that is also calculated by the model, which allows easy implementation of the precipitation assimilation in the LETKF system. Note that the diagnostic PP in the analyses plays no role in the subsequent forecasts, and all improvements in model forecasts are achieved by the update of the state variables.

The convective parameterization scheme is a simplified mass-flux scheme activated whenever conditional instability is present, and humidity in the planetary boundary layer (PBL) exceeds a prescribed threshold. The cloud-base mass flux (at the top of the PBL) is computed in such a way that the PBL humidity is relaxed towards the threshold value on a time-scale of 6 h. The large scale condensation is created by relaxing the humidity above saturation towards a sigma-dependent threshold value on a time scale of 4 h. Although the model resolution is very low and the parameterization scheme is simple, the SPEEDY model produces realistic precipitation (Molteni 2003) and responds realistically to anomalous SST forcing (Kucharski et al. 2013). Therefore, we think the complexity of the model is sufficient for preliminary precipitation assimilation studies.

3.3 Experiment design

3.3.1 General settings

The SPEEDY model is first run for a one year spin-up (year 1981) and then for 10 years, from January 1, 1982 to January 1, 1992 forced by the climatological sea surface temperature. These 10 years of simulation are used to compute the CDFs of precipitation in preparation for defining the Gaussian transformation. The same run in the period from January 1, 1982 to January 1, 1983 is also regarded as the nature run, or the "truth" in the OSSEs. Figure 3.1 shows the comparison between the mean daily precipitation amount in our 10-year model run and in a high-quality precipitation analysis. It is concluded that the climatology produced from the SPEEDY model is reasonably good compared to the analysis data.

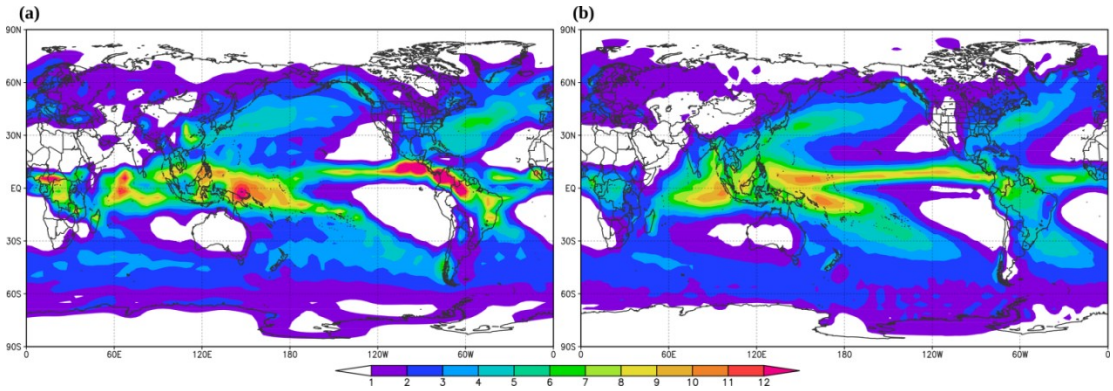

Figure 3.1: The mean daily precipitation amount (mm) in (a) the 10-year nature run with the SPEEDY model and (b) CPC Merged Analysis of Precipitation (CMAP) from 1979 to 2011.

The CDFs of precipitation is computed for each grid point and each season, and the transformations of both observation and model precipitation variables are thus

followed in terms of their geographical location and season during the data assimilation computation:

$$\tilde{y} = F^{G^{-1}}[F(y; \text{location, season})] \,. \tag{3.1}$$

The periods of four seasons are allocated as March–May, June–August, September–November, and December–February. Besides, we define the y_{trace} value to be 0.1 mm for 6-hour accumulations; i.e., the precipitation values that are less than 0.1 mm $(6\text{h})^{-1}$ are regarded as "zero precipitation."

Simulated observations are taken from this nature run by adding random noise corresponding to the designated observation errors. The basic observing system used in this study is just conventional rawinsonde observations that are assimilated in the control run ("RAOBS" hereafter). The rawinsonde locations are distributed realistically as shown by open circles in Figure 3.2. Variables assimilated include u, v winds, temperature, specific humidity, and surface pressure, whose observation errors are listed in Table 3.1. Additional precipitation observations are assimilated in other experiments to estimate the impact of the precipitation assimilation. The 6-hour accumulated precipitation data are obtained from the nature run every 2 by 2 model grid points (i.e., every 7.5° by 7.5°) simulating satellite retrievals (indicated with plus signs in Figure 3.2). The observation errors of precipitation observations are set to be either 20% or 50% of the observed values for the non-zero precipitation (i.e., normal random errors with standard deviation 20% or 50% of the true values are added when generating the precipitation observations) and no error when zero precipitation is observed in the nature run, based on the assumption that clear air observations have no uncertainty. Covariance localization is computed adjusting the observation errors

by their distance (the "R localization" in Greybush et al. 2011), with a horizontal length scale L = 500 km and a vertical length scale of 0.1 in natural logarithm of pressure for all observations with two exceptions:

1) No vertical localization is applied for precipitation observations because of the expected correlation between precipitation and model variables in deep layers.
2) Reduced horizontal localization lengths for precipitation observations are used in two experiments ("0.5L" and "0.3L") in order to test the sensitivity of the results to precipitation localization.

The adaptive inflation scheme of Miyoshi (2011) is used. In addition, to obtain stable analyses, the upper-level (the highest 3 model levels) moisture (Q) observations are not used, and the upper-level Q variables in the model are also not updated by any other observations.

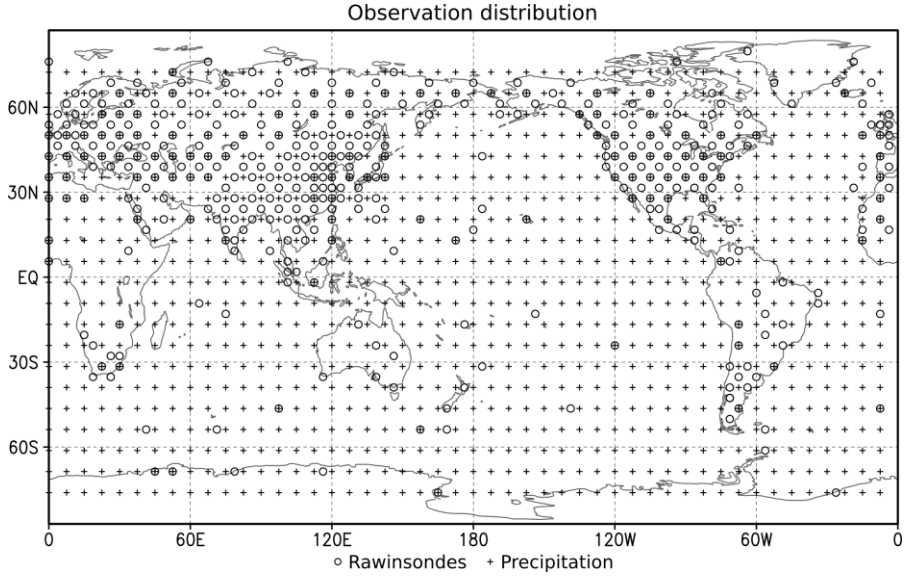

Figure 3.2: The spatial distribution of conventional rawinsonde observations (open circle) and global precipitation observations (plus sign) used in the OSSEs.

Table 3.1: The observation errors for the simulated observations.

Variable	Observation error
U	1.0 m s^{-1}
V	1.0 m s^{-1}
T	1.0 K
Q (specific humidity)	1.0×10^{-3} kg kg^{-1}
Ps (surface pressure)	1.0 hPa
PP (previous 6-hour accumulated precipitation)	20% or 50% (in different experiments)

Twenty ensemble members are used in our assimilation experiments. Starting from January 1, 1982, all experiments are initialized with the same initial ensemble created by a random choice of model conditions at an unrelated time in the nature run, so they are very different from the "truth." Observation data are then assimilated into the model with a 6-hour cycle. All experiments are run for 1 year until January 1, 1983. The differences among experiments are summarized in Table 3.2. First, in "RAOBS", only the rawinsonde observations are assimilated. We denote the control experiment showing the effectiveness of precipitation assimilation as "PP_CTRL", in which precipitation is assimilated and the Gaussian transformation is performed. Unless mentioned otherwise, the simpler "climatological median" of zeros (CZ) method to transform the zero values is used. All prognostic variables in the SPEEDY model are updated during the assimilation as in the standard formulation of LETKF. The observation error of precipitation observations in this experiment is rather accurate, 20%, and the localization length of precipitation observations is the same as rawinsonde observations (i.e., L = 500 km). In "Qonly", only the specific humidity Q

is updated during the LETKF assimilation of precipitation observations. This is analogous to conventional "nudging" methods using precipitation observations to only modify the moisture field in the model. Other sensitivity experiments listed in Table 3.2 will be introduced later. Further, for these experiments, 5-day free forecasts initialized from each 6-hourly ensemble mean analysis over the year are conducted in order to quantify the forecast impacts of the assimilation of precipitation.

Table 3.2: Design of all experiments. "GTcz" and "GTbz" stand for the Gaussian transformation with the CZ and BZ methods, respectively, to transform zero precipitation.

Experiment	Observation		Transf	QC for precip assimilation	Obs error of precip	Loc length of precip
	Raobs	Precip				
RAOBS	X					
PP_CTRL	X	X	GTcz	Precip members ≥ 10	20%	1L (= 500km)
Qonly	X	X (only update Q)	GTcz	Precip members ≥ 10	20%	1L
noGT	X	X		Precip members ≥ 10	20%	1L
Log	X	X	Log	Precip members ≥ 10	20%	1L
GTbz	X	X	GTbz	Precip members ≥ 10	20%	1L
ObsR	X	X	GTcz	Obs precip > 0.1 mm h^{-1}	20%	1L
1mR	X	X	GTcz	Precip members ≥ 1	20%	1L
5mR	X	X	GTcz	Precip members ≥ 5	20%	1L
15mR	X	X	GTcz	Precip members ≥ 15	20%	1L
50%err	X	X	GTcz	Precip members ≥ 10	50%	1L
50%err_noGT	X	X		Precip members ≥ 10	50%	1L
0.5L	X	X	GTcz	Precip members ≥ 10	20%	0.5L
0.3L	X	X	GTcz	Precip members ≥ 10	20%	0.3L

3.3.2 Quality control based on the model background

In the traditional way of precipitation assimilation, the zero precipitation observations are usually discarded because those observations are difficult to use (e.g., Koizumi et al. 2005). Nevertheless, zero precipitation observations should contain valuable (and accurate) information about the atmospheric state. With our current transformation algorithm handling the zero precipitation and an ensemble data assimilation system, zero precipitation observations are, indeed, assimilated. Instead of discarding all zero observations, a different quality control criterion is used in this study: assimilation is conducted at all grid points where at least some members of prior ensemble are precipitating (regardless of the observed values). The motivation of this criterion is that if the ensemble spread is zero (i.e., all forecasts have zero precipitation), it is not possible to assimilate precipitation using an EnKF. In Section 3.5.1, we will show that assimilating precipitation observations at locations with only a few precipitating members does not show improvements, so that the criterion we have chosen in the PP_CTRL experiment is to require that at least half (10) of the forecasts have positive precipitation at the analysis grid point ("10mR" criterion hereafter), which controls the assimilation quality and saves computational time. We will also show that while this model background-based criterion only allows us to assimilate a small portion of the zero precipitation observations, this portion of observations seems to contain the crucial data which are really useful in the EnKF data assimilation.

3.4 Results

3.4.1 Global analysis and forecast errors

Figure 3.3 shows the evolution of the global root-mean-square (RMS) analysis errors (verified against the nature run) of the u-winds over one year. We only show this variable because the impacts are remarkably similar for all model variables, indicating that the assimilation of precipitation approach is indeed able to influence the full dynamical evolution of the model and not just the moist thermodynamics. Different time intervals are used to show the spin-up stage in the first month and for the remaining 11 months after the spin-up. The average values of RMS analysis errors in the last 11 months are also listed in Table 3.3. Note that the spin-up takes about one month because the ensemble initial states were chosen to be very different from the nature run at the initial time. In the LETKF (or any EnKF) a long spin-up is required in order to estimate not only the truth (with the ensemble mean), but also the "errors of the day" with the ensemble perturbations (Yang et al. 2012).

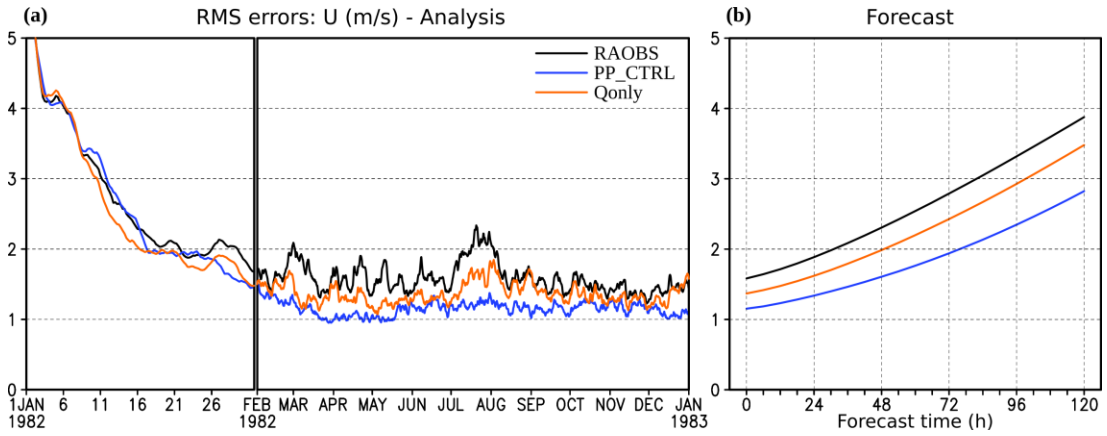

Figure 3.3: The global root-mean-square (a) analysis and (b) forecast errors (verified against the nature run) of u-winds in experiments PAOBS, PP_CTRL, and Qonly. For the analysis errors, the evolution over one year is shown. Different scales on the time axis are used for the spin-up period (the first month) and the remaining 11 months. For the forecast errors, the 11-month (after the spin-up) average values are shown versus the forecast time.

Table 3.3: Impact of precipitation assimilation on the last 11-month averaged analysis errors of u-wind.

Experiment	Last 11-month averaged RMSE of U (m s^{-1}) (percentage changes relative to RAOBS)			
	Globe	NH	TR	SH
RAOBS	1.58	0.67	1.64	2.03
PP_CTRL	1.15 (-27.2%)	0.53 (-20.6%)	1.45 (-11.2%)	0.91 (-55.2%)
Qonly	1.37 (-13.6%)	0.58 (-13.1%)	1.51 (-7.4%)	1.59 (-21.8%)

It is clear that when all variables (and therefore the full potential vorticity) are modified (PP_CTRL; blue line in Figure 3.3a), the improvement introduced by precipitation assimilation is quite large (27.2% reduction in the mean global analysis

error) after the first month of spin-up. Not only is the long-term averaged RMS error reduced, but the temporal variation of analysis accuracy is also reduced (e.g., the error jump observed in the RAOBS experiment during July is not seen in PP_CTRL). This result is very encouraging because it clearly shows that assimilating precipitation does bring significant benefits to the LETKF analysis. In contrast, when precipitation observations only modify the moisture field (Qonly; orange line in Figure 3.3a), the improvement is much smaller (only 13.6% reduction in the mean global analysis error after the spin-up), even though this approach also uses the Gaussian transformation and the model background-based observation selection criterion of precipitation.

In addition to the LETKF analysis, the impact of precipitation assimilation on model forecasts is also shown on Figure 3.3b. The global RMS forecast errors of u-wind are averaged over the last 11 months (i.e., after the spin-up). It is evident that the improvements last throughout the 5-day forecasts, so that the effect of precipitation assimilation is not "forgotten" by the model during the forecast, as experienced with nudging. Contrary to our expectations, the improvement by LETKF modifying only moisture (Qonly) also lasts throughout the forecast, which seems more effective than nudging possibly because of the use of the Gaussian transformation with an EnKF and/or the idealized OSSE framework. However, the improvement in Qonly is much smaller than that in PP_CTRL, and its error growth rate (i.e., the slope) is close to that in RAOBS whereas the error growth rate in PP_CTRL is smaller than for the other two experiments. As indicated before, similar improvements in the analysis and 5-day forecast errors are also observed in all other model variables, including the very important precipitation forecasts. Figure 3.4

shows that the precipitation forecasts are improved as well by assimilating the precipitation observations. Starting from 12 forecast hours, the error growth rates are stable, and the forecast improvement on precipitation in PP_CTRL relative to RAOBS is more than 2 days.

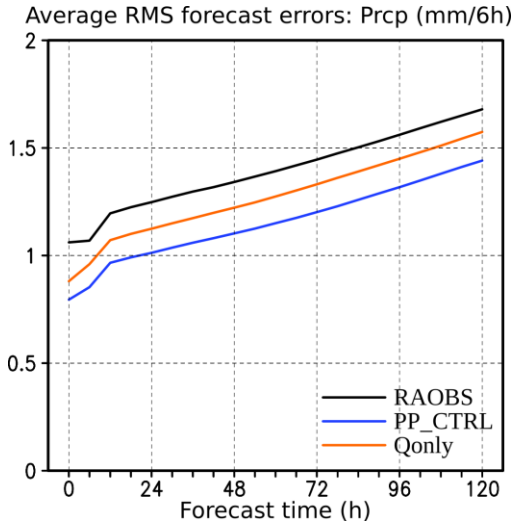

Figure 3.4: As in Figure 3.3b, but for precipitation forecast errors.

3.4.2 Regional dependence

The regional dependence of the impact of precipitation assimilation is discussed in this section. The RMS errors are computed for three regions: the Northern Hemisphere extratropics (30–90N; NH), the tropics (30S–30N; TR), and the Southern Hemisphere extratropics (30–90S; SH). Figure 3.5 shows the RMS errors of u-wind in 0 – 5 day forecasts averaged over the last 11 months for main experiments as Figure 3.3b, but for each region. For all other experiments, the 11-month average RMS analysis errors in terms of separate regions are also listed in several tables: Table 3.3–3.5, 3.7, and 3.8.

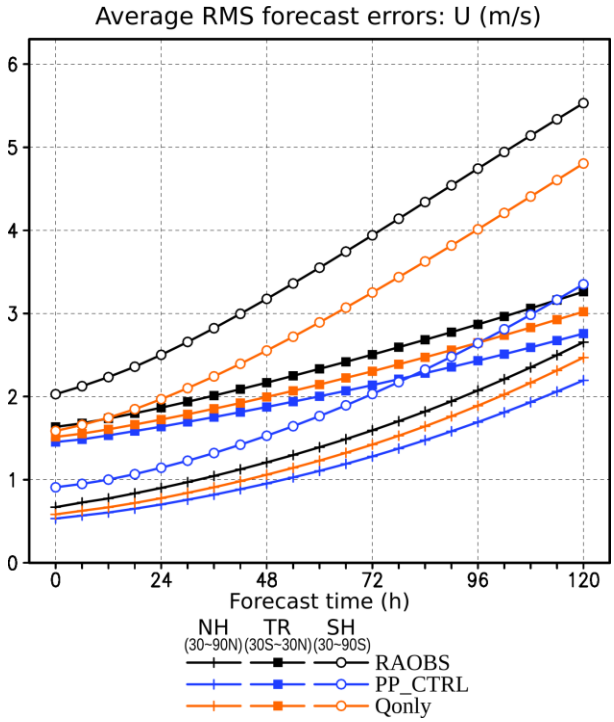

Figure 3.5: As in Figure 3.3b, but the RMS forecast errors are calculated separately for the Northern Hemisphere extratropics (30–90N; NH), the tropics (30S–30N; TR), and the Southern Hemisphere extratropics (30–90S; SH), indicated by different marks on the lines.

It is clear that, as in operational forecasts, these three regions have distinct characteristics of analysis errors, error growth rate, and the impact of precipitation assimilation. With only rawinsonde observations (RAOBS), the analysis (0 hour) in the NH region is already quite accurate, while the TR analysis is less accurate and the SH analysis is the least accurate. As a result, the precipitation assimilation only has a small effect on the NH region (20.6% reduction in PP_CTRL) but a large effect on the SH region (55.2% reduction in PP_CTRL). The effect on the TR region is even smaller (11.2% reduction in PP_CTRL), which could be due to differences in dynamical instabilities and precipitation mechanisms between the tropical and

extratropical regions. The prevailing convective precipitation in the tropics tends to maintain small-scale features and thus would be more difficult to capture in this low-resolution global model implementing only the large-scale mass-flux parameterization scheme and by low-resolution observations. During the 5-day forecasts, the RMS errors in both NH and SH regions grow with similar rates, faster than that in the TR region, as observed in operational forecasts (Reynolds et al. 1994; Bengtsson et al. 2005), due to the stronger growth rates of mid-latitude baroclinic instabilities. The RMS errors in the NH region are then close to those in the TR region at the end of the 5-day forecasts. The improvement by precipitation assimilation in the SH region is so large that the RMS analysis and most forecast errors in the SH region in PP_CTRL are even better than those in the TR region even though without precipitation assimilation the SH analyses and forecasts are much less accurate. The difference between the LETKF modifying all variables and only modifying moisture is also emphasized in the SH region with the difference in RMSE between Qonly and PP_CTRL increasing with forecast time. Note that in spite of different dynamical nature of error growth in the three regions, precipitation assimilation does lead to positive impacts in all regions.

Global maps of (temporally averaged) RMS errors and error reduction of the mid-level vorticity ($\sigma = 0.51$) for the 72-hour forecasts during the last 11 months are shown in Figure 3.6. As expected, the error in RAOBS (contours) is large in the Southern Hemisphere since the conventional rawinsonde network is quite sparse in that region. The Southern Ocean near the southern end of South America has the largest error in the world presumably because it is the least observed. By contrast, the

RAOBS vorticity forecast error is generally small in the Northern Hemisphere, especially over the Euro-Asian continent with the densest rawinsonde observations. By including the precipitation observations in LETKF assimilation, the vorticity error reduction (i.e., the RMS error of PP_CTRL – the RMS error of RAOBS; shaded) is large in the SH extratropical region, smaller in the NH extratropical region, and smallest in the tropical region. Once again, the dynamical impact of assimilation of precipitation on the evolution is shown by the fact that the largest error reduction is almost collocated with the regions with the largest error in RAOBS, where the room for improvement is large, and yet the error is still reduced even in rawinsonde-rich Northern Hemisphere. The tropical region, instead, shows the smallest improvement, and the eastern equatorial Pacific and the central Africa are the only two areas that show slightly negative impacts. We can conclude that precipitation assimilation in the EnKF has a profound impact on vorticity through the dynamical impact of giving higher weights to the ensemble members with more accurate precipitation. This improvement is observed almost everywhere.

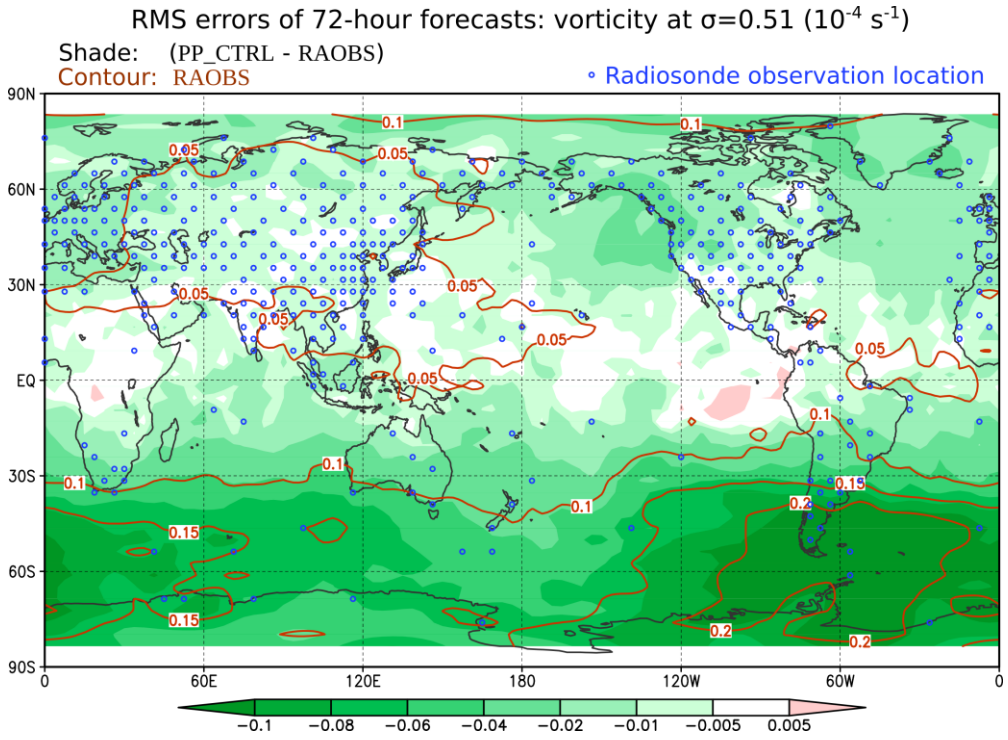

Figure 3.6: The global map of RMS 72-hour forecast errors of the vorticity at $\sigma = 0.51$ during the 11 months after the spin-up in RAOBS (brown contour) and the corresponding error reduction from PP_CTRL to RAOBS (shading). The rawinsonde observation locations are also shown in blue open circles.

3.4.3 Comparison among transformation methods.

Several experiments using different methods of precipitation transformation are compared in Figure 3.7 assuming accurate precipitation (20% errors). In experiment "noGT", no transformation of precipitation is applied; in experiment "Log", the logarithm transformation is used; in experiment "GTbz", the Gaussian transformation with the "background median of zeros" (BZ) method to transform the zero precipitation is used instead of the CZ method. As shown in the figure, during the spin-up stage, the LETKF analysis without the transformation of precipitation (noGT;

red line in Figure 3.7) is worse than PP_CTRL when the Gaussian transformation is applied. However, with these accurate observations, the Gaussian transformation does not make a significant difference after the spin-up period (Table 3.4; 26.1% vs. 27.2% reduction in the mean global analysis errors). It is possible that the proposed Gaussian transformation is especially useful to the LETKF assimilation when the model background is less accurate and the difference between model background and the precipitation observations is large. Therefore, when the analysis is accurate enough after the first month of spin-up, the Gaussian transformation does not offer a major advantage. The impact of the Gaussian transformation in experiments with less accurate precipitation observations is, however, much larger and will be shown in Section 3.5.2.

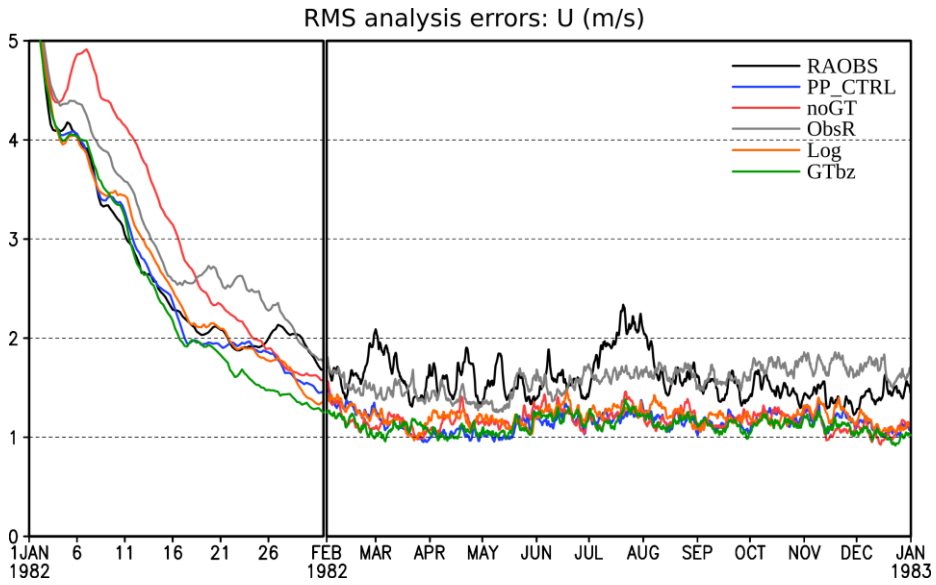

Figure 3.7: As in Figure 3.3a, but for experiments RAOBS, PP_CTRL, noGT, ObsR, Log, and GTbz.

The logarithm transformation (Log; orange line in Figure 3.7) results in similar evolution of the analysis errors as the PP_CTRL using the Gaussian transformation, but the overall analysis errors are slightly larger than those in PP_CTRL in all verification regions (Table 3.4; 23.5% vs. 27.2% reduction in the mean global analysis errors). This comparison demonstrates the advantage of the Gaussian transformation over the simple logarithm transformation which may be too ideal and not necessarily optimal. However, we do not put too much emphasis on the logarithm transformation here with the SPEEDY model experiments. The effect of the logarithm transformation will be examined more carefully in Chapters 5–7 with real precipitation observations and a more realistic model.

Table 3.4: Impact of precipitation transformation methods.

Experiment	Last 11-month averaged RMSE of U (m s^{-1}) (percentage changes relative to RAOBS)			
	Globe	NH	TR	SH
RAOBS	1.58	0.67	1.64	2.03
PP_CTRL (20%err)	1.15 (-27.2%)	0.53 (-20.6%)	1.45 (-11.2%)	0.91 (-55.2%)
noGT (20%err)	1.17 (-26.1%)	0.52 (-22.0%)	1.47 (-10.3%)	0.95 (-53.0%)
Log	1.21 (-23.5%)	0.55 (-17.9%)	1.53 (-6.7%)	0.96 (-52.5%)
GTbz	1.12 (-29.3%)	0.52 (-22.7%)	1.40 (-14.3%)	0.91 (-55.0%)

On the other hand, when we repeat the experiment using the BZ method in the Gaussian transformation (GTbz; green line in Figure 3.7) instead of the CZ method, we obtain even better results than PP_CTRL. It spins up faster than all other experiments and maintains an analysis that is slightly more accurate than that in

PP_CTRL (Table 3.4; 29.3% vs. 27.2% reduction in the mean global analysis errors). More importantly, although this additional improvement is not big in the analysis, but it keeps growing with forecast time in the 5-day forecasts (Figure 3.8). Therefore, the Gaussian transformation with the BZ method is the best method for the precipitation transformation in this OSSE configuration. Again, we will discuss more about the differences among the transformation methods in later chapters.

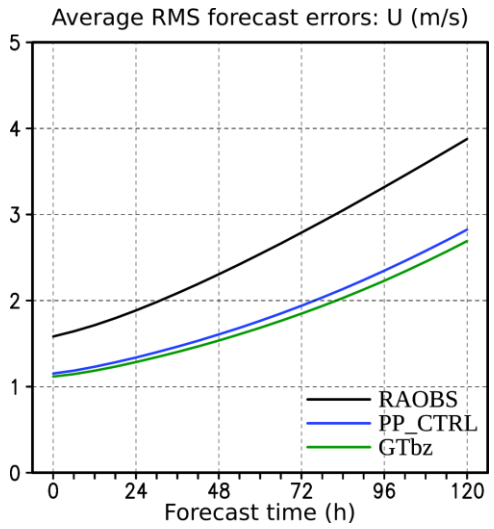

Figure 3.8: As in Figure 3.3b, but for experiments RAOBS, PP_CTRL, and GTbz.

3.5 Sensitivity experiments

The other sensitivity experiments are as follows: Experiments "1mR", "5mR", and "15mR" are conducted to test the sensitivity to the quality control criteria for assimilation. They vary the critical number of precipitating members to 1, 5, and 15 from 10 in PP_CTRL. Experiments "50%err" and "50%err_noGT" are conducted to test the impact of lower observation accuracy on the precipitation assimilation, using higher precipitation observation errors of 50% rather than 20%. In addition,

experiments “0.5L” and “0.3L”, which vary the localization length to 250 and 150 from 500 km in PP_CTRL, are conducted in order to test the sensitivity to the localization lengths of precipitation observations.

3.5.1 Sensitivity to quality control criteria

Figure 3.7 also shows the analysis error of the “ObsR” experiment that uses the traditional criterion of assimilating only positive rain observations [> 0.1 mm $(6h)^{-1}$]. Compared it with our newly proposed 10mR criterion that requires at least half of the background members to rain (PP_CTRL), the 10mR criterion seems to be essential in order to have effective precipitation assimilation. The analysis of ObsR (gray line in Figure 3.7) is obviously degraded from PP_CTRL (Table 3.5; giving only a 0.3% reduction relative to RAOBS in the mean global analysis error). In particular, the degradation comes mainly from the tropical region (30S–30N; Table 3.5; 18.7% increase in the mean analysis error), which indicates that this observation-based criterion is not useful in our experimental setup in areas dominated by convective precipitation. Table 3.5 also shows the results of additional experiments with different minimum numbers (1, 5, and 15 out of 20) of precipitating ensemble members required to assimilation precipitation observations. With a criterion that is too lenient (requiring only 1 or 5 precipitating members), the improvement by precipitation assimilation is also degraded. This indicates that assimilating precipitation observations at locations where precipitating members are rare can hurt the analysis. If stricter criteria (10mR or even 15mR) are used as we do in most experiments in this study, the results are better. Note that this type of criteria also automatically allows some zero precipitation observations to be assimilated, provided that there are enough

precipitating members at the observation location. These locations will probably be in areas of scattered precipitation or near the edges of large-scale precipitation. Average numbers (and percentages) of observations in 4 different classes in terms of the observation-based criterion and the model background-based criterion in PP_CTRL experiment after the spin-up is shown in Table 3.6. It is shown that the current 10mR criterion only allows a small portion of the zero precipitation observations (bold; 48.9 out of 542.6, the average number of zero precipitation observations) to be assimilated in our control experiment. Since the results are significantly improved by using this criterion, it is clear that this small portion of precipitation observations is crucial and really useful in the EnKF data assimilation. Given the fact that the observation data in the upper-right corner of the table (i.e., precipitation observed but no enough precipitating members in the background) are not used in our "10mR" method, and physically this part of data is also expected to have valuable information, it would be worth exploring other ways to exploit information from these data.

Table 3.5: Impact of quality control criteria of precipitation observations.

Experiment	Last 11-month averaged RMSE of U (m s^{-1}) (percentage changes relative to RAOBS)			
	Globe	NH	TR	SH
RAOBS	1.58	0.67	1.64	2.03
ObsR	1.58 (-0.3%)	0.69 (+3.4%)	1.94 (+18.7%)	1.40 (-31.0%)
1mR	1.29 (-18.6%)	0.57 (-14.3%)	1.62 (-0.9%)	1.04 (-48.6%)
5mR	1.19 (-25.2%)	0.52 (-22.3%)	1.50 (-8.5%)	0.94 (-53.6%)
PP_CTRL (10mR)	1.15 (-27.2%)	0.53 (-20.6%)	1.45 (-11.2%)	0.91 (-55.2%)
15mR	1.13 (-28.9%)	0.52 (-23.0%)	1.42 (-13.4%)	0.89 (-56.0%)

Table 3.6: The average numbers and percentages (in parentheses) of observations in 4 classes in terms of the observation-based criterion and the model background-based criterion in PP_CTRL experiment after the spin-up. The bold, underlined classes are assimilated into the model and the others are not used. The total number of observations is 1008 at every cycle.

	Obs precip rate $<$ 0.1 mm $(6h)^{-1}$	Obs precip rate $\geq$ 0.1 mm $(6h)^{-1}$
Background precip members $<$ 10	493.7 (49.0%)	134.5 (13.3%)
Background precip members $\geq$ 10	**48.9 (4.9%)**	**330.9 (32.8%)**

3.5.2 Sensitivity to the accuracy of precipitation observations

As mentioned in Section 3.4.3, with accurate precipitation observations of 20%, the application of the Gaussian transformation to the precipitation variable has only a minor impact on the LETKF analysis accuracy after the spin-up (Figure 3.7). However, this is not the case when we use more realistic precipitation observation errors of 50%. Figure 3.9 and Table 3.7 shows the impact of both larger observation errors as well as the use of the Gaussian transformation. The observation error of precipitation observations is increased to 50% both in the observations and in the LETKF estimation of observation errors. When the Gaussian transformation is used (50%err vs. PP_CTRL which uses 20%err), the analysis becomes only slightly worse (shown as a green line in Figure 3.9). However, without the Gaussian transformation

and with 50% errors (50%err_noGT; red line in Figure 3.9), the precipitation assimilation fails. The LETKF analysis in 50%err_noGT is actually worse than not assimilating precipitation in each region, as well as globally (Table 3.7). In other words, without the Gaussian transformation the precipitation assimilation hurts the analysis, whereas 50%err with the Gaussian transformation is almost as good as that obtained with the much smaller 20% errors. This sensitivity test demonstrates the importance of the Gaussian transformation. Less accurate observations will tend to have larger differences from the model background and may not be able to make the analysis accurate enough, so that the non-Gaussian effects become more important for large errors. Note that the errors of real satellite or radar precipitation estimates depend strongly on the degree of spatial and/or temporal averaging applied to the data (Huffman et al. 2010), and that a 50% error in precipitation observations would be considered quite good for such products (Bowman 2005). Therefore, the Gaussian transformation proposed in this study seems essential for the practical assimilation of precipitation.

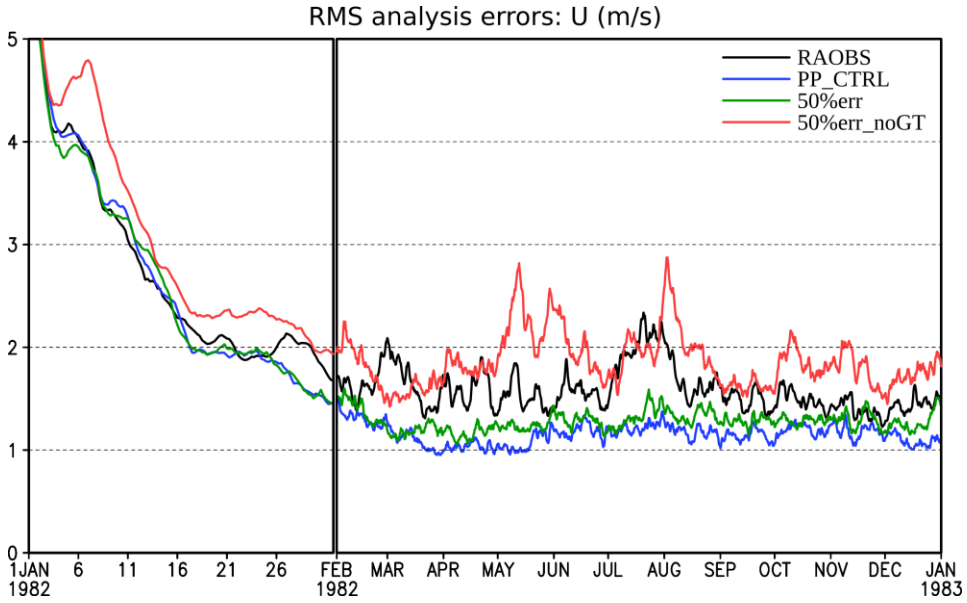

Figure 3.9: As in Figure 3.3a, but for experiments RAOBS, PP_CTRL, 50%err, and 50%err_noGT.

Table 3.7: Impact of accuracy of precipitation observations with and without the Gaussian transformation.

Experiment	Last 11-month averaged RMSE of U (m s^{-1}) (percentage changes relative to RAOBS)			
	Globe	NH	TR	SH
RAOBS	1.58	0.67	1.64	2.03
PP_CTRL (20%err)	1.15 (-27.2%)	0.53 (-20.6%)	1.45 (-11.2%)	0.91 (-55.2%)
noGT (20%err)	1.17 (-26.1%)	0.52 (-22.0%)	1.47 (-10.3%)	0.95 (-53.0%)
50%err	1.28 (-19.2%)	0.59 (-12.5%)	1.52 (-6.9%)	1.26 (-38.1%)
50%err_noGT	1.87 (+17.8%)	0.79 (+18.2%)	2.00 (+22.0%)	2.29 (+12.9%)

3.5.3 Sensitivity to the localization lengths of precipitation observations

In all experiments so far we have used the same horizontal localization length scale for precipitation assimilation as for rawinsonde observations (500 km, denoted as 1L). Since dense global precipitation observations are assimilated in our OSSEs, and precipitation has more local characteristics than the dynamical variables, we speculate that the optimal horizontal localization length scale for precipitation observations could be smaller than that for rawinsonde observations. Two additional experiments, 0.5L and 0.3L, with 250 and 150 km localization lengths for precipitation observations, respectively, are conducted. It is observed in Table 3.8 that the smaller length scales improve the LETKF analyses, and the 0.5L (250 km) length scale would be close to optimal under our current experimental design. The averaged RMS analysis error after the spin-up can be reduced by 32.7% relative to RAOBS when the 0.5L length scale is used, compared with 27.2% when using the original length scale. This suggests that the optimal localization length could vary with different observation datasets and experimental settings and should be tuned appropriately. It would be interesting to try localization length scales that vary geographically, e.g., smaller length in tropics or wherever precipitation is mostly dominated by convection.

Table 3.8: Impact of horizontal localization lengths of precipitation observations.

Experiment	Last 11-month averaged RMSE of U (m s^{-1}) (percentage changes relative to RAOBS)			
	Globe	NH	TR	SH
RAOBS	1.58	0.67	1.64	2.03
PP_CTRL (1L)	1.15 (-27.2%)	0.53 (-20.6%)	1.45 (-11.2%)	0.91 (-55.2%)
0.5L	1.07 (-32.7%)	0.48 (-28.0%)	1.31 (-20.0%)	0.95 (-53.4%)
0.3L	1.14 (-27.8%)	0.53 (-20.2%)	1.37 (-16.2%)	1.08 (-46.6%)

3.6 Summary and discussion

Past attempts to assimilate precipitation observations into NWP models have found it difficult to improve model analyses and, especially, model forecasts. In the experience with nudging or variational methods, the forecasts starting from analyses with precipitation assimilation lose their extra skill in forecasts of precipitation or other dynamical variables after a day or less (e.g., Errico et al. 2007). The linear representation of moist physical processes required in the variational data assimilation and the non-Gaussianity of precipitation observations and model perturbations are both major problems in precipitation assimilation (e.g., Bauer et al. 2011).

The EnKF does not require linearization of the model, thus addressing the first problem. The ensemble can give the "error correlation of the day", essential to produce optimal analyses. In precipitation assimilation, the EnKF can take advantage of the original nonlinear precipitation parameterization to establish useful finite amplitude perturbation covariances between the diagnostic precipitation output and

all other state variables without additional computational cost. In this way, the EnKF is expected to more efficiently improve the potential vorticity field compared to nudging or variational approaches. Since potential vorticity is the variable that primarily determines the evolution of the forecast in NWP models, it is not surprising that the analysis improvement due to precipitation used in an EnKF is not so quickly "forgotten" in the forecasts.

In addition to using the EnKF, we introduce two important changes in the data assimilation procedure that contribute to improving the performance of precipitation assimilation. Firstly, we adopt the Gaussian transformation for precipitation based on its climatological distribution in the model. Secondly, we propose a model background-based criterion in the ensemble data assimilation: precipitation observations are assimilated only at grid points where at least some members of the forecast ensemble are precipitating. This automatically allows zero precipitation observations to be assimilated.

To prove these concepts, we conduct identical-twin OSSEs of global precipitation assimilation with the SPEEDY model and the LETKF. The SPEEDY model is a relatively simple global circulation model, but able to simulate a realistic climatology (Molteni 2003). Results in our OSSEs are extremely encouraging. By assimilating global precipitation, the globally averaged RMS analysis errors of u-winds after the spin-up stage are reduced by as much as 29% (in GTbz) as compared to only assimilating rawinsonde observations. The improvement is not "forgotten" and persists throughout the entire 5-day forecasts. All model variables show similar impacts of the precipitation assimilation. The improvement is much reduced when

only the moisture field is modified by the precipitation observations. By separating the globe into three verification regions, i.e., the NH extratropics, the tropics, and the SH extratropics, it is shown that the effect of precipitation assimilation is larger in the SH region than that in the NH region since the NH analyses are already accurate due to the denser rawinsonde network. The tropical region shows the least relative improvement probably because of the slower dynamical instabilities and the prevailing convective precipitation type with small-scale features. Reducing the localization scale in these regions may improve the impact in the tropics.

In addition, a number of comparisons among experiments are made in order to assess the impact of different transformation methods and the observation selection criteria, as well as the sensitivity to the precipitation error level and to the localization length scale used for the precipitation observations. Applying the Gaussian transformation does not have a large impact on the analysis errors when precipitation observation errors are at an accurate 20% level, but it is very beneficial when observation errors are at a much higher (and realistic) 50% level. As to the impacts by different transformation methods, the logarithm transformation is slightly worse than the Gaussian transformation in our case, and the BZ method is slightly better than the CZ method for transforming zero precipitation values with the Gaussian transformation. The proposed 10mR data selection criterion (assimilating precipitation at the location where at least half of the members are precipitating) allows using some zero precipitation observations, and gives much better results than the traditional observation-based criterion of only assimilating positive precipitation,

and better than assimilating more observations with a looser criteria (1mR and 5mR criteria).

Although these results are promising, it is important to recognize that the SPEEDY model is simple, that model errors, especially in precipitation parameterization, are absent in this identical-twin OSSE setting, and that the simulated observations might be too idealized. In a real system, an accurate precipitation parameterization scheme would be very important to the precipitation assimilation. We still expect the EnKF to show advantages in this case because the original well-tuned nonlinear moist physics can be directly used for the data assimilation. Besides, the dimensionality of the employed system, a T30 horizontal resolution with 7 vertical levels, is very low compared to current operational systems. This low resolution prevents us from addressing some aspects of precipitation assimilation such as the strong and small-scale convective precipitation in tropical regions. In addition, with a real system, the difficulty of estimating errors of precipitation observations will emerge as another critical issue that is absent in the current OSSE framework.

Nevertheless, this set of experiments with the SPEEDY model is an essential first step to understand the feasibility and potential of the precipitation assimilation using an ensemble data assimilation method. The results suggest that, in our relatively simple system, the EnKF provides advantages for precipitation assimilation beyond the traditional nudging or variational methods. In the later chapters, follow-up studies using a more realistic model and assimilating real satellite precipitation observations will be presented.

Chapter 4: LETKF data assimilation with the NCEP GFS model

4.1 Introduction

With the success of the SPEEDY model experiments, we proceed to test our idea of precipitation assimilation using a more realistic setting. We choose to use a lower resolution version of the NCEP Global Forecasting System (GFS) model assimilating the TRMM Multi-satellite Precipitation Analysis (TMPA). The primary data assimilation system for the GFS model is the Gridpoint Statistical Interpolation (GSI; Kleist et al. 2009), which uses 3-dimensional variational method (3DVar). There have been several efforts on the coupling of ensemble data assimilation systems to the GFS model. Szunyogh et al. (2008) tested the LETKF with a low resolution version of the GFS model and obtained comparable analysis accuracy as the variational method. Besides, with NCEP's recent movement from the traditional 3DVar to the hybrid 3DVar-EnKF system, several versions of EnKF for the GFS model has been created (Whitaker et al. 2008; Kleist 2012; Wang et al. 2013). However, these versions of GFS-EnKF are run on specific machines and may be difficult to be ported to the university research environment with limited computational resources, so we decided to develop our own GFS-LETKF system to conduct the real precipitation assimilation experiments. The purpose of developing this system is not limited to the use of precipitation assimilation, but also for other research plans, in particular, the project of coupled atmospheric-oceanic data assimilation system led by Eugenia Kalnay. In this chapter, we will describe the main goals of the development and provide an overview of the system.

4.2 *The GFS model*

The GFS model is an operational global NWP model developed by the Environmental Modeling Center (EMC) at the NCEP. It is one of the major state-of-the-art operational NWP models over the world and provides main model guidance for the weather forecast in the United States. We asked a version of the GFS model from the EMC with the kind help from Henry Huang and Daryl Kleist. This version was successfully ported to our own Linux cluster in the department by the valuable contribution from Tetsuro Miyachi. The GFS model can be run at various resolutions from T62 to T574, all with 64 vertical levels (L64) on a hybrid sigma/pressure coordinate. T574 has been the current operational resolution since 2010. We will take advantage of the lower-resolution versions (T62/T126) of the GFS model to quickly conduct our experiments of precipitation assimilation. The prognostic variables in the GFS model include the zonal (U) and meridional (V) components of winds, temperature (T), specific humidity (Q), cloud condensate (Qc), and surface pressure (Ps), so these are used as the state variables in our GFS-LETKF system.

4.3 *Development of the GFS-LETKF*

4.3.1 General strategies

We hope the development of the GFS-LETKF system can benefit not only this study but also other planned data assimilation researches. The general strategies are as follows:

- The system is targeted to be run at lower resolution with simple configurations in order to favor fast experiments to study new data assimilation ideas, but it

still preserves the flexibility of running higher resolution experiments on larger computer clusters. Currently, the main tests are performed at a T62L64 resolution, which is equivalent to about 215 km horizontally.

- The generic LETKF core code (available at the public Google Code platform: http://code.google.com/p/miyoshi/) will be used with minimal modifications. The same core code has been coupled to a number of models with a broad range of complexity, including the Lorenz 40-variable model (Lorenz and Emanuel 1998), the SPEEDY model, and the Weather Research and Forecasting (WRF) model. The same code structure will benefit the data assimilation researches. We aim to merge the GFS-LETKF system into the existent LETKF code repository in the future.
- The observation operators can be flexibly chosen. A set of simple observation operators for conventional observation data is built in the LETKF code. For more sophisticated observation types such as the satellite radiance data, one can choose to use the GSI as the observation operator. This allows us to be able to assimilate more data. Details about the use of the GSI in the GFS-LETKF system is described in Section 4.3.3.

Figure 4.1 shows the flow chart of the GFS-LETKF system. The rectangles represent any kind of files with their formats shown in square brackets. Those rectangles are connected by arrow lines that represent program execution, with corresponding program file names shown in the bold italic font next to the arrow lines. Three main components of the system – the data assimilation cycle, the observation processing module, and the model forecast and verification modules – are boxed by

the red dashed rectangles. The data assimilation cycle is illustrated in the lower part of the figure: the 9-hour ensemble GFS model integration is executed based on the GFS sigma/surface file formats (sig/sfc), and the LETKF analysis is executed based on the gridded file format (grd). The purpose of conducting 9-hour forecasts is to perform a 4-dimensional LETKF (4D-LETKF) which assimilates asynchronous observation data at their right time within a window from hour 3 to hour 9. The source of the observation data is from the NCEP PREPBUFR dataset that not only provides the observed values but also the observation errors associated with each observation. These observation errors will be used in our system. As described before, there is flexibility of choosing observation operators. The route 1 shown in green arrows uses the built-in observation operators that can only process conventional (non-radiance) observation data. The route 2 shown in blue arrows uses the GSI as the observation operator. A set of reference model analysis data (gray rectangle) is needed in order to provide updated values of some prognostic variables that are not able to be analyzed by the atmospheric data assimilation system, such as ozone concentration and sea surface temperature (SST). In our study, the Climate Forecast System (CFS) Reanalysis (CFSR; Saha et al. 2010), which is a most advanced reanalysis dataset produced by the NCEP CFS version 2, is chosen to be this reference model dataset.

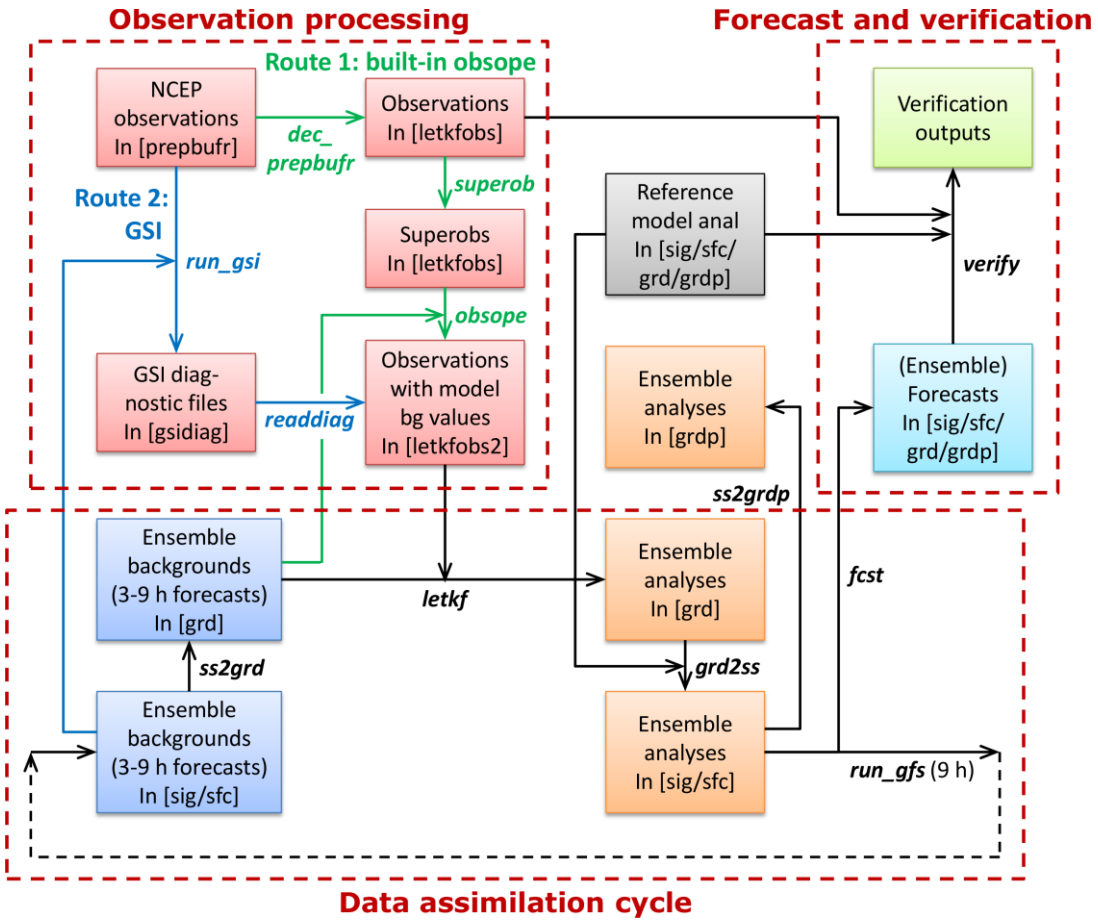

Figure 4.1: The flow chart of the GFS-LETKF system. The rectangles represent any kind of files with their formats shown in square brackets. Those rectangles are connected by arrow lines that represent program execution, with corresponding program file names shown in the bold italic font next to the arrow lines. There are two routes of the observation processing: using built-in observation operators (green arrows) and using the GSI (blue arrows). Explanation of the format abbreviations: "sig/sfc" for sigma/surface files of GFS model inputs and outputs; "grd" for gridded files in model levels that can be read by the LETKF main program and plotted with GrADS software; "grdp" for gridded files in pressure levels; "prepbufr" for the NCEP PREPBUFR observations; "letkfobs" for a special observation data format used by the LETKF code; "letkfobs2" is similar to "letkfobs" but with observation values in model backgrounds appended; "gsidiag" for the format of GSI diagnostic outputs.

4.3.2 Choice of initial ensemble

The simplest way to create an initial ensemble would be using a combination of initial conditions at different times as we did in the SPEEDY model experiments. We also design by this way to initialize the GFS-LETKF system from a random time series of any model analysis dataset[2]. At first, we used the CFSR data that we already used as the reference model analysis (gray rectangle in Figure 4.1) to initialize the system. However, the result of this trial was not satisfactory. A consistent temperature bias was observed near the tropopause which can be as large as -8 K, especially near the polar region (Figure 4.2c). It was an unacceptable huge bias that can significantly degrade the LETKF data assimilation performance. After a comprehensive examination, we found that the main cause of this large bias is the unrealistic globally mean negative water vapor concentration appeared at the lower stratosphere in CFSR (Figure 4.2a, b). This underestimate of the stratospheric water vapor resulted in the unrealistically strong longwave radiation cooling near the tropopause. The data assimilation was not able to fix the water vapor concentration at such high levels because there was hardly any moisture observation. For this reason, we have revisited our choice of the initial conditions and used the operational GFS model analysis, in

[2] Although any random time series of the model data can be chosen to generate the initial ensemble, it is recommended to use the data in the same season and same local time in order to prevent the deteriorate effects of the annual cycle and the diurnal cycle.

which the water vapor profile is more reasonable. The problem has been solved by this choice.

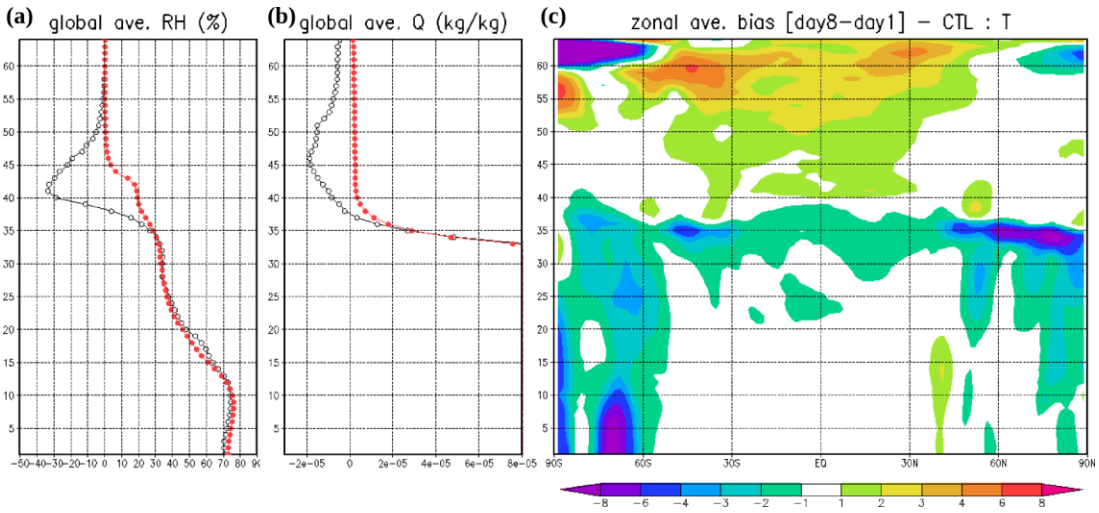

Figure 4.2: The globally averaged (a) RH (%) and (b) Q (kg kg^{-1}) profiles in the CFSR initial condition (black lines; 12Z, August 15, 2008) and in the operational GFS (red lines; 00Z, January 1, 2012). (c) The zonally averaged long-term temperature drift, computed by the day 8 output minus the day 1 output in a T62 GFS forecast initialized from random CFSR data. The vertical coordinate is the GFS model level from 1 to 64.

4.3.3 Flexible observation operators

It is relatively easy to build a set of observation operators for the conventional (non-radiance) observation data that only involve 2-dimentional or 3-dimensional interpolation. However, if we want to add the ability of assimilating satellite radiance data into our system, it is too difficult to create the observation operators that involve radiative transfer calculations. An easier route to assimilate satellite radiance data is through the mature GSI system. We can first run the GSI system in an "observer"

mode and store its diagnostic outputs that contain the information of the observation values in the model background [$\mathbf{y}^b = H(\mathbf{x}^b)$], then our program can make use of this information to compute the LETKF analysis without bothering the observation operator computation. In order to achieve this, Takemasa Miyoshi has separated the observation operator computation outside the main LETKF program in his Google Code repository, thus we can flexibly choose to use any observation operator. Daryl Kleist provided us clear instruction on how the NCEP used the GSI as an observer to develop their GFS-EnKF system. Runhua Yang did most of work to test the GSI system on our Linux cluster and to write a program to extract the information we need from GFS diagnostic files. After the cooperative work, the GSI has been coupled into the GFS-LETKF system and become an option of the observation operator (shown in blue arrows in Figure 4.1), while the option to use the simple built-in observation operators to process conventional data is still retained (green arrows in Figure 4.1). However, to date, the function of the satellite radiance data assimilation has not been finished yet. There are still some additional tasks to process the GFS diagnostic files for the satellite radiance observations whose format is more complicated than the conventional observations. In the current system, we can only use the GSI to process the conventional data.

We verify our implementation by comparing the observation increment between using built-in observation operators and using the GSI in a single LETKF update with the same set of observations. As shown in Figure 4.3, the LETKF update using two options results in similar observation increments in both patterns and magnitudes for

the u-wind (Figure 4.3a) and the sea level pressure (SLP; Figure 4.3b), indicating that the implementation of the flexible observation operators works correctly.

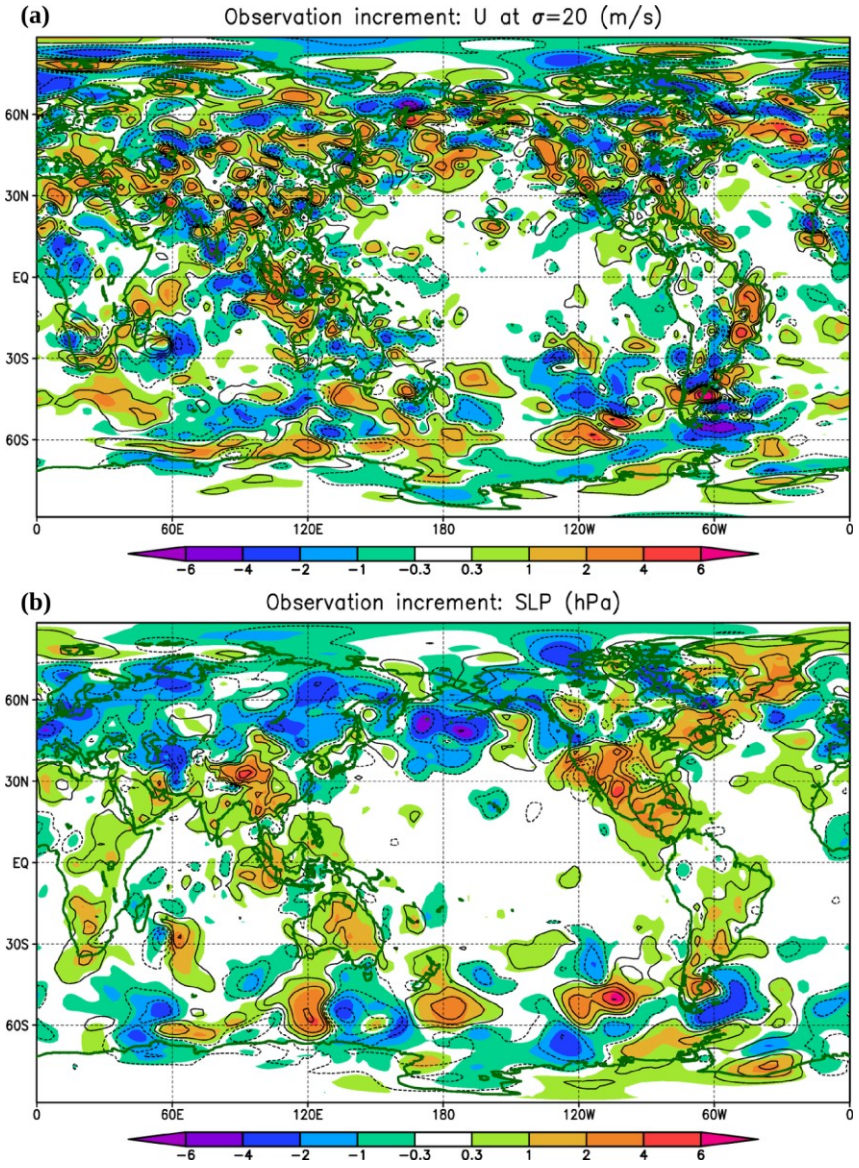

Figure 4.3: The observation increments of (a) u-wind at $\sigma = 20$ (m s^{-1}) and (b) sea level pressure (hPa) computed using the built-in observation operators (shown in shade) and using the GSI (shown in contour) in a single LETKF update.

In this study of precipitation assimilation, we use the built-in observation operators to run all of our experiments. Since we do not use any satellite radiance data, the use of the simple built-in observation operators makes the computation much faster than using the heavy GSI program.

4.3.4 Observation thinning

The NCEP PREPBUFR data are used as the observation data source. It includes all conventional observation platforms but without satellite radiance data. As shown in Figure 4.4a, c, the original PREPBUFR data are extremely dense in some particular locations, such as the continental United States and the Europe. Besides, some observations are also too dense in their vertical resolution, such as the rawinsondes in Europe (Figure 4.5a). As a result, the representativeness of the data does not fit into our low-resolution model, so it is not good to directly assimilate this original dataset from the NCEP. In the ensemble data assimilation, these dense data can also result in too small ensemble spreads and degrade the analyses in latter cycles. To alleviate the problem, the original data need to be thinned before assimilated into the model.

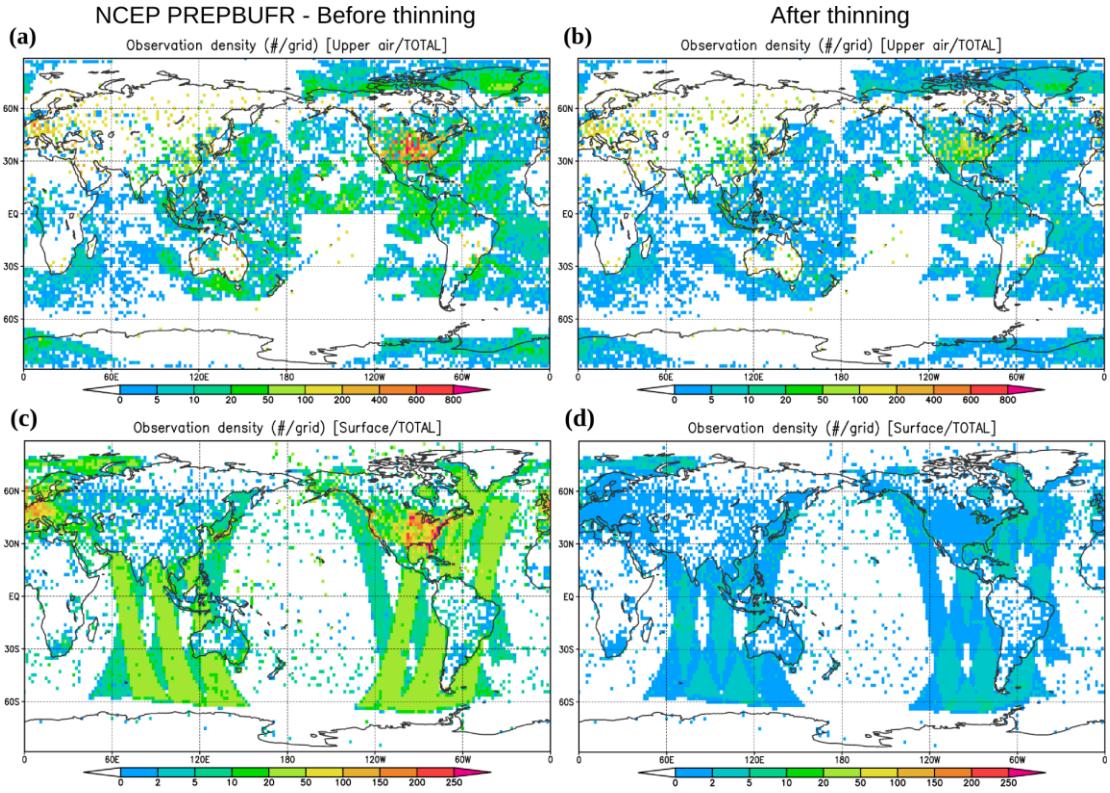

Figure 4.4: In August 2008, (a) (b) the upper-level observation densities (number of observations per column grid) and (c) (d) the surface observation densities in the NCEP PREPBUFR data before (left) and after (right) the superobing/thinning procedure.

In the GFS-LETKF system, a mixed superobing/thinning procedure is developed following a basic principle: keeping at most only one observation per (3-dimensional) model grid point/observation type/variable during one assimilation window. This procedure reduces the total observation numbers by about a third and the resultant observation density is shown in Figure 4.4b, d horizontally and Figure 4.5b vertically. When the built-in observation operators are used, it is recommended to run this superobing/thinning program before assimilating the NCEP PREPBUFR data. When the GSI is used, since GSI can also perform the observation thinning during the

observation operator computation, we can simply enable observation thinning in the GSI and achieve similar results.

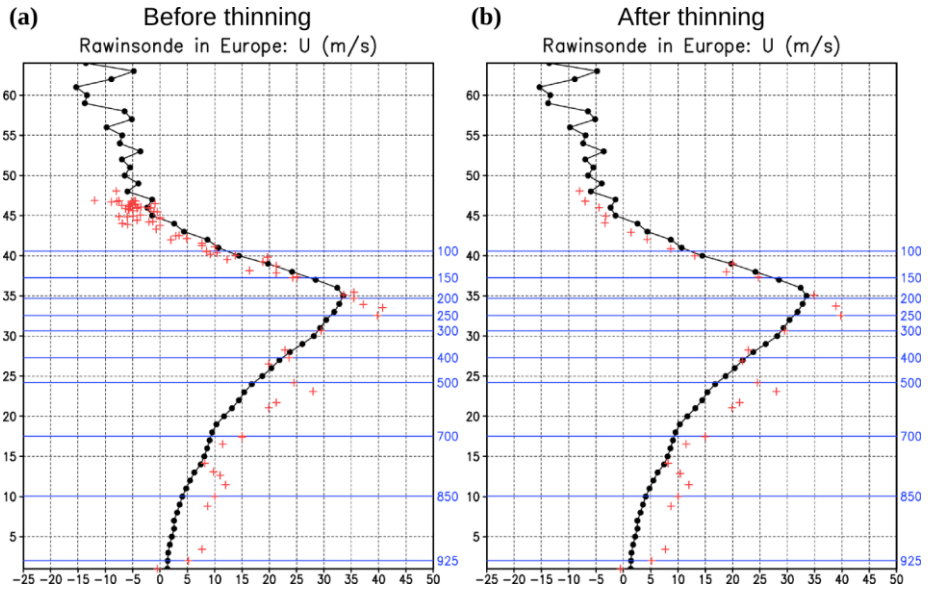

Figure 4.5: The vertical sample points (red plus signs) of u-wind data in a random rawinsonde observation in Europe (a) before and (b) after the superobing/thinning procedure. The black dots and lines are the u-wind vertical profiles in the model background. The left vertical coordinate (black) is GFS model levels from 1 to 64; the right vertical coordinate (blue) is pressure levels (hPa).

4.3.5 Modifications to prevent system blow-up

During the development, we found that the GFS-LETKF system tends to blow up after about 2 months of the cycling data assimilation run. After careful examination, it is concluded that there are two main causes of the problem: the quasi-constant adaptive inflation parameter and the unrealistically large moisture spread in the tropical regions, and these two problems are actually tied together.

The adaptive inflation (Miyoshi 2011) assumes slowly evolving observing network, so the inflation takes place quasi-constantly over the cycles. However, the observing network in the real world changes rapidly. The amount of rawinsonde observations significantly varies between 00, 12Z and 06, 18Z, and several types of satellite observations (e.g., air motion vectors) just appear randomly. At some locations, for example, the adaptive inflation estimates a factor of 4 multiplicative inflation parameter based on the previous several month cycling run. This factor will keep almost constantly cycle by cycle. Then, with some bad luck, at some cycle almost all surrounding observations within the localization length are gone, thus the analysis ensemble spread would increase by a factor of 4 in this cycle (because there is no observation to reduce the spread in the same time). The unrealistic ensemble spread will lead to unrealistic assimilation increment in the subsequent cycles, and will result in unrealistic values of model variables. Eventually the model can crash because of the unrealistic initial conditions.

In order to alleviate this problem associated with the inflation, we add a "relaxation to prior" scheme proposed by Zhang et al. (2004) that relaxes the analysis ensemble perturbation in the EnKF ($\mathbf{X}^a$) to the background ensemble perturbation ($\mathbf{X}^b$) based on a weight constant α that can be optimally chosen:

$$\mathbf{X}^a \leftarrow (1-\alpha)\,\mathbf{X}^a + \alpha\,\mathbf{X}^b\,. \tag{4.1}$$

In the LETKF, it is equivalent to replacing the weight matrix $\mathbf{W}^a$ with a weighted average of it and the identity matrix:

$$\mathbf{W}^a \leftarrow (1-\alpha)\,\mathbf{W}^a + \alpha\,\mathbf{I}\,. \tag{4.2}$$

Note that the adaptive inflation is still functioning at the same time, which means that the adaptively estimated multiplicative inflation factor is still used in the LETKF calculation. This "relaxation to prior" method can smooth the evolution of the ensemble spreads. In our precipitation assimilation experiments, the α value is chosen to be 0.5.

Although this modification can stabilize the system and extend the period of the successful cycling run, it can still randomly blow up when the low-level moisture spread becomes unrealistically large. We observe this problem repeatedly happens over the tropical land regions such as the central Africa. Without a better solution, we add an artificial constraint on the ensemble spread of moisture: when the standard deviation of the specific humidity is greater than 0.7 times of its ensemble mean value, the spread is relaxed to this limit. The modification greatly stabilizes the system.

4.3.6 Verification

The forecast and the verification packages are included in the GFS-LETKF system. Deterministic or ensemble forecasts of any length can be conducted every cycle based on the mean or ensemble LETKF analyses. After the forecasts finish, one can choose to use any model analysis, such as the CFSR, or rawinsonde observations as reference states to compute the RMS errors, average absolute errors, biases in terms of several variables. The verification regions can also be flexibly chosen.

4.3.7 Forecast sensitivity to observations

A package to compute the ensemble forecast sensitivity to observations (EFSO; Kalnay et al. 2012; Ota et al. 2013) developed by Daisuke Hotta is also included in

the GFS-LETKF system. We will use this tool to compute the EFSO of each precipitation observation in Chapter 7. The formulation of the EFSO will be described in Chapter 7.2.

4.4 Benchmark tests

A few preliminary test experiments assimilating conventional observations are conducted to evaluate the performance of the GFS-LETKF system.

4.4.1 Forecast verification

An initial ensemble is created at 00Z January 1, 2008 from a random time series of operational GFS initial conditions. After one month spin-up, we conduct 5-day forecasts initialized from ensemble mean analyses every cycle from February 1–10, 2008, and the average forecast errors verified against rawinsonde observations are computed for the globe and for three regions: the Northern Hemisphere extratropics (20–90N), the tropics (20N–20S), and the Southern Hemisphere extratropics (20–90S). Another set of forecasts are also conducted using the same T62L64 GFS model but with initial conditions from the CFSR, and the same verification is computed. The CFSR is expected to be a higher quality analysis dataset than our GFS-LETKF analysis because it was produced at a native T382L64 resolution and it assimilated much more observation data.

Figure 4.6 shows that the forecasts from GFS-LETKF are worse than those from CFSR in u-wind, temperature, and humidity by about 12–18 hour lead time, but the difference in forecast errors is not growing with time. The difference could arise from the lack of the satellite radiance data assimilation in our current GFS-LETKF system

and the big difference in native resolutions (i.e., T62 in GFS-LETKF vs. T382 in CFSR) of the data assimilation system. The important role of the satellite radiance data assimilation can be assessed from the verification results for different regions (Figure 4.7). It shows a smaller skill difference in the Northern Hemisphere extratropical region but a larger skill difference in the Southern Hemisphere extratropical region, where the conventional observation data are sparse so that the satellite data are essential. Giving the above explanation, we believe that our GFS-LETKF system has reached reasonable analysis and forecast accuracy with its relatively low resolution and smaller observation usage.

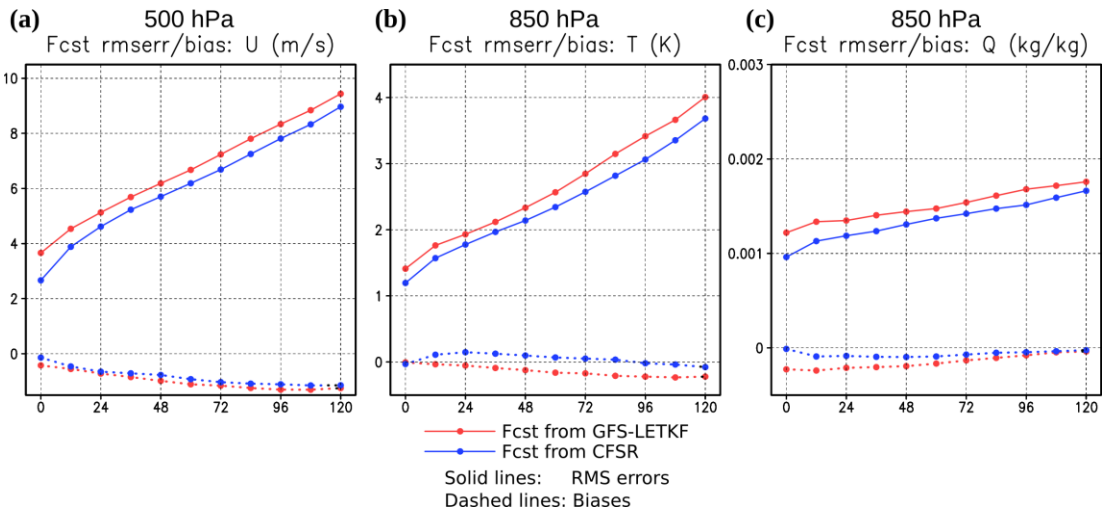

Figure 4.6: Using a T62L64 GFS model, the average global root-mean-square forecast errors (solid lines) and biases (dashed lines) versus forecast time initialized from T62 GFS-LETKF analyses (red lines) and CFSR (blue lines): (a) 500-hPa u-wind (m s^{-1}) (b) 850-hPa temperature (K) (c) 850-hPa specific humidity (kg kg^{-1}).

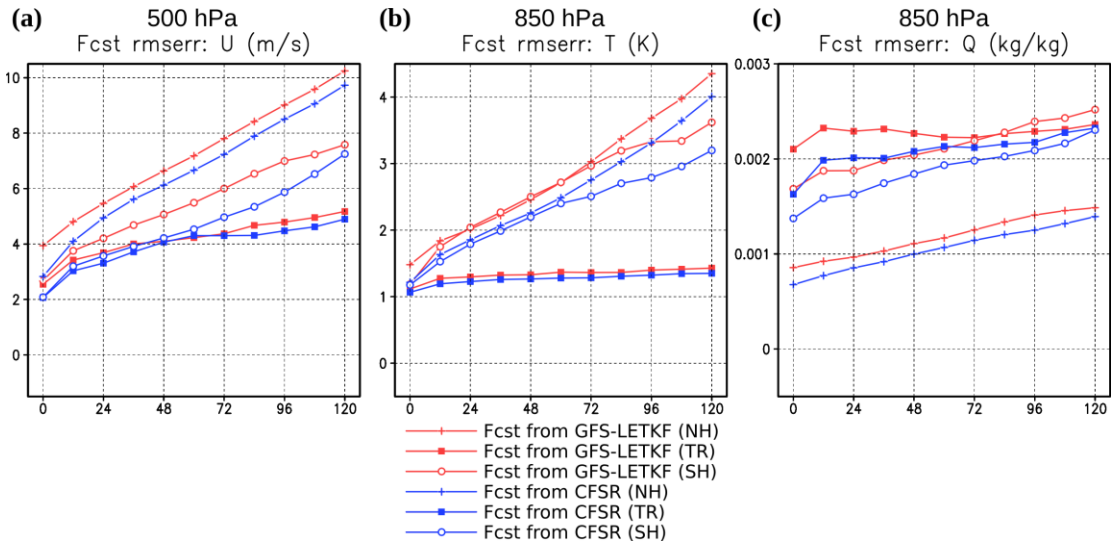

Figure 4.7: As in Figure 4.6, but for root-mean-square forecast errors averaged over three difference regions: the Northern Hemisphere extratropics (NH; 20–90N), the tropics (TR; 20S–20N), and the Southern Hemisphere extratropics (SH; 20–90S).

4.4.2 Resolution dependence

In addition to the test experiments at the T62 resolution described in the previous subsection, experiments at a T126 resolution are also conducted for the same period. Three new forecast experiments are introduced here, using a T126 GFS as the forecast model but initialized from different analysis data, including the T126 GFS-LETKF analyses (blue lines in Figure 4.8), T62 GFS-LETKF analyses (green lines), and the T382 CFSR (purple lines). The other two forecast experiments using the T62 GFS model that we have already seen in the previous subsection are also plotted in Figure 4.8 for reference (red lines: initialized from T62 GFS LETKF analyses; gray lines: initialized from the T382 CFSR). Therefore, Figure 4.8 shows an overall

comparison among different resolutions of data assimilation systems and resolutions of forecast models.

As expected, it is found that the initial analysis errors depend mostly on the resolution of data assimilation systems, and the error growth rates depend mostly on the resolution of forecast models. The errors grow slower when a higher resolution model is used. As a result, for longer-term forecasts (> 48 hour), the resolution of forecast models is more important than the resolution of data assimilation systems used to produce the analyses (green vs. red lines), although the higher-resolution data assimilation system also brings essential benefits (blue vs. green lines). Besides, the CFSR analyses are still considerably superior to our GFS-LETKF analyses at the T126 analysis resolution (blue vs. purple lines). In addition, as shown in the vertical profiles of the forecast errors (Figure 4.8b), forecasts initialized from the CFSR are relatively more accurate at the altitude of upper troposphere, as compared to the forecasts initialized from our GFS-LETKF system, presumably due to the beneficial use of the satellite radiance data in the CFSR.

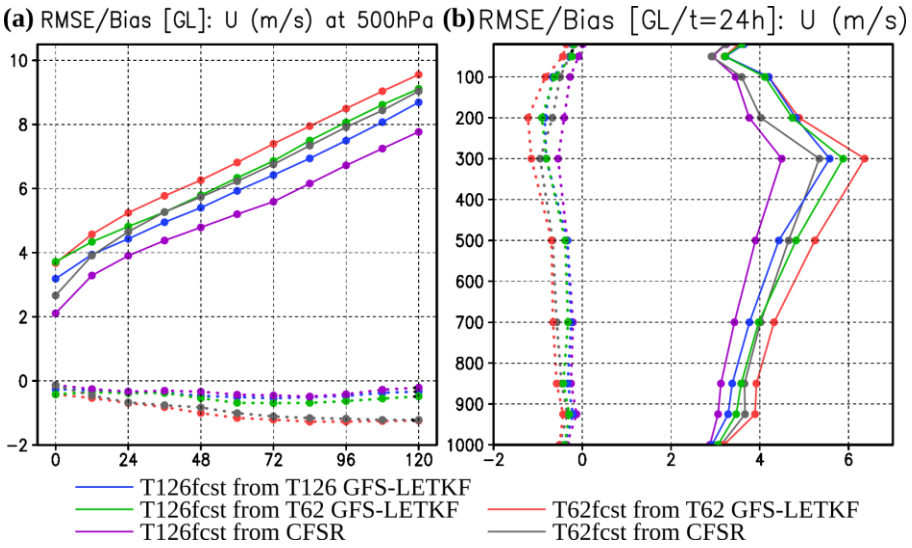

Figure 4.8: (a) The average global root-mean-square forecast errors (RMSEs; solid lines) and biases (dashed lines) of 500 hPa u-winds (m s^{-1}) versus forecast time for experiments with different analysis and forecasta resolutions: (1) Using a T126 GFS as the forecast model, forecasts are initialized from T126 GFS-LETKF analyses (blue lines), T62 GFS-LETKF analyses (green lines), and the CFSR (purple lines). (2) Using a T62 GFS as the forecast model, forecasts are initialized from T62 GFS LETKF analyses (red lines) and the CFSR (gray lines). (b) Same as (a), but for average RMSEs (solid lines) and biases (dashed lines) of u-winds (m s^{-1}) at various vertical levels in the 24-hour forecasts.

Chapter 5: Assimilation of real precipitation observations I - Challenges and possible solutions

5.1 Introduction

The next three chapters are on the real precipitation assimilation experiments. With a realistic model and real satellite observation data, there are much more challenges compared to the OSSEs with the SPEEDY model. Therefore, a naïve replication of the SPEEDY model experiments but with the real model and observations would not lead to acceptable results. Instead, in the first step, it is a good idea to investigate and isolate those challenges with the real model and observations, and to understand the differences between the idealized and realistic settings. After we sufficiently understand these issues, we can propose possible solutions to overcome them. Following this logic, in this chapter we will first introduce the characteristics of the satellite precipitation dataset that will be used in the assimilation and discuss several expected challenges, then we will show several statistical results between the precipitation variables in the model background and in the observations in order to investigate and narrow down the challenges in our proposed real precipitation assimilation system. We will also discuss the possible solutions to these issues.

5.1.1 The TRMM Multi-satellite Precipitation Analysis

We choose to use the TRMM Multi-satellite Precipitation Analysis (TMPA; Huffman et al. 2007, 2010) for our real precipitation assimilation experiments. It is a gridded precipitation dataset compiled from multiple satellite sensors. It has a global

coverage from 50S to 50N with a homogeneous 0.25-degree spatial resolution and a 3-hour temporal resolution. The primary data sources are the low-earth-orbit (LEO) satellites such as the Microwave Imager (TMI) on TRMM, Special Sensor Microwave Imager (SSM/I) on Defense Meteorological Satellite Program (DMSP) satellites, Advanced Micro-wave Scanning Radiometer-Earth Observing System (AMSR-E) on Aqua, and the Advanced Microwave Sounding Unit-B (AMSU-B) on the National Oceanic and Atmospheric Administration (NOAA) satellite series. These microwave satellite data have a strong physical relationship to the hydrometeors and thus the surface precipitation, but they are spatially and temporally inhomogeneous. To fill the gaps left from the LEO sensors, the infrared (IR) data collected by the geosynchronous-earth-orbit (GEO) satellites are used as the secondary data sources, though the accuracy of precipitation derived from the IR is lower. In addition, in the research version (i.e., not in real time) of the TMPA, these satellite-derived precipitation amounts are further rescaled based on several monthly rain gauge analyses to achieve accurate statistics in the climatological scale. Due to the limit of the satellite measurements, the errors inherent in the finest scale estimates are large. The most successful use of the TMPA data is when the analysis takes advantage of the fine-scale data to create time/space averages appropriate to the user's application (Huffman et al. 2010).

With the above data processing procedure, the TMPA has very high data coverage rate (Figure 5.1a), making itself a potentially good data source for global precipitation assimilation. In our real precipitation assimilation study, we use the version 7 of the TMPA research products, labeled as 3B42, released in 2012

(Huffman and Bolvin 2013). The data is available for the period from January 1998 to present. The climatological mean daily precipitation computed from the 14-year TMPA data (1998-2011) is shown in Figure 5.1b.

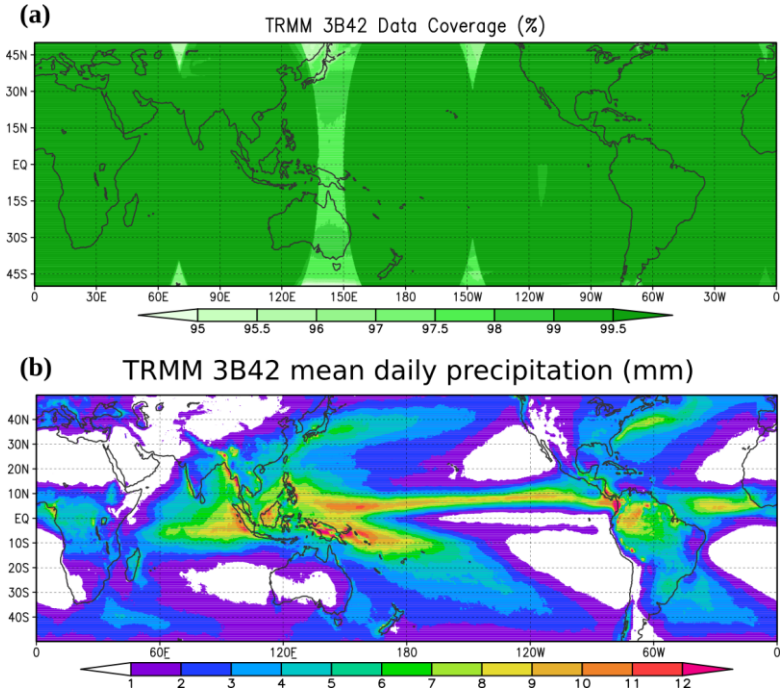

Figure 5.1: (a) The data coverage rate (%) and (b) the mean daily precipitation (mm) of the 14-year (1998-2011) TRMM Multi-satellite Precipitation Analysis.

5.1.2 Problems we face with real data and models

Since the SPEEDY model experiments in Chapter 3 are conducted within an identical-twin OSSE framework, their most serious drawback would be the assumption of perfect models. In reality, we know that the precipitation parameterization in the models is far from perfect, thus the model error of precipitation is large. Specifically, the convective model precipitation output come from cumulus parameterization and/or microphysical parameterization. The cumulus

parameterization diagnoses precipitation mainly based on the vertical thermodynamic profile at the model grids. It is a rougher method but is the only solution to simulate precipitation when the model grid spacing is greater than 10 km. When the model resolution is increasing, the convection can be more explicitly resolved, thus we can rely more on the microphysics parameterization to simulate precipitation. The precipitation simulated by these two methods can have different error characteristics: for example, common problems of the cumulus parameterization include the underestimate of the contribution and frequency for heavy precipitation, the overestimate of them for light precipitation, and incorrect timing of the precipitation (Dai 2006). Although it is believed that the precipitation simulated by microphysics parameterization is more reasonable, due to the insufficient resolution, in most of current global models the precipitation is still simulated by the cumulus parameterization. Meanwhile, our focus is also the large-scale precipitation in a low-resolution global model, so the issues of model errors we deal with is from the cumulus parameterization. In higher-resolution models, the challenges and the strategies may change.

In addition, the observation error of the precipitation data is another tough problem. Not only is the error magnitude large in the satellite retrieval products, but the characteristics of the error in the retrievals is also mostly unknown: the observation error of precipitation can vary with location, time, precipitation amounts, and precipitation types, and it can also be very non-Gaussian. There have been several studies to validate the in satellite precipitation estimates and to quantify the biases and errors (Bauer et al. 2002; Bowman 2005; Ebert et al. 2007). The error

magnitude is typically very large as compared to other conventional observations used in the data assimilation, but it varies very much when different grid sizes and validation time intervals are chosen. To give an idea of the error magnitude, for individual TRMM satellite overpasses averaged over a 1° × 1° box, the relative RMS difference with respect to a rain gauge centered in the box is as high as 200% to 300% (Bowman 2005), which is much larger than what we used in the SPEEDY experiments (20% or 50%). However, by combining information from multiple satellite sensors, averaging raw data in space and/or in time, the errors can be reduced. Tian and Peters-Lidard (2010) estimated the lower bound of the uncertainties of satellite-based precipitation measurements in each 0.25° grid over the globe by computing the variance from six different satellite precipitation datasets. They concluded that the uncertainties are relatively small (40–60%) over the oceans, especially in the tropics, and over the lower-latitude South America. Large uncertainties (100–140%) exist over high latitudes, especially during the cold season. High relative uncertainties also persist over complex terrains such as the Tibetan Plateau, the Rockies and the Andes, and near the coastline region. More sophisticated error models categorizing the errors into three components, including hit bias, missed precipitation, and false precipitation, have also been proposed to better quantify the errors is the satellite precipitation estimates (Tian et al. 2009; Maggioni et al. 2013).

However, the above studies are not sufficient to determine the observation errors and error characteristics of the precipitation observations when used in the data assimilation, because the meaning of the "observation error" in the data assimilation could be different from these studies. There are at least two components of the

"observation error" that must be considered in the data assimilation formulation: the instrumental error and the representativeness error (Ide et al. 1997; Errico et al. 2007). For a satellite retrieval quantity, the "instrumental error" is loosely defined. We recognize that the main issue regarding the observation errors of precipitation is not investigated in this study. It is a very difficult problem and has not been solved yet. In this study, we follow similar strategy as Lopez (2011, 2013): a simple constant value is used for the observation error of all precipitation observations after the variable transformation (either the logarithm transformation or the Gaussian transformation). The underlying hypothesis is that after the precipitation transformation, the observation errors is more uniform (Mahfouf et al. 2007). We first conduct many trials to obtain the best value for the precipitation observation error and then use it in our experiments. We think that a better way to address this issue is to use some kind of adaptive methods associated with the data assimilation system to objectively determine the observation error of precipitation. For example, Li et al. (2009) demonstrated a method to estimate the optimal observation errors with the EnKF. Applying such methods to estimate the observation error of satellite precipitation data could be an interesting study.

5.1.3 Strategies to overcome these problems

As discussed, both the model precipitation and the precipitation observations may have large errors, so the long-term statistics of these two quantities may be very different, which is harmful to the data assimilation use. In this data assimilation study, we are not attempting to improve either the model or the observations. Our main goal is to optimally use this imperfect observation dataset in this imperfect model, to

improve the model forecasts in both precipitation and non-precipitation variables. To achieve this goal, we follow two simultaneous goals:

1) For those observations that are more compatible with the model background, some bias correction scheme could be applied to make the model and observed precipitation have similar climatological distributions.
2) For those observations that are deemed to be too bad to be used, we should define useful quality control criteria to reject these observations. Note that the statement "an observation is bad for assimilation" is not necessarily because the observation itself is bad, but could also be because the model is not good enough to use this observation in that location and time.

In addition, the method of Gaussian transformation and the criterion that requires enough precipitating background members that we proposed in the SPEEDY model experiments are still applied to the real precipitation assimilation to overcome the non-Gaussianity problem. In particular, we will verify the validity of these methods by the Gaussianity statistics in Chapter 5.4. This argument was absent in our SPEEDY model experiments. Several statistical results of precipitation are presented in the following sections in order to identify the problems and support the above-mentioned strategies especially for our proposed configuration of precipitation assimilation with the GFS-LETKF.

5.2 Joint probability distribution diagram statistics

In the beginning of the precipitation statistics, we plot joint probability distribution diagrams to see the inconsistency between the model background precipitation and the precipitation observations. To ensure an apple-to-apple

comparison, a large sample of "model background values" and "observation values" of precipitation is created by the method shown in Figure 5.2. For observations, 10-year (2001–2010) data are collected to form a series of observations. The original TMPA data are provided with the 3-hourly precipitation rate at a 0.25-degree longitude-latitude resolution. We first change (upscale) the original TMPA grids to the T62 or T126 Gaussian grids used by the GFS model using an areal conservative remapping, and then we can choose to either use the instantaneous precipitation rate as in its original form, or use the 6-hour accumulated precipitation amount. The 6-hour accumulated precipitation centered at time t is computed by

$$\mathrm{P(6h)}_t = \frac{3}{2}\mathrm{Pr}_{t-3} + 3\,\mathrm{Pr}_t + \frac{3}{2}\mathrm{Pr}_{t+3}\,, \tag{5.1}$$

where Pr_t is the precipitation rate at time t in unit mm h^{-1}. The different joint PDF properties between the precipitation rate and the accumulated precipitation will be discussed later. On the other hand, for model backgrounds, we conduct a series of 9-hour GFS model forecasts at desired resolutions (T62 or T126 in this study) every 6 hours initialized from the same 10-year (2001–2010) CFSR reanalysis data, then the 3 to 9 hour forecasts are collected to form a series of model background. It is noted that these 3 to 9 hour forecast data are exactly what we use as model backgrounds in the 4D-LETKF data assimilation, so they can lead to meaningful statistics from the point of view of data assimilation. The GFS model generates forecast fields every hour and its precipitation output is also in the form of the instantaneous precipitation rate. We can pick up the precipitation rates every 3 hours corresponding to the TMPA observations, or we can compute the 6-hour accumulated precipitation centered at time t by

$$\mathrm{P(6h)}_t = \frac{1}{2}\mathrm{Pr}_{t-3} + \sum_{t\prime=t-2}^{t+2} \mathrm{Pr}_{t\prime} + \frac{1}{2}\mathrm{Pr}_{t+3}\ , \tag{5.2}$$

then they can be directly compared to the observations.

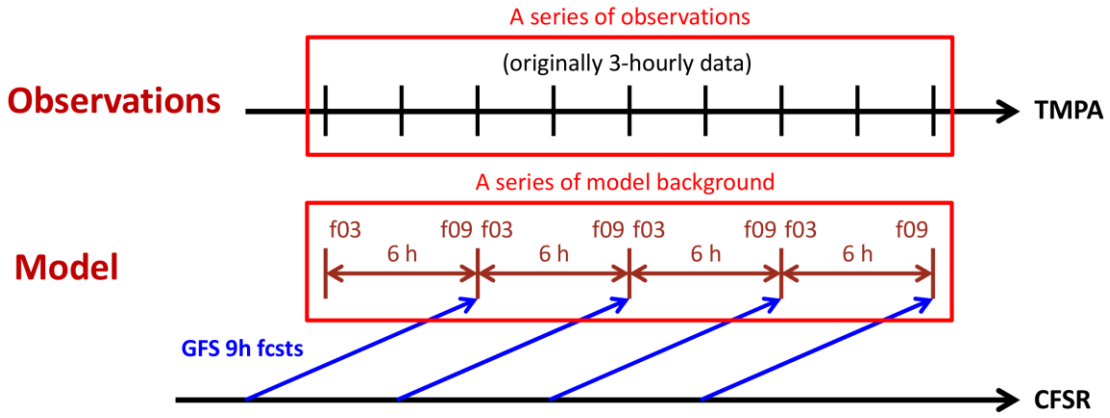

Figure 5.2: Formation of samples of precipitation in the 10-year TMPA and the GFS model background.

Figure 5.3 shows the joint probability distribution diagrams between the 6-hour accumulated precipitation in the T62 GFS model background and in the TMPA data upscaled to same T62 grids. Different transformation methods are used in each subplot. Only positive precipitation is shown in the figures because when the zero precipitation is also plotted, it just adds two saturated lines along the x-axis $(\tilde{y}, \tilde{y}_{\mathrm{zero}})$ and y-axis $(\tilde{y}_{\mathrm{zero}}, \tilde{y})$ representing the abundance of zero precipitation in either the model background or the observation data (not shown). We expect that the maximum probability regions should be located along the one-to-one diagonal line for a usual variable that is useful for data assimilation. However, when the joint probability distribution diagram is plotted without a transformation method (Figure 5.3a), we barely see any correlation in precipitation between the model background and the

observations[3]. The probability of the small precipitation amounts is saturated and not oriented along the one-to-one line. This could partly explain why the precipitation is not a good variable for data assimilation and a transformation of precipitation is normally needed. When the precipitation is logarithm-transformed before the plotting (Figure 5.3b), the curved line of the maximum probability (red dashed curve) is nicely seen. This maximum probability curve is off from the one-to-one line, indicating a value-dependent positive bias of the model precipitation as compared to the TMPA data. As discussed in Chapter 5.1, we are not to argue either the model precipitation or the TMPA data is more correct, but it is better to remove this bias before the data assimilation. An interesting fact is that when the "modified" logarithm is used [i.e., a constant $\alpha = 0.6$ mm $(6h)^{-1}$ is added in the transformation; refer to Equation (2.1)] (Figure 5.3c), the saturation in the small precipitation amounts is seen again, yet the maximum probability curve near the one-to-one line is still retained but less obvious. The constant α is required when the logarithm transformation is used in the data assimilation, and $\alpha = 0.6$ mm is the value that leads to the best experimental results in the precipitation assimilation experiments that we will show in Chapter 6. However, from this joint probability distribution diagram, it is inferred that the use of the constant α in the logarithm transformation makes the behavior of the transformed variable in the small precipitation amounts similar to the original variable and thus reduce the discrimination in the small amounts.

[3] In this case, the R^2 value computed from the linear regression shown in the figure is not particularly meaningful, since the correlation largely comes from the off-diagonal regions.

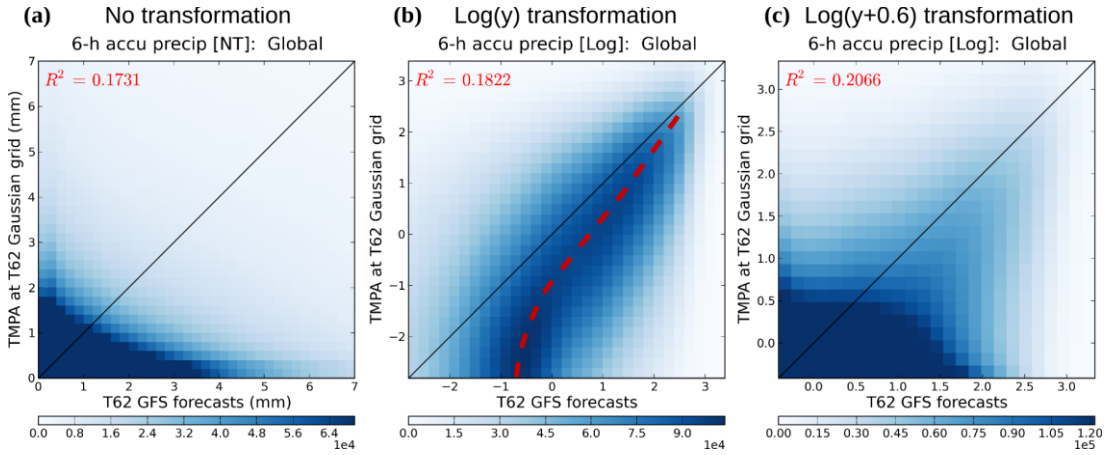

Figure 5.3: The joint probability distribution of the 6-hour accumulated precipitation with different transformation methods between the T62 GFS model background and the TMPA data upscaled to same T62 grids. (a) No transformation (b) exact logarithm transformation [$\alpha = 0$ in Equation (2.1)] (c) "modified" logarithm transformation ($\alpha = 0.6$ mm) is applied to the precipitation variables. Only positive precipitation is shown in all figures.

Figure 5.4 shows the same diagrams but for the comparison between the instantaneous precipitation rate and the 6-hour accumulated precipitation ($\alpha = 0$ in the logarithm transformation). As shown in Figure 5.4a, the correlation with the precipitation rate is worse than that with the accumulated precipitation amount. In particular, a multimodal feature is seen in the model precipitation. The precipitation rate produced from the T62 GFS model tends to be concentrated at several ranges (-3 to -2, -1.5 to -1, and 0 to 1 in the transformed value), which could be related to some deficiencies of the precipitation parameterization at this low resolution. The lower correlation may also be resulted from the timing error of the precipitation parameterization scheme. The instantaneous precipitation rate is too sensitive to the timing error while it is common for the precipitation produced from the cumulus

parameterization. For example, Chao (2013) showed that the cumulus precipitation scheme can have large systematic errors in the precipitation diurnal cycle over the land. Therefore, although the accumulation of precipitation discards the information of the time variation of the precipitation within the 6-hour assimilation window, the 6-hour accumulated value of precipitation would still be a better variable than the precipitation rate when used in the data assimilation. The successful assimilation of precipitation demonstrated by Lopez (2011, 2013) also used the 6-hour accumulated precipitation. Nevertheless, we note that the model resolution we use is a fairly coarse T62, and the precipitation parameterization could perform better in a higher resolution model.

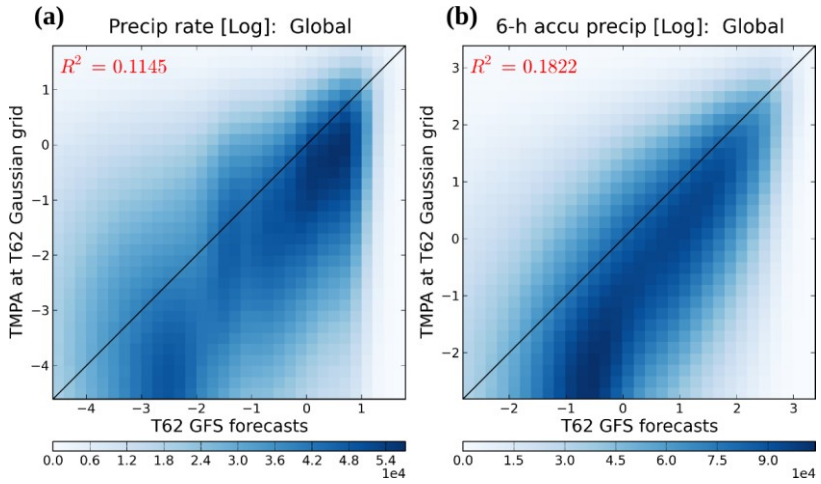

Figure 5.4: The joint probability distribution of the logarithm-transformed (a) instantaneous precipitation rate (mm h^{-1} in its original value) and (b) 6-hour accumulated precipitation (mm in its original value) between the T62 GFS model background and the TMPA data upscaled to same T62 grids. Only positive precipitation is shown in all figures.

The same diagram but plotted with higher resolution results in shown in Figure 5.5b. In this case, we redo all the processes in Figure 5.2 at a T126 resolution; i.e., the GFS model forecasts are conducted at the T126 resolution and the TMPA data are upscaled to the same T126 grids. At this resolution, the correlation is actually slightly lower than that at the T62 resolution, which probably due to the larger random error in the higher resolution model and observation data. By spatially averaging the field, this random error can be reduced (Huffman et al. 2010). It does not mean that the higher resolution model or observations are useless, but it is kind of a "trade-off" between the resolution and errors. For our purpose of assimilating global large-scale precipitation to improve the model forecasts, a spatially averaged lower-resolution variable could be sufficient.

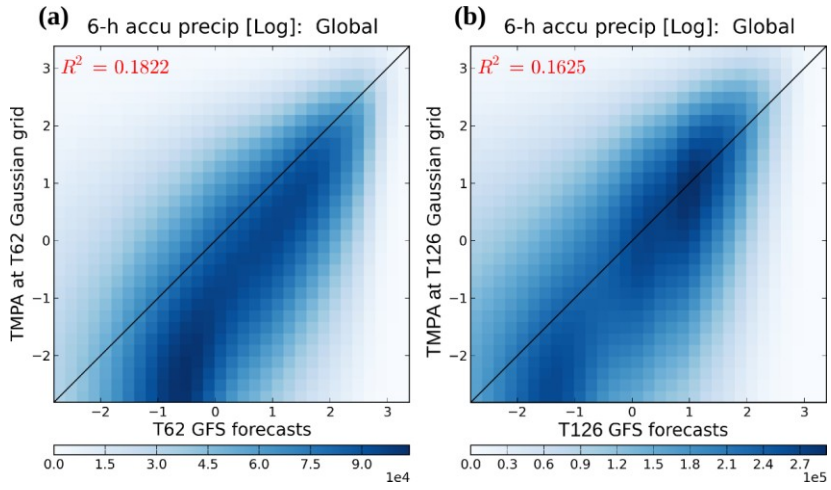

Figure 5.5: As in Figure 5.3, but for logarithm-transformed precipitation at (a) a T62 resolution and (b) a T126 resolution in both the GFS model background and the TMPA data.

5.3 *Separate Gaussian transformations applied to model background and observations*

From this section the Gaussian transformation of the precipitation with the realistic GFS model and TMPA observations are introduced. We apply the same Gaussian transformation technique to this case as we did in the SPEEDY model experiments but with a little modification: the transformations are defined separately for model backgrounds and observations. Specifically, the transformation of the model precipitation is performed based on the CDF computed from the model climatology; and the transformation of the precipitation observations is performed based on the CDF computed from the observation climatology. We use the same 10-year (2001–2010) sample prepared in the previous section to compute the CDFs of model and TMPA precipitations for each T62 grid point and each 10-day period of year (3 periods per month; 36 periods in total), and define their own transformations as functions of locations and time by:

$$\tilde{y} = F^{G^{-1}}[F(y; \text{location, period of year})] \,. \tag{5.3}$$

Here the precipitation values that are less than 0.06 mm $(6\text{h})^{-1}$ are regarded as "zero precipitation" [i.e., $y_{\text{trace}} = 0.06$ mm $(6\text{h})^{-1}$; refer to Equation (2.9)]. In the SPEEDY model experiments, there was no consideration of separate transformations because it was an identical-twin configuration so that the two CDFs are theoretically identical. In addition, with the real data containing large spatial and temporal variabilities, we like to have a more "continuous" CDF field smoothly varying in space and time, so when computing the CDF at each grid point and each period, all data within 500-km radius and ± 2 periods (± 20 days) are considered as a whole set of samples in order to

obtain the smoothed field. This choice also increases the sample sizes and thus reduces the sample errors. Although it helps us to construct a smooth CDF field and thus a more continuous definition of the Gaussian transformation, the disadvantage of this method is that the transformation would be not good in the regions with intrinsically large gradient of precipitation climatology, such as regions with complex terrain and orographic precipitation.

Before showing the statistical results with the Gaussian-transformed precipitation, we first take a look of the CDF fields we construct from the 10-year model and observation data. Figure 5.6 shows an example of maps of precipitation amounts at various cumulative distribution levels in the period of February 1–10 in both the TMPA data and the T62 GFS model backgrounds. By comparing the fields at same cumulative distribution levels, it is clearly found that the model has positive bias as compared to the observations as concluded in the previous section (the amounts in Figure 5.6b, d, f are generally greater than those in Figure 5.6a, c, e). In terms of patterns, the CDF fields of the model and the observations agree reasonably well in most regions. However, in some particular regions, they actually have large disagreement. The regions can be more highlighted in maps showing the zero precipitation probability. As shown in Figure 5.7, the most significant differences in the zero precipitation probability between the model and the observations are observed over where the marine stratocumulus is formed, including the subtropical eastern Pacific in both northern and southern hemispheres, and the subtropical eastern Indian Ocean. In the TMPA data, it rarely rains in these regions (about 80% probability of zero precipitation or 20% probability of positive precipitation), but in

the model it has too frequent drizzle (about 30% probability of zero precipitation or 70% of positive precipitation). Based on our understanding of the marine stratocumulus (vanZanten et al. 2005; Leon et al. 2008), the reality favors the TMPA data and it poses a question on the GFS model results. The precipitation parameterization in the T62 GFS model may be incapable to correctly simulate the marine stratocumulus precipitation. Nonetheless, again we are not to improve the model or observations. A reasonable strategy would be not using the precipitation data in these regions during the assimilation, since the disagreement between the model background and the observations is huge.

With the Gaussian transformation of the model precipitation and the TMPA precipitation, the joint probability distribution diagrams are shown in Figure 5.8. Figure 5.8a and d are the global results. Figure 5.8a uses logarithm transformation which we already seen (same as Figure 5.3b) and Figure 5.8d is the same figure plotted with the Gaussian transformed variables. It is shown that with the Gaussian transformation, the distribution of the precipitation variables become more normal, the maximum probability curve becomes more collocated with the one-to-one line (i.e., the biases are removed), and the correlation (R^2 value) becomes slighter higher. In our transformation method defined for model and observations separately, the model climatology and the observation climatology are first converted to the same 0–1 scale (cumulative distribution), then the same $F^{G^{-1}}$ is applied to obtain the Gaussian variables. Therefore, this method can essentially remove the value-dependent bias as seen in Figure 5.8a. We would call this method a "CDF-based bias correction."

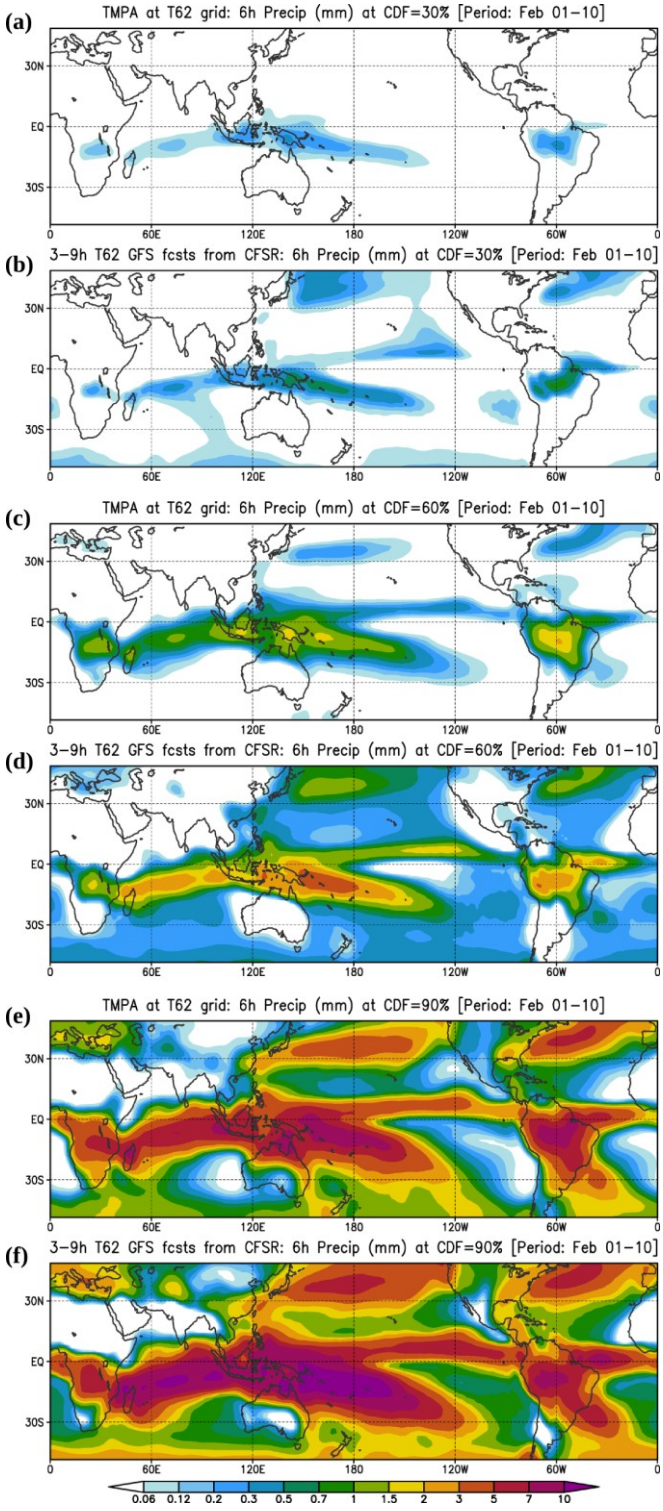

Figure 5.6: The maps of precipitation amounts (mm) at (a) (b) 30%, (c) (d) 60%, and (e) (f) a 90 % cumulative distribution levels in the period of February 1–10 in (a) (c) (e) the TMPA data and (b) (d) (f) the T62 GFS model backgrounds.

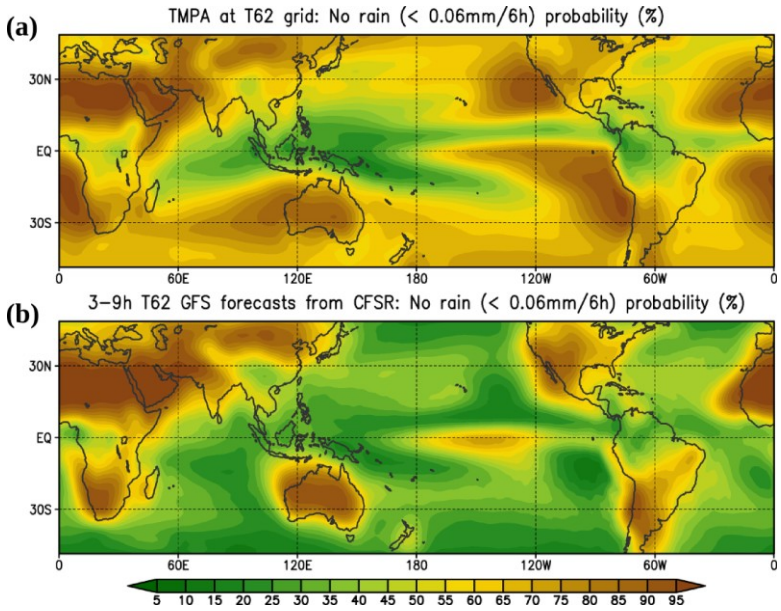

Figure 5.7: The maps of (all-season) zero precipitation probability (%) in (a) the TMPA data and (b) the T62 GFS model backgrounds.

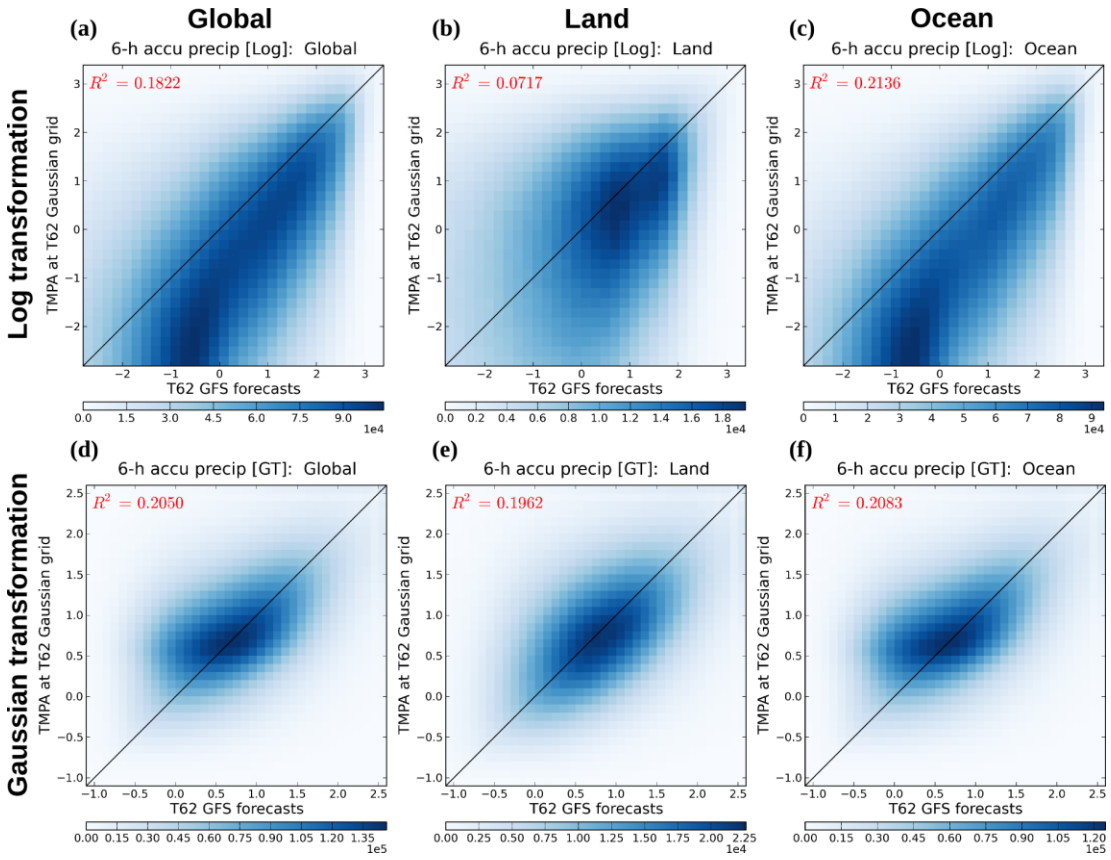

Figure 5.8: The joint probability distribution of (a)-(c) the logarithm-transformed ($\alpha = 0$) and (d)-(f) the Gaussian-transformed 6-hour accumulated precipitation between the T62 GFS model background and the TMPA data upscaled to same T62 grids. (a) (d) Global results; (b) (e) only the precipitation over the land; (c) (f) only the precipitation over the ocean. Only positive precipitation is shown in all figures.

We can change the validation regions based on the land/ocean distribution and the latitude. The same diagrams are plotted with land data only (Figure 5.8b, e), ocean data only (Figure 5.8c, f), the northern hemisphere extratropics (20–50N; Figure 5.9a, d), the tropical regions (20N–20S; Figure 5.9b, e), and the southern hemisphere extratropics (20–50S; Figure 5.9c, f). Note that the TMPA only covers from 50S to 50N so the statistics is done within this extent. Overall, the same effect of the

Gaussian transformation of precipitation is also generally seen. The value-dependent biases are removed in all regions. Using the logarithm transformation, the climatological distributions are skewed toward large precipitation amounts in the land and tropical regions where the convective precipitation is more prevalent, and toward small precipitation amounts in other regions. The skewness is less obvious in all regions when the Gaussian transformation is applied. As to the correlation, the increase of the correlation is particularly notable in the land region and in the northern hemisphere extratropics.

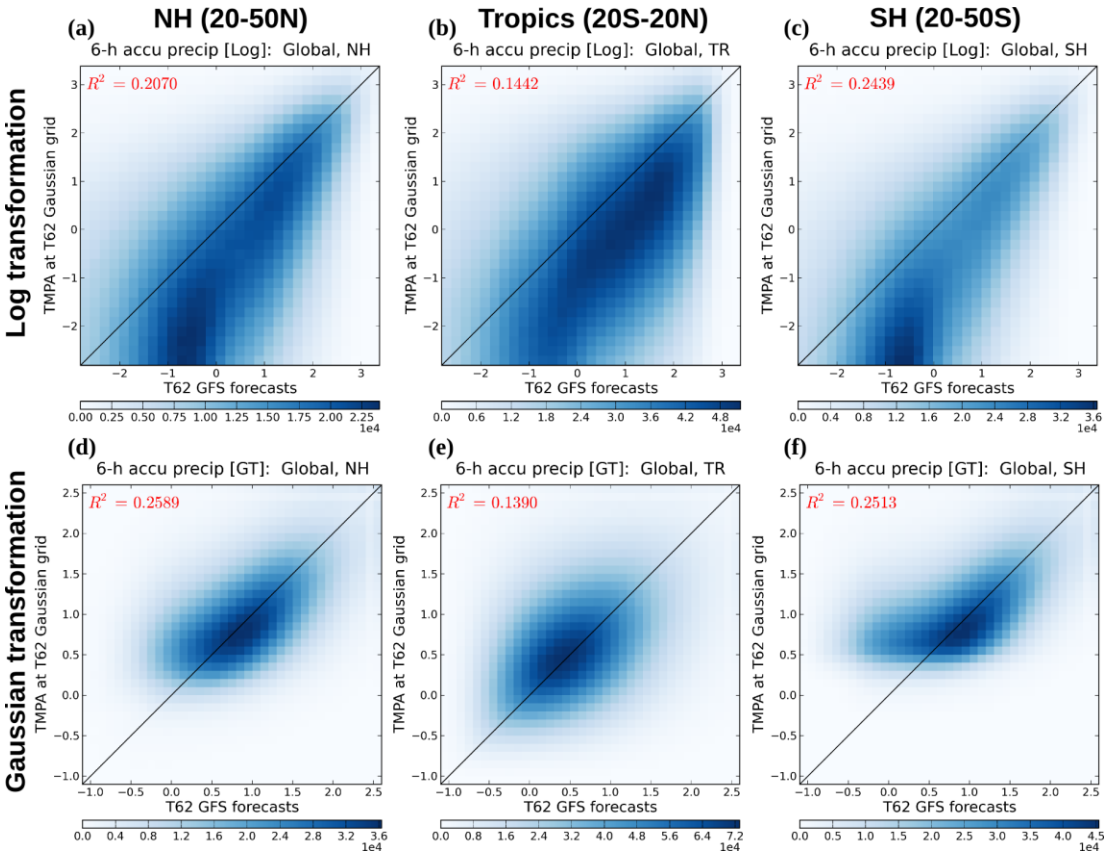

Figure 5.9: As in Figure 5.8, but for (a) (d) the northern hemisphere extratropics (20–50N), (b) (e) the tropical regions (20N–20S), and (c) (f) the southern hemisphere extratropics (20–50S).

5.4 Gaussianity statistics

Another statistics examining the Gaussianity in the model background is also computed here. In Chapter 2.3, we mentioned that the Gaussian transformation based on the climatological CDFs does not necessarily ensure the Gaussianity of the background error distributions. However, we assumed that it is still helpful to make the error distributions more Gaussian. This assumption can be persuasively verified using samples of ensemble model backgrounds since we can explicitly compute the Gaussianity given an ensemble. To generate the samples of this statistics, we need to run ensemble GFS forecasts. Following the design shown in Figure 5.10, we conduct a series of 9-hour ensemble GFS forecasts at the T62 resolution initialized from the ensemble analyses of a GFS-LETKF cycling run, and then the 3 to 9 hour forecasts are taken to form a series of ensemble model background. The 6-hour accumulated precipitation amounts are computed following the same method described in Chapter 5.2. The GFS-LETKF cycling run assimilates only the global rawinsonde data and is taken from an experiment that will be introduced in Chapter 6. It is noted that instead of computing the statistics for the 10-year data every 6-hour cycle, we only compute this Gaussianity statistics for the year 2008 and every 30 hours (5 data assimilation cycles) due to the heavy computational burden of running the ensemble model. The use of 30 hours instead of a multiple of a day is to avoid always computing the statistics in the same time of the diurnal cycle.

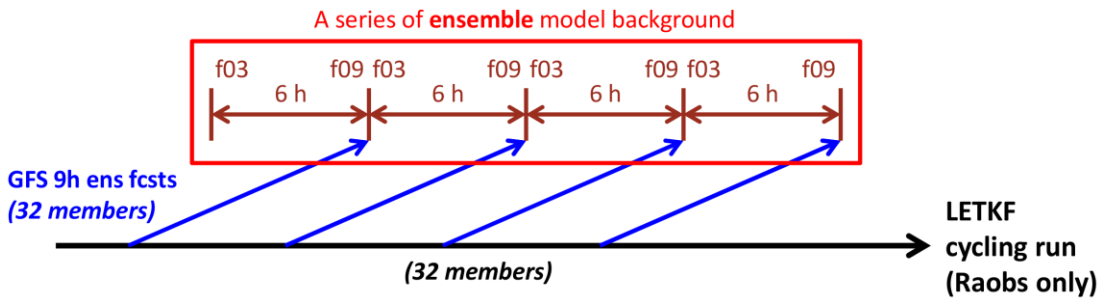

Figure 5.10: Formation of samples of ensemble precipitation in the GFS model backgrounds. Note that in our study, cycles in between every 5 cycles are skipped in order to save computational time.

The "Gaussianity" can be defined by several measures, such as the sophisticated "relative entropy" method, simpler methods based on hypothesis testing, or the even simpler skewness and kurtosis (Bocquet et al. 2010). Here we use the method based on the hypothesis testing to measure the deviation from the Gaussian distribution for a given distribution:

$$\chi^2 = \sum_{k=1}^{K} \frac{\left(\tilde{y}^{(k)} - \tilde{y}^{(k)}_{\text{expected}}\right)^2}{\sigma^2}, \tag{5.4}$$

where K is the ensemble size, $\tilde{y}^{(k)}$ is the (transformed) observation value in the kth member that has been sorted in ascending order, and

$$\tilde{y}^{(k)}_{\text{expected}} = \bar{y} + \sigma F^{G^{-1}}\left(\frac{k - 0.5}{K}\right), \tag{5.5}$$

representing a realization of the expected Gaussian distribution. The expected mean $\bar{y}$ and the expected variance σ^2 are determined from the background members $\tilde{y}^{(k)}$. The χ^2 value is a measure of the deviation from the expected Gaussian distribution, so it is a measure of the "non-Gaussianity." A larger χ^2 value means a more non-Gaussian

background error distribution, and vice versa. After computing the χ^2 value for each precipitation observation at each cycle, they can be averaged in time or in any group to obtain meaningful statistics.

Figure 5.11 shows the average χ^2 values with respect to the number of background members with positive precipitation not using (NT) and using each transformation method. The transformation methods here include with the logarithm transformation with $\alpha = 0.6$ mm (Log), and the Gaussian transformation with the CZ (GTcz) and BZ (GTbz) methods for zero precipitation transformations. The Gaussianity increases (χ^2 decreases) with the number of precipitating members, regardless of the transformation methods. Therefore, the current Gaussianity statistics provides a compelling reason of implementing the model background-based quality control criterion as proposed in the SPEEDY model experiment (Section 3.3.2). Compared the χ^2 values computed with transformed precipitation to those computed with the original precipitation, it is found that the Gaussianity is considerably increased when there are more than 8–10 precipitating members and any of the three transformation methods is used (Figure 5.11c, f, g), while the transformation can also make the error distribution more non-Gaussian when there are too few the precipitating members. Although the transformation methods seem to be deteriorating in the latter case, we do not worry about it because the quality control criterion monitoring the number of precipitating members will prevent the observations being assimilated in this situation. Comparing the different transformation methods, the Gaussian transformations are generally more effective than the logarithm transformation, and the GTbz method results in the most Gaussian background errors

of precipitation, leading to as much as 60% improvement than using the original precipitation values when there are more than 24 precipitating members (Figure 5.11g). The simpler GTcz method shows the similar effect as GTbz, but suffers a little when there are many but not all precipitating members (Figure 5.11f).

Figure 5.12 shows the global maps of the χ^2 values averaged in time. As discussed before, the general improvements by transforming the precipitation are also seen here. As to the geographical distributions, the very non-Gaussian regions are distributed over the desert areas. All three transformation methods cannot improve the Gaussianity over these really bad regions. Therefore, it would not be a good idea to conduct the precipitation assimilation over the areas with very infrequent precipitation. Another key finding is that the Gaussianity over the ocean is generally better than over the land, and most of the improvements are also achieved over the ocean.

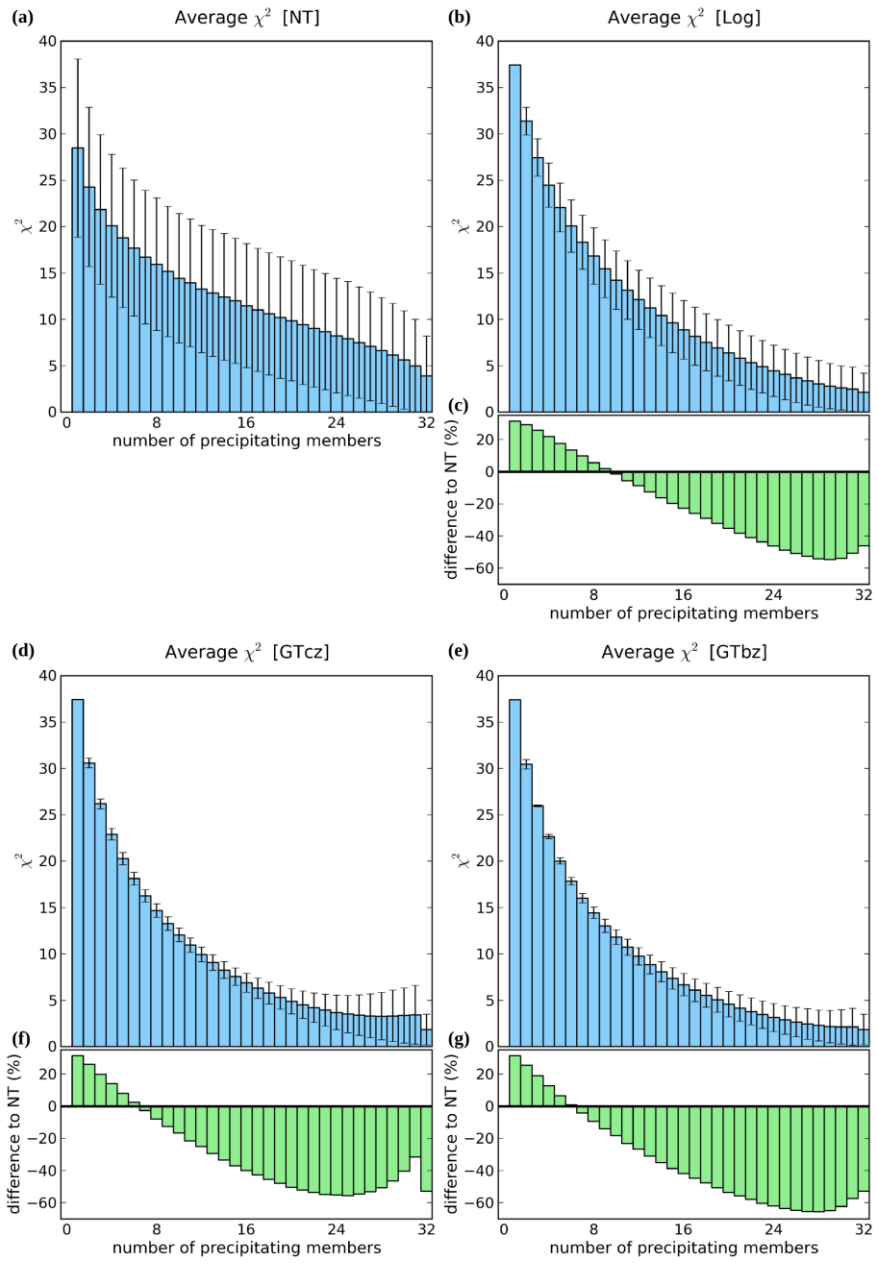

Figure 5.11: The average non-Gaussianity (χ^2) of background precipitation errors with respect to the number of precipitating background members (a) without transformation, (b) with the logarithm transformation, (d) with the Gaussian transformation and the CZ method for transforming zero values, and (e) with the Gaussian transformation and the BZ method for transforming zero values. (c) (f) (g) The percentage differences of the average χ^2 in each method as compared to those without transformation.

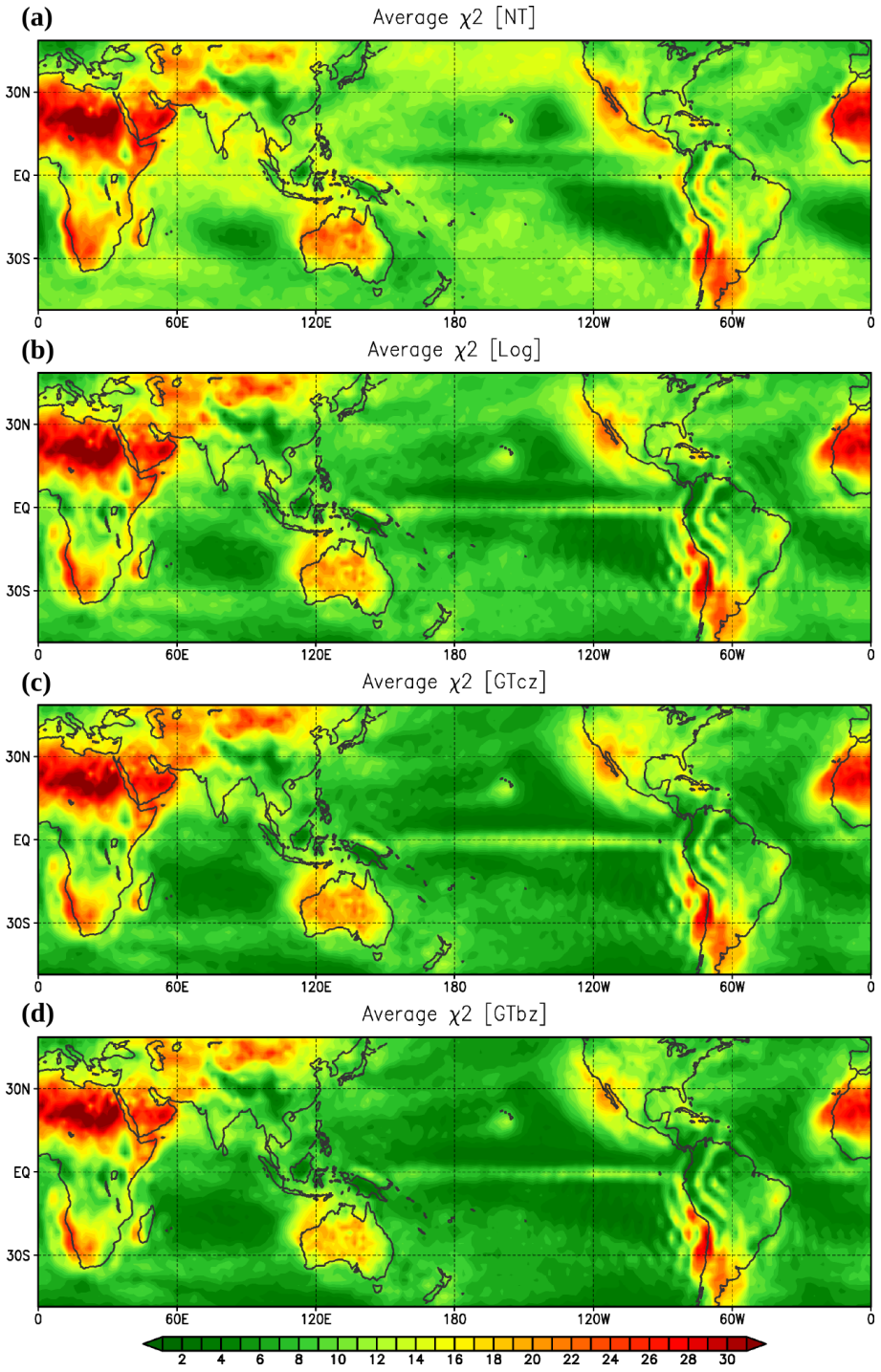

Figure 5.12: The maps of the average non-Gaussianity (χ^2) of background precipitation errors (a) without transformation, (b) with the logarithm transformation, (c) with the Gaussian transformation and the CZ method for transforming zero values, and (d) with the Gaussian transformation and the BZ method for transforming zero values.

5.5 Summary and discussion

In this chapter, we compute several statistics with the precipitation variable in the model background and observations from the point of view of the LETKF data assimilation. To achieve most meaningful statistics, the samples are carefully constructed using the same model with same forecast time, the same data assimilation system (to form the ensemble), the same observations, and the same resolution, as we planned in the real precipitation assimilation experiments. These statistical results can give us many useful hints of how to extract much useful information from the precipitation observations.

First of all, as we expected, the errors of precipitation in both numerical models and observations are large. This fact can contribute to a substantial amount of difficulties in the precipitation assimilation. For example, the GFS model has a severe problem in parameterizing the marine stratocumulus precipitation at a T62 resolution. Strenuous efforts to improve the accuracy of the model precipitation or satellite precipitation estimates have been made by the modeling or retrieval communities, but they are still very difficult topics. In our data assimilation study goals, we do not include any modification of the model or the observations. Instead, we adopt two strategies: For the "useful" component of the observation data, we apply appropriate transformations, and remove the value-dependent biases to make the model and observed precipitation have similar climatological distributions; for the other "difficult-to-use" component, we define effective quality control criteria to reject them. That an observation is difficult is not necessarily because the observation itself is poor, but could also be because the model backgrounds are poor, something that

can be diagnosed from the statistics in this chapter. We expect that by taking this approach, although both the model and observations may have large errors, the improvement of the model forecasts, which is our main goal, could still be achieved.

The "precipitation scale" is a key point of the problem. It can be understood in many aspects. First, the principle to simulate precipitation in numerical models can be intrinsically different at different grid resolutions. When the grid resolution is low, the precipitation is mainly parameterized by cumulus schemes; when the resolution is sufficient to resolve convection, the microphysics parameterization schemes can take over. Not only can the error characteristics be very different between these two methods, but even with the same scheme, it can also change with the model resolution. For example, in the GFS model, precipitation at the T126 resolution is less biased than that at the T62 resolution, but the correlation to the observations is also lower. Besides, the precipitation is usually patched randomly, especially for convective precipitation, leading to large random errors at high resolutions. The timing of the convective precipitation is also difficult to simulate by the model. In addition, the high spatial and temporal variabilities further lead to large representativeness errors, which are also dependent upon resolutions and important to the data assimilation. Performing spatial and/or temporal averages can effectively reduce the errors. Huffman et al. (2010) recommended TMPA users create time/space averages that are appropriate to their application from the original fine-scale data. Bauer et al. (2011) also mentioned that using the spatially/temporally smoothed precipitation data in the assimilation can be beneficial. Based on similar reasons, accumulated precipitation (equivalent to a time average) is a better variable to be assimilated rather than the

instantaneous precipitation rate for precipitation assimilation. However, this strategy seems to contradict the continued pursuit of higher resolution, especially if we are able to afford the high-solution models and take the high-resolution observations. There is a "trade-off" between resolution and errors. If the main goal is to improve the longer-term model forecasts, using the smoothed lower resolution fields to improve the large-scale analysis can be a reasonable choice. In our study, we can run the GFS model at a T62 low resolution, so the TMPA data are upscaled to the same T62 grids before assimilated, therefore focusing on the assimilation of large-scale precipitation. An interesting test would be to use a higher resolution model but still include an average operator in the observation operator H, in order to see if the sacrifice of the resolution can still help to improve the effectiveness of the precipitation assimilation. We note that the strategy for effective assimilation of convective scale precipitation such as meteorological radar observations could be quite different from what we used in our study.

The statistics we developed also answer that the Gaussian transformation can improve the precipitation assimilation. Compared to the original precipitation variable, the Gaussian transformation can reduce the non-Gaussianity measured by χ^2 by as much as 60% when there are enough background precipitating members. The logarithm transformation has similar effects but it is less effective. The BZ method to transform zero precipitation leads to better results than the CZ method. In addition, applying the Gaussian transformation to the model background precipitation and precipitation observations separately can also serve as a CDF-based bias correction

that can correct the value-dependent bias and increase the correlation between the model precipitation and observations over some regions.

Based on the above discussion, the problems associated with the assimilation of real precipitation in realistic models will be addressed as follows:

- Large non-Gaussianity of the precipitation variable: Use the Gaussian transformation and assimilate precipitation only where there are enough background members with positive precipitation. This was proposed for the SPEEDY model experiments and has been verified in this chapter.
- Inconsistent probability distribution of precipitation between model and observation climatology: Define the CDF-based transformation for the model variable and the observation precipitation separately to remove the amplitude-dependent bias.
- Timing errors of the precipitation: Use the 6-h accumulated amount.
- Deficient precipitation parameterization: Do not use observations when the model is deficient. Appropriate quality control criteria need to be defined in order to only select the precipitation observations where the model can use them effectively. In the next chapter, we will introduce a simple criterion based on the correlation of model background precipitation and the precipitation observations in each grid point.
- High-resolution observations contain large random errors: Perform spatial and/or temporal averages to reduce the random errors; upscale the observations to large-scale grids.

- Unknown observation error scales and distributions: This issue is not investigated in this study. Instead, we obtain by tuning the best observation error assumed to be globally constant in the transformed variable.

Chapter 6: Assimilation of real precipitation observations II - Experimental results

6.1 Introduction

In this Part II chapter of the real precipitation assimilation, we show the results of precipitation assimilation experiments using more realistic models and observations. The basic experimental design is similar to the SPEEDY model experiments in Chapter 3, but with the NCEP GFS model assimilating TMPA satellite precipitation data, so that it is no longer an OSSE. Real model and observation errors are in play here. We still use a rawinsonde-only experiment as the baseline and assimilate precipitation on top of it in order to have a large "room for improvement." More focus on the comparison among the precipitation transformation methods is put here because the results with the real model and data can provide more reliable guidance on the effects of precipitation transformations.

6.2 Experiment design

6.2.1 General settings

The GFS model is run at a T62 resolution with 64 vertical hybrid sigma/pressure levels. Thirty-two ensemble members are used. The initial ensemble at 00Z November 1, 2007 is created by taking a random series of operational GFS analyses at unrelated times. All conventional (non-radiance) observations taken from the NCEP PREPBUFR dataset are assimilated in the first month in order to spin up the system and evolve the ensemble to represent the "error of the day." After this one-

month cycling run, the analyses on 00Z December 1, 2007 is used as the initial condition for all experiments. The experimental settings are summarized in Table 6.1. In the "RAOBS" experiment, only the rawinsonde observations are assimilated. In the other experiments, the global TMPA data upscaled to the T62 Gaussian grids and computed in a form of the "6-hour accumulated precipitation" during the assimilation window are assimilated as well. In the "NT" experiment, no transformation of precipitation is used, and in the "Log", "GTcz", and "GTbz" experiments, the logarithm transformation, the Gaussian transformation with the CZ method to transform zero precipitation based on climatology, and the Gaussian transformation with the BZ method to transform zero precipitation based on the background ensemble are used, respectively. The method of the Gaussian transformation applied to the real GFS model precipitation and the TMPA data has been described in Chapter 5.3. The constant α in the logarithm transformation [refer to Equation (2.1)] is set to 0.6 mm (equivalent to 0.1 mm h^{-1} average precipitation rate), which is an optimal value based on several trials. When no transformation is used, the observation error of precipitation is set to 50% of the observed values but with a minimum of 0.3 mm (equivalent to 0.05 mm h^{-1} average precipitation rate). When the logarithm transformation or the Gaussian transformation is used, it is set to a constant of 0.5 (unitless) in the transformed variable except for the sensitivity experiments. All of these choices are made to optimize the experimental results in each experiment. The horizontal localization length scale ("R" localization in Greybush et al. 2011) of the precipitation observations is 350 km in most of experiments, but it is 500 km for all other observations. These localization settings are based on the finding in the

SPEEDY model experiments that the optimal localization scale of precipitation observations would be smaller than regular observations (Section 3.5.3). The vertical localization length scale is 0.4 in natural logarithm of pressure for regular observations and precipitation observations, while the centers of the localization functions of all precipitation observations are located at 850 hPa. The inflation scheme is the mixed adaptive inflation-relaxation scheme described in Section 4.3.5.

The five main experiments (RAOBS, NT, Log, GTcz, and GTbz) are conducted for a 13-month cycling run until 00Z January 1, 2009 and 5-day free forecasts initialized from each 6-hourly ensemble mean analysis are conducted in order to quantify the forecast impacts of the assimilation of precipitation. In addition, other five sensitivity experiments are conducted in the same way to examine the sensitivities to the precipitation observation errors (GTbz_err0.3, GTbz_err0.7), the localization lengths (GTbz_loc500, GTbz_loc200), and the precipitation quality control criteria (GTbz_16mR). These sensitivity experiments are only conducted for 3 month ended at 00Z March 1, 2008. The details of these sensitivity experiments will be described in Chapter 6.4. The European Centre for Medium-range Weather Forecasts (ECMWF) ERA interim reanalysis dataset is used to verify our results. It is noted that the one-month period from December 1, 2007 to January 1, 2008 is still regarded as an additional spin-up period because a certain period is required for the adaptive inflation scheme to adjust to the change of observing systems from the previous conventional observation dataset to the new configurations in each experiment. The other details of the GFS-LETKF data assimilation system can be found in Chapter 4.

Table 6.1: Design of all experiments.

Experiment	Observation		Transf	QC for precip assimilation	Obs error of precip	Loc length of precip
	Raobs	Precip				
RAOBS	X					
NT	X	X		Precip members ≥ 24	50%, minimum 0.3	350 km
Log	X	X	Log, $\alpha = 0.6$	Precip members ≥ 24	0.5	350 km
GTcz	X	X	GTcz	Precip members ≥ 24	0.5	350 km
GTbz	X	X	GTbz	Precip members ≥ 24	0.5	350 km
GTbz_err0.3	X	X	GTbz	Precip members ≥ 24	0.3	350 km
GTbz_err0.7	X	X	GTbz	Precip members ≥ 24	0.7	350 km
GTbz_loc500	X	X	GTbz	Precip members ≥ 24	0.5	500 km
GTbc_loc200	X	X	GTbz	Precip members ≥ 24	0.5	200 km
GTbz_16mR	X	X	GTbz	Precip members ≥ 16	0.5	350 km

6.2.2 Quality control criteria for the TMPA assimilation

As introduced in Section 3.3.2, the precipitation observations are assimilated only when the number of the background members with positive precipitation is greater than a threshold. This model background-based criterion can ensure the quality of the precipitation assimilation as experimentally examined in Section 3.5.1 and theoretically discussed in Chapter 5.4. Here with the GFS model, we require at least 24 (out of 32) precipitating background members to assimilate the precipitation ("24mR" hereafter).

In addition to the 24mR criterion, and in response to the discussion in Chapter 5 that the model and the observations can be very inconsistent over certain regions, a

new quality control criterion based on the correlation of long-term model precipitation and long-term observed precipitation is introduced. Based on the same 10-year samples of the GFS model backgrounds and the TMPA data as we used to compute the CDFs and several statistics, the correlation between these two datasets are computed for each grid point and each 10-day period of year (refer to Chapter 5.3). In every period, data within ± 2 periods (± 20 days) are considered together in order to obtain the temporally smoothed field. This correlation score is a simple measure of the statistical "consistency" between the model background and the observations. We expect that the precipitation data distributed over the higher-correlation regions are more useful than those over lower-correlation regions where the model errors and/or observation errors are too large. Figure 6.1 shows the correlation maps in 4 different periods in January, April, July, and October. We choose the correlation ≥ 0.35 as the criterion for the precipitation assimilation ("Corr0.35" hereafter), which corresponds to the green shaded area in the figure (the blue contours are correlations $= 0.35$). Overall, the correlation over the ocean is generally much higher than that over the land. The marine stratocumulus regions are problematic as we observed in Chapter 5.3, and the entire Africa and the Tibetan Plateau also show constantly low correlation; therefore, the precipitation observations over these regions are rejected. Over the United States, the eastern U.S. has higher correlation than the western U.S., and the precipitation observations over the western U.S. are rejected in winter and in summer. We note that this correlation score is not the only possible method to define the precipitation quality control. In Chapter 7.5, we will discuss and compare several other potential methods.

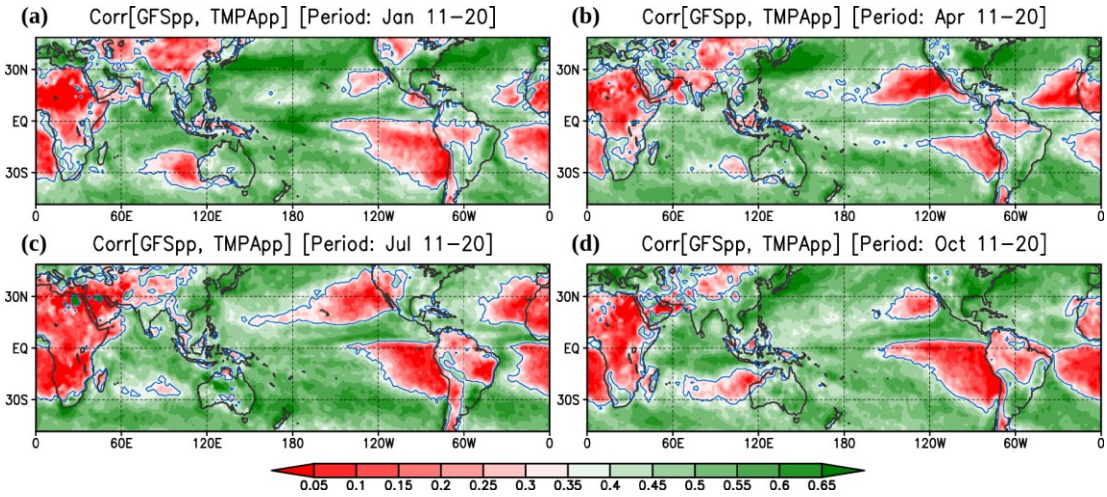

Figure 6.1: The maps of correlation between precipitation in the GFS model backgrounds and in the TMPA observations during the periods of (a) January 11–20, (b) April 11–20, (c) July 11–20, and (d) October 11–20. The blue contours indicate correlations = 0.35 that is the threshold of the precipitation assimilation. Precipitation observations are assimilated over the green shaded areas.

6.3 Results

6.3.1 Global analysis and forecast errors

Figure 6.2 shows the evolution of the global RMS analysis errors of the u-wind verified against the ECMWF ERA interim reanalysis over the 13-month period. Although the time variation is large, it can be seen that the precipitation assimilation experiment without transformation (NT; cyan lines) is clearly worse than RAOBS (black lines), the experiment with logarithm transformation of precipitation (green lines) is roughly comparable to RAOBS, and the two experiments using Gaussian transformation of precipitation (GTcz and GTbz; blue and red lines) are slightly better

than RAOBS. The yellow shade indicates the verification period of the entire year 2008 that will be used to compute the average errors and biases in later figures.

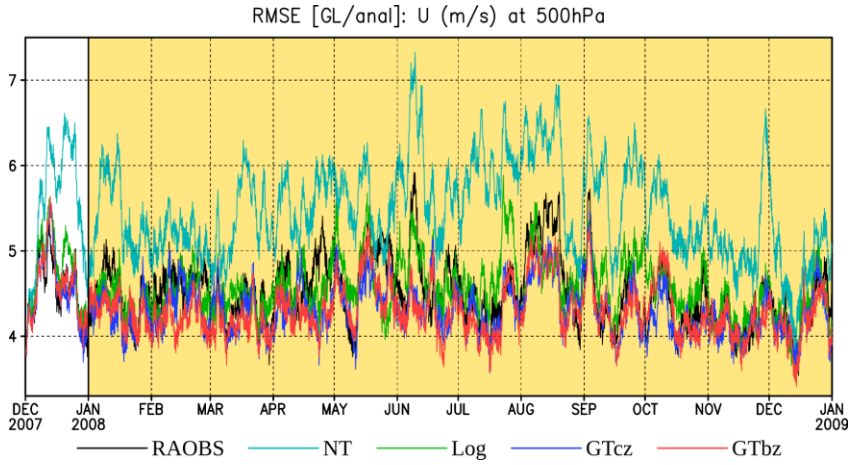

Figure 6.2: The 13-month evolution of the global root-mean-square analysis errors of u-wind (m s^{-1}) verified against the ERA interim reanalysis in RAOBS, NT, Log, GTcz, and GTbz. The yellow shaded period from January 1, 2008 to January 1, 2009 is the verification period.

Figure 6.3 shows the average 5-day global RMS forecast errors (solid lines) and biases (dashed lines) in the 1-year verification period versus forecast time. The positive impacts by precipitation assimilation using the Gaussian transformation are clearly seen in this figure. With the Gaussian transformation (blue lines and red lines, which are almost superposed), the GFS model analyses ($t = 0$) and forecasts are constantly improved in the 5 day range in terms of the 500-hPa u-wind (Figure 6.3a), the 500-hPa temperature (Figure 6.3b), and the 700-hPa specific humidity (Figure 6.3c). The differences in the analysis and forecast errors between the GTcz or GTbz experiments to the Raobs experiments are statistically significant at all 0- to 120-hour

forecast times at the 0.1% level using the hypothesis testing for paired samples. For the mid-level wind and temperature, the CZ method (blue lines) and the BZ method (red lines) of the zero precipitation transformation lead to almost indistinguishable results (for the 500-hPa u-winds, they are statistically insignificant at 18- to 120-hour forecast times at the 1% level; for the 500-hPa temperature, they are statistically insignificant at 60- to 120-hour forecast times at the 1% level.), but for the 700-hPa moisture, the more sophisticated BZ method performs slight better (statistically significant at all 0- to 120-hour forecast times at the 0.1% level). The improvement lasts over the 5-day forecast period, indicating that the master dynamical variables (e.g., potential vorticity) are improved by the precipitation assimilation using the LETKF, which is consistent with our SPEEDY OSSEs but different from the past experience that the model tends to quickly forget the changes by assimilating precipitation (e.g., Mesinger et al. 2006). On the other hand, with the logarithm transformation (green lines), the impacts are marginal. The Log experiment shows similar forecast errors in the 500-hPa u-wind, and slightly worse 500-hPa temperature but slightly better 700-hPa moisture as compared to RAOBS. In great contrast, if the transformation of precipitation is not used (NT; cyan lines), very large negative impacts by precipitation assimilation are seen with all variables. The negative impacts in Log and NT experiments are also seen in the biases: the precipitation assimilation by these two methods tends to increase the model biases, especially in the temperature and moisture variables.

It is important to note that the Corr0.35 quality control criterion based on the correlation between the model background and the observations is rather essential in

these real precipitation assimilation experiments. When this criterion is not used, even with the Gaussian transformation, the impact by assimilating the TMPA data is still negative (not shown), which means that the observations over the low correlation regions are too harmful so that all positive impacts by those useful precipitation observations are completely eroded away.

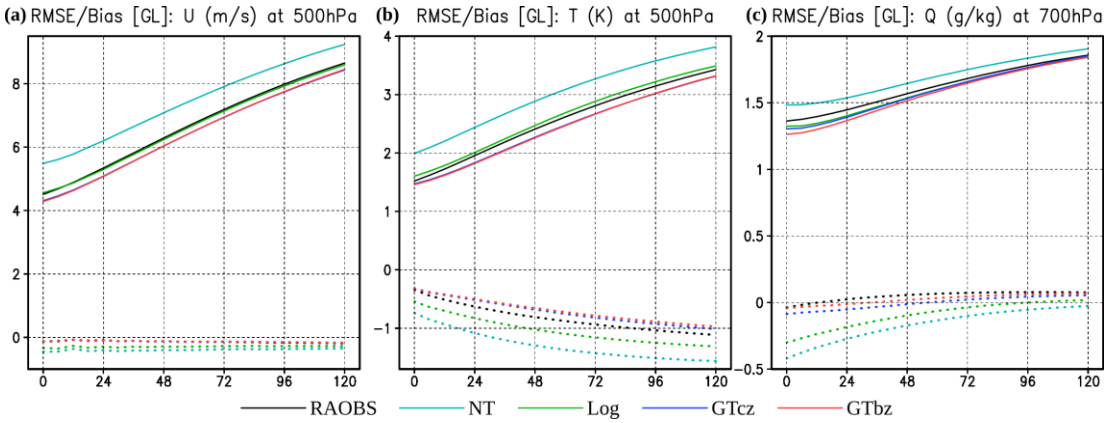

Figure 6.3: The average global root-mean-square forecast errors (solid lines) and biases (dashed lines) in year 2008 (verified against the ERA interim reanalysis) versus forecast time in RAOBS (black lines), NT (cyan lines), Log (green lines), GTcz (blue lines), and GTbz (red lines): (a) 500-hPa u-wind (m s^{-1}) (b) 500-hPa temperature (K) (c) 700-hPa specific humidity (g kg^{-1}).

6.3.2 Regional dependence

The regional dependence is investigated by computing the RMS errors and biases for three separate regions: the Northern Hemisphere extratropics (20–90N; NH), the tropics (20S–20N; TR), and the Southern Hemisphere extratropics (20–90S; SH). Figure 6.4, 6.5, and 6.6 shows the average RMS errors and biases of the 500-hPa u-

wind, the 500-hPa temperature, and the 700-hPa specific humidity in the 5-day forecasts for the NH, SH, and TR regions, respectively. As discussed in the SPEEDY model experiments, the analyses and forecasts over the NH region are more accurate than the SH region because of its better observing network, and the NH and SH regions have larger error growth rates than the TR region due to the stronger growth rates of mid-latitude baroclinic instabilities. With the Gaussian transformation, the improvement by precipitation assimilation is seen over all three regions. In particular, the SH region is improved the most, resulting in about additional 12 hour forecast lead time in u-wind (Figure 6.5a). The above results in separate verification regions are consistent to what we found with the SPEEDY model experiments. Among the three variables, the 700-hPa moisture is the one most benefitted by the precipitation assimilation. For the moisture variable, the difference in analysis errors $(t = 0)$ between RAOBS and GTcz/GTbz are large, especially in the SH region (Figure 6.5c), although the difference becomes smaller with forecast time. The GTcz and the GTbz are still almost indistinguishable in most regions and variables, except for the u-wind in the TR region, and the moisture in the NH region and TR region, where the GTbz method shows slightly better results than the GTcz method.

In terms of the mid-level wind and temperature, the Log experiment leads to marginal results as RAOBS in the NH and SH region, but it clearly degrades the temperature in the TR region. In terms of the 700-hPa moisture, the Log experiment can, however, brings positive impacts, showing again the particular benefit of precipitation assimilation on the moisture. By contrast, the NT experiment results are bad in all regions for all variables.

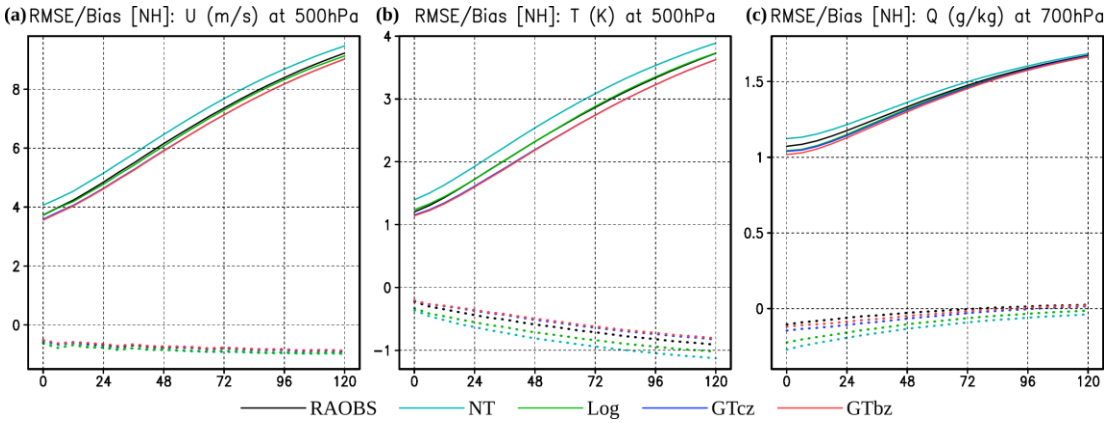

Figure 6.4: As in Figure 6.3, but for the northern hemisphere extratropical region (20–90N).

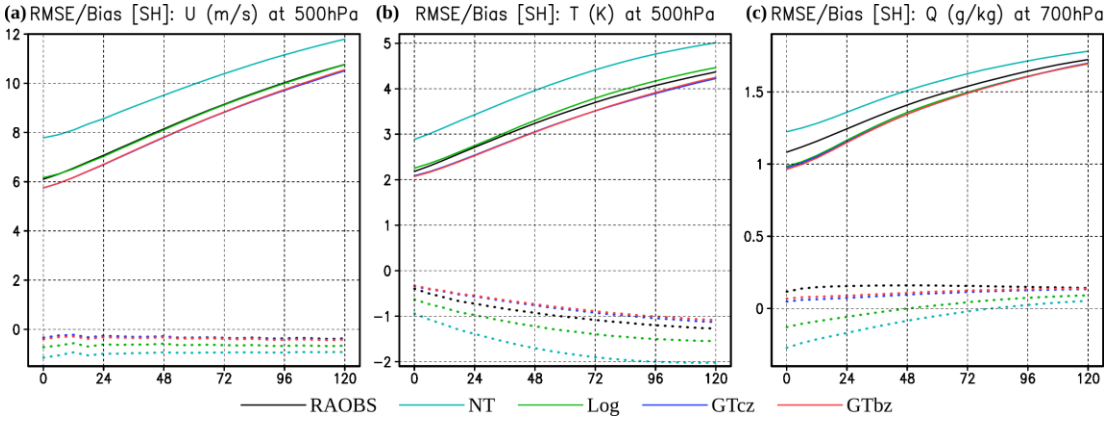

Figure 6.5: As in Figure 6.3, but for the southern hemisphere extratropical region (20–90S).

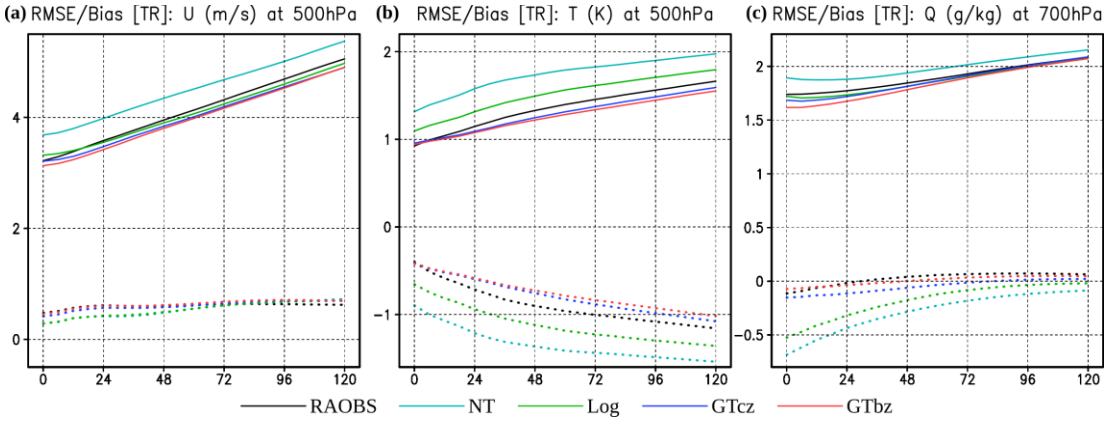

Figure 6.6: As in Figure 6.3, but for the tropical region (20N–20S).

6.3.3 Vertical error profiles

The vertical profiles of the 24-hour forecast errors are plotted in Figure 6.7 and 6.8. Figure 6.7 shows the vertical profiles of the u-wind errors. The error is the largest at 200–300 hPa where the jet level with large zonal winds is located. The improvement or degradation of the 24-hour forecasts by assimilating the TMPA data in GTcz, GTbz, Log, and NT experiments are consistently seen at all levels, while the largest improvement with the Gaussian transformation of precipitation is found at the mid-levels. Besides, the TR region has different profiles of the precipitation assimilation impacts compared to the other regions. The low-level (700–1000 hPa) u-wind is not improved by the precipitation assimilation. Figure 6.8 shows the vertical profiles of the specific humidity errors. Generally, with the Gaussian transformation (GTcz and GTbz), the moisture is improved the most at the mid-levels (500–700 hPa), which is already shown in Figure 6.3–6.6, but can be degraded at the lower levels (850–1000 hPa), especially in the TR region. The GTbz method is slightly better than the GTcz method when the moisture is verified, and again, the Log results are marginal and the NT results are very bad.

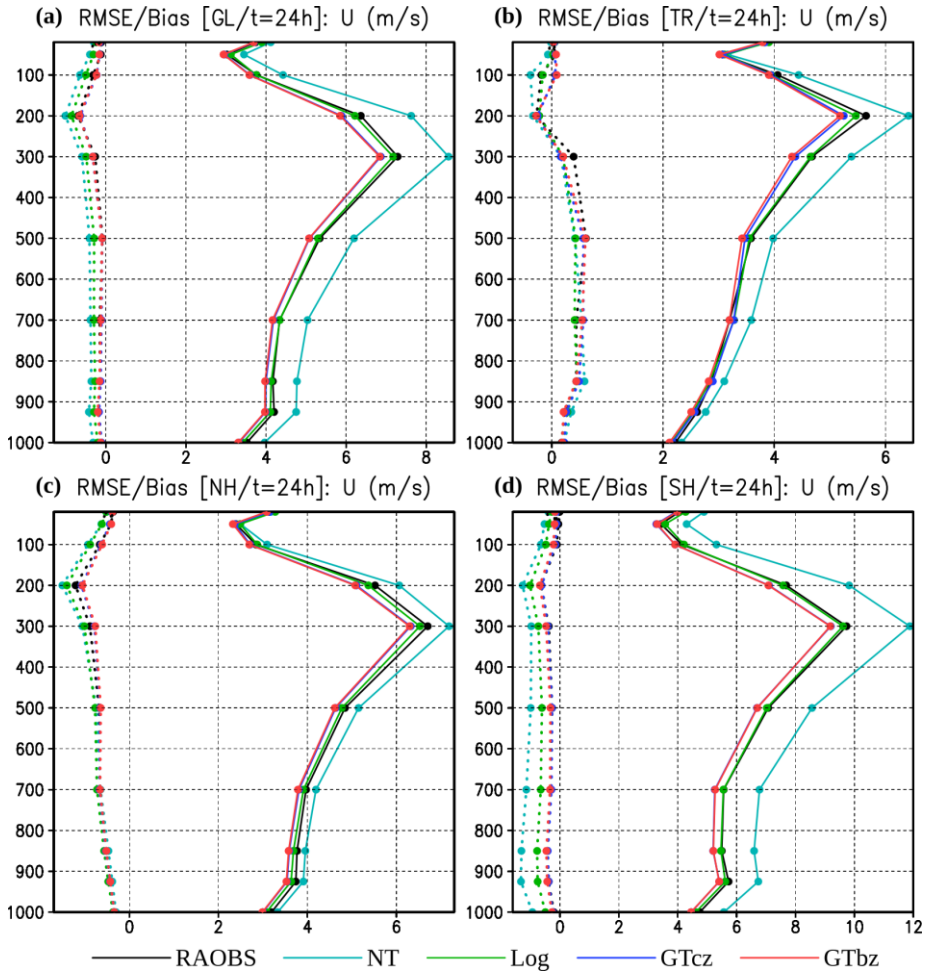

Figure 6.7: The vertical profiles of the average root-mean-square 24-hour forecast errors (solid lines) and biases (dashed lines) of u-wind (m s^{-1}) in year 2008 (verified against the ERA interim reanalysis) in RAOBS, NT, Log, GTcz, and GTbz. The verification regions are (a) the globe, (b) the northern hemisphere extratropics (20–90N), (c) the tropics (20N–20S), and (d) the southern hemisphere extratropics (20–90S).

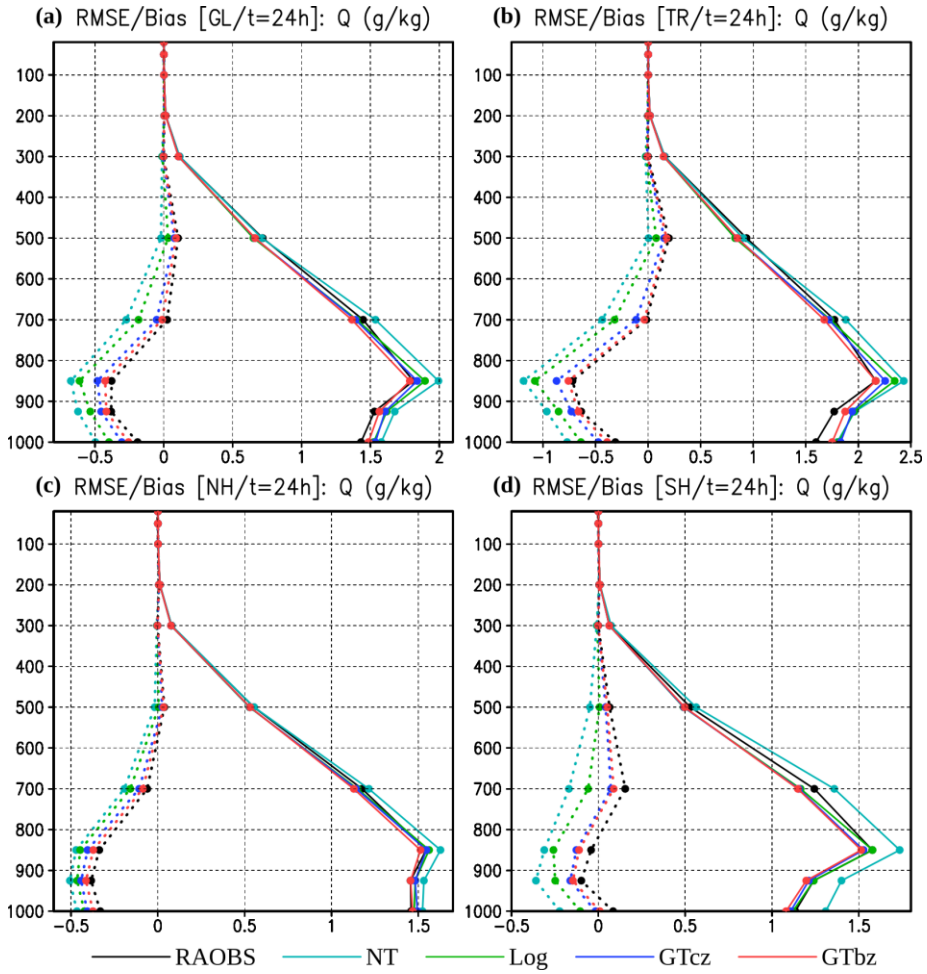

Figure 6.8: As in Figure 6.7, but for the verification of specific humidity (g kg^{-1}).

6.4 Sensitivity experiments

Five additional sensitivity experiments are conducted in order to examine the sensitivities to the precipitation observation errors, the localization lengths, and the precipitation quality control criteria. Due to the computational burden, these sensitivity experiments are only conducted for 3 month ended at 00Z March 1, 2008 so that the average period for the forecast verification is only 2 months. The experimental settings of these experiments are also listed in Table 6.1. They are all

designed based on the GTbz experiment. In the experiments GTbz_err0.3 and GTbz_err0.7, the observation errors for precipitation are changed to 0.3 and 0.7, respectively, instead of 0.5 in GTbz. In the experiments GTbz_loc500, GTbz_loc200, the localization length scales for precipitation observations are changed to 500 km and 200 km, respectively, instead of 350 km in GTbz. In the experiment GTbz_16mR, it requires at least 16 (out of 32) members having positive precipitation (16mR criterion) instead of 24 members in GTbz.

6.4.1 Sensitivity to observation errors

Figure 6.9 shows the sensitivity of the 5-day forecast errors to the precipitation observation errors. Recall that in this study we use constant unitless values for the observation errors of precipitation when the Gaussian transformation is applied. Among the three values, 0.3, 0.5, and 0.7, the observation error of 0.5 as in the control experiment (red lines; GTbz) results in the best LETKF analyses and 5-day forecasts. When the values of 0.3 (blue lines) or 0.7 (green lines) are used, the precipitation assimilation still leads to improvements in the 5-day forecasts (compared to Raobs), but the improvements are smaller than that in GTbz when the value of 0.5 is used.

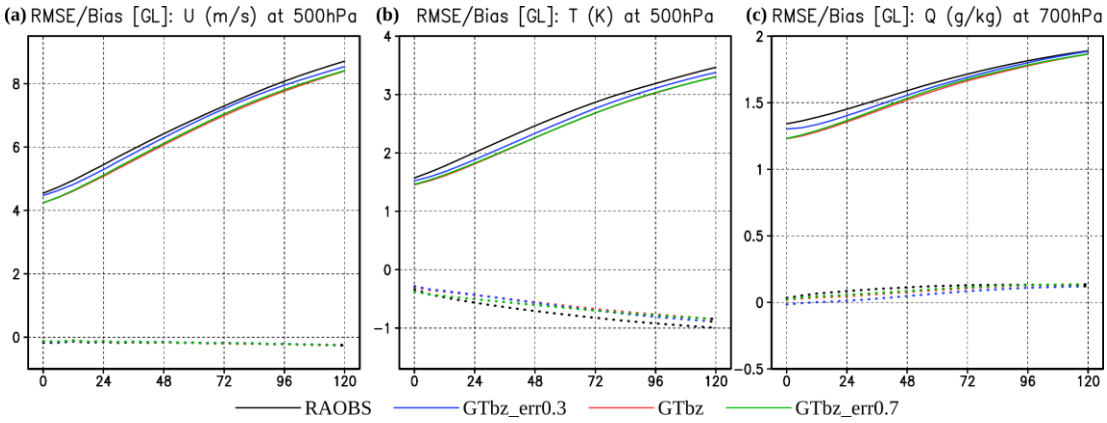

Figure 6.9: The average global root-mean-square forecast errors (solid lines) and biases (dashed lines) during January 1–March 1, 2008 (verified against the ERA interim reanalysis) versus forecast time in RAOBS (black lines), GTbz_err0.3 (blue lines), GTbz (err0.5; red lines), and GTbz_err0.7 (green lines): (a) 500-hPa u-wind (m s^{-1}) (b) 500-hPa temperature (K) (c) 700-hPa specific humidity (g kg^{-1}).

6.4.2 Sensitivity to localizations

Figure 6.10 shows the sensitivity of the 5-day forecast errors to the horizontal localization length scales for precipitation observations. It is verified that, compared to the localization length for conventional observations, smaller localization lengths are beneficial to the precipitation data assimilation, as we found in the SPEEDY experiments (Section 3.5.3). The horizontal localization lengths of 200 km (green lines) and 350 km (red lines) lead to similar results, which are all better than the 500 km localization lengths (blue lines). In our control experiment (GTbz), the 350 km localization length is used.

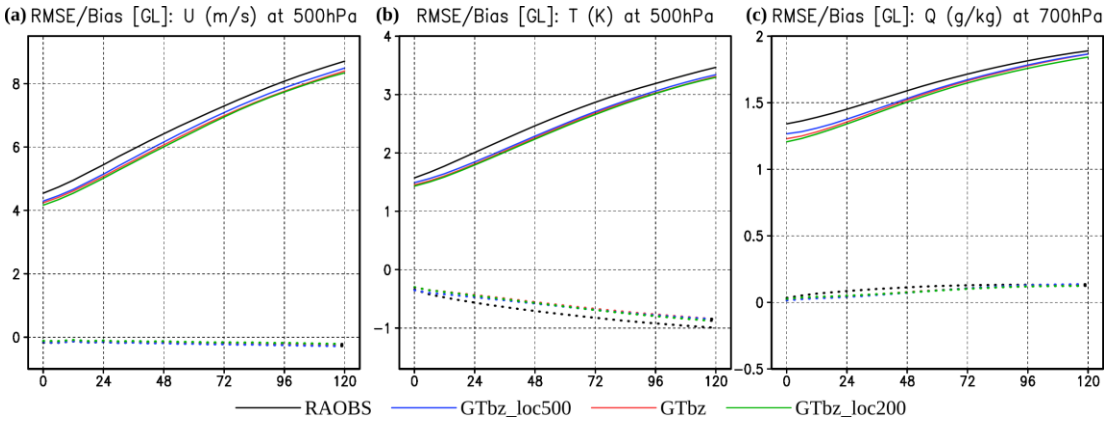

Figure 6.10: As in Figure 6.9, but for experiments RAOBS (black lines), GTbz_loc500 (blue lines), GTbz (loc350; red lines), and GTbz_loc200 (green lines).

6.4.3 Sensitivity to quality control criteria

Figure 6.11 shows the sensitivity of the 5-day forecast errors to the minimum numbers of the precipitating members in the background ensemble (i.e., XmR criteria). It is found that the 16mR and 24mR observation selection criteria lead to similar positive impacts by the precipitation assimilation. In particular, the stricter criterion, 24mR (red lines), results in slightly better analyses and 5-day forecasts than the 16mR criterion (blue lines), especially in mid-level u-winds and 700-hPa moisture fields.

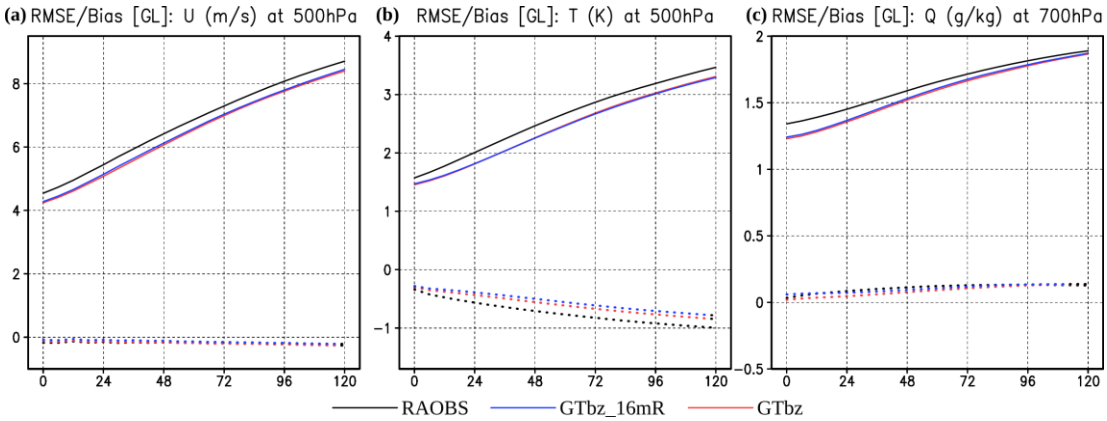

Figure 6.11: As in Figure 6.9, but for experiments RAOBS (black lines), GTbz_16mR (blue lines), and GTbz (24mR; red lines).

6.5 Summary and discussion

With the success of the LETKF assimilation of precipitation using the SPEEDY model, the same ideas are now tested with the realistic NCEP GFS model and the real TMPA observations. Compared to the SPEEDY model experiments, it is a more difficult problem because more issues emerge in these realistic settings, such as the possibly large model errors of precipitation, and the unknown observation errors. To solve the problem, we adopt all methods proposed with the SPEEDY perfect model experiments, and also introduce some additional modifications based on the guidance gained from the Part I statistical studies (Chapter 5). Consequently, using the rawinsonde-only experiment as the baseline of comparison, we successfully obtain positive results, which are comparable to the SPEEDY experiments, but using the realistic settings.

In additional to the quality control criterion based on the number of the precipitating background members (XmR criterion), a new criterion based on the

correlation between the long-term model background precipitation and the observation data in each grid point and each period of year is proposed in this chapter. The reason to implement this criterion is to filter out the precipitation observations made at the locations and seasons where the model background and the observation are climatologically inconsistent. The inconsistency can arise from the deficient precipitation parameterization in the model and/or the problematic precipitation retrievals. Assuming we are not planning to improve the model or the observations, this part of the observation data would be the part that should be discarded. In our experiments, we require the correlation be higher than 0.35 (Corr0.35 criterion), and it turns out to be an essential criterion to our experimental results since the experiment without this criterion was not successful.

Having the real model and observations, here we focus more on the comparisons among different transformation methods, including no transformation, logarithm transformation, and two Gaussian transformations with different methods of handling zero values. In contrast to the single transformation used in the SPEEDY model experiments, the Gaussian transformation here is applied to the model background and the observations separately. Among all experiments, only the experiments with the Gaussian transformation of precipitation show clear positive impacts by assimilating the TMPA data. The differences between the two schemes of zero precipitation transformations are fairly small, while the sophisticated GTbz method performs slightly better than the simple GTcz method in some variables such as moisture. The largest improvement is seen in the u-wind in the SH region. Additional 12-hour forecast lead time in u-wind is obtained there by assimilating the TMPA data,

meaning that the model "remembers" the assimilation change over the entire forecast periods. In contrast, the precipitation assimilation without using transformations (NT) leads to much degraded analyses and forecasts. The Log experiment is just marginal, resulting in slightly worse temperature fields but slightly better moisture fields.

Several sensitivity experiments are conducted, which conclude that the 0.5 observation error for the transformed precipitation, the 350 km horizontal localization length scale for precipitation observations, and the 24mR criterion, as used in the control experiment (GTbz), are close to their optimal values. The smaller horizontal localization lengths than that for conventional observations are beneficial to the precipitation data assimilation, which is consistent to our previous results in the idealized SPEEDY OSSEs.

It is important to note that the complexity of the current configuration is still "intermediate" between the OSSEs with simplified models and the real operational NWP. Firstly, although we double the resolution from T30 in the SPEEDY model to the T62 GFS model, the resolution is still low as compared to the state-of-the-art operational NWP models. Secondly, our baseline experiment, RAOBS, assimilates only rawinsonde observations, which is considered insufficient in operational forecasts. Although having the large room for improvement is advantageous for us to identify the positive impacts by the additional precipitation data, it does not prove that the precipitation assimilation will still be beneficial when more conventional and satellite observation data are assimilated as well. The average improvement by precipitation assimilation in the current GFS model experiments is relatively smaller than that in the SPEEDY model experiment, and we expect it becomes even smaller

when more observation data are also assimilated. Nevertheless, this work is undoubtedly another step forward towards the assimilation of global large-scale satellite precipitation estimates. Obtaining positive impacts by assimilating precipitation on top of a more accurate baseline experiment is one of our important future directions of work.

Chapter 7: Assimilation of real precipitation observations III - Forecast sensitivity to observations

7.1 Introduction

In Chapters 3 and 6, we demonstrated positive impacts by assimilating precipitation in an idealized system and a realistic system, respectively. The positive impacts were obtained by conducting many different experiments assimilating different sets of observations. In addition, we proposed to use the Gaussian transformation of precipitation and the quality control criterion that precipitation is assimilated only when enough precipitating members are present in the model background. The usefulness of these methods is also verified by conducting a group of sensitivity experiments. Conducting these so-called "observing system experiments" (OSEs) in order to recommend the best experimental settings is usually a very time-consuming process. In this chapter, we reexamine the effects of precipitation assimilation from a different aspect: we apply the method of the ensemble forecast sensitivity to observations (EFSO; Kalnay et al. 2012; Ota et al. 2013) to the precipitation assimilation with the GFS-LETKF system. The EFSO is a powerful technique which allows us to systematically estimate the impact on the short-range forecasts by *every* single observation in the same time, with only a small amount of additional computation. Therefore, by averaging the observation impacts in terms of various factors, such as geographic locations, numbers of precipitating background members, and the observed precipitation amounts, we can efficiently obtain an overall picture of the effectiveness or ineffectiveness of the precipitation assimilation,

without conducting many computationally expensive OSEs. By this route, the soundness of our methods of precipitation assimilation will be reinvestigated.

7.2 EFSO formulation

The method to compute the forecast sensitivity to observations (FSO) was first introduced by Langland and Baker (2004) using an adjoint method with a variational data assimilation system. It has been applied to several operational data assimilation systems to estimate the relative observation impacts among different types of observation platforms (e.g. Gelaro et al. 2010). Liu and Kalnay (2008) and Li et al. (2010) proposed an equivalent method formulated under the ensemble data assimilation system (i.e., EFSO) with no need of the adjoint model. Kalnay et al. (2012) further improved the formulation based on direct computation of the cost function, without computing its gradient. Ota et al. (2013) implemented the EFSO with the NCEP GFS model and demonstrated how to use this method to identify the observations that lead to a local forecast failure. The formulation used by Kalnay et al. (2012) and Ota et al. (2013) is briefly summarized below.

The model forecast started from t_i and validated at t is denoted by $\mathbf{x}^f_{t|t_i}$. The ensemble mean forecast errors started from $t = 0$ h and $t = -6$ h verified against the analysis at the verification time t are denoted by:

$$\mathbf{e}_{t|0} = \bar{\mathbf{x}}^f_{t|0} - \mathbf{x}^{\text{truth}}_t \text{ , and } \mathbf{e}_{t|-6} = \bar{\mathbf{x}}^f_{t|-6} - \mathbf{x}^{\text{truth}}_t \text{ , } \tag{7.1}$$

respectively. $\mathbf{x}^{\text{truth}}_t$ is estimated with a verifying analysis that can be from the same system or any other model analysis. As shown in Figure 7.1, the impact of assimilating observation $\mathbf{y}^o$ at $t = 0$ h is manifested by the difference between two

forecast errors ($\mathbf{e}_{t|0}$ and $\mathbf{e}_{t|-6}$), since the forecast started at $t = -6$ h serves as the first guess for the analysis at $t = 0$ h. Therefore, a cost function to measure the change in forecast errors made by the data assimilation is defined as:

$$J = \Delta e^2 = e_{t|0}^2 - e_{t|-6}^2 = \mathbf{e}_{t|0}^T C \mathbf{e}_{t|0} - \mathbf{e}_{t|-6}^T C \mathbf{e}_{t|-6} \,, \tag{7.2}$$

where C is a given norm operator defining the measure of the forecast errors. For norms of kinetic energy (KE), potential energy (PE), and moist energy (ME), $e^2 = \mathbf{e}^T C \mathbf{e}$ can be expressed as (Ehrendorfer et al. 1999):

$$e_{\mathrm{KE}}^2 = \frac{1}{2}\frac{1}{S}\int_S \int_0^1 (u'^2 + v'^2)\, d\sigma dS \,, \tag{7.3}$$

$$e_{\mathrm{PE}}^2 = \frac{1}{2}\frac{1}{S}\int_S \left[\int_0^1 \frac{C_\mathrm{p}}{T_\mathrm{r}}\, T'^2\, d\sigma + \frac{R_\mathrm{d} T_\mathrm{r}}{P_\mathrm{r}^2}\, P_\mathrm{s}'^2\right] dS \,, \tag{7.4}$$

$$e_{\mathrm{ME}}^2 = \frac{1}{2}\frac{1}{S}\int_S \int_0^1 \frac{L^2}{C_\mathrm{p} T_\mathrm{r}}\, q'^2\, d\sigma dS \,, \tag{7.5}$$

while the subscripts $t|0$ or $t|-6$ are neglected. Here u', v', T', P_s', and q' are the forecast errors of zonal wind, meridional wind, temperature, surface pressure, and specific humidity, respectively. C_p, R_d, and L are the specific heat at constant pressure, the gas constant of dry air and the latent heat of condensation per unit mass, respectively. T_r and P_r are the reference temperature and pressure, respectively. In this study, we use $T_\mathrm{r} = 280$ K and $P_\mathrm{r} = 1000$ hPa. In addition, the dry total energy (DTE) = KE + PE, and moist total energy (MTE) = KE + PE + ME can be easily computed within the EnKF which does not require linearization of the physical parameterizations. When the cost function (Δe^2) is negative (positive), it means a

reduction (increase) of forecast errors measured by the given norm at the evaluation time, and thus a positive (negative) impact by the data assimilation.

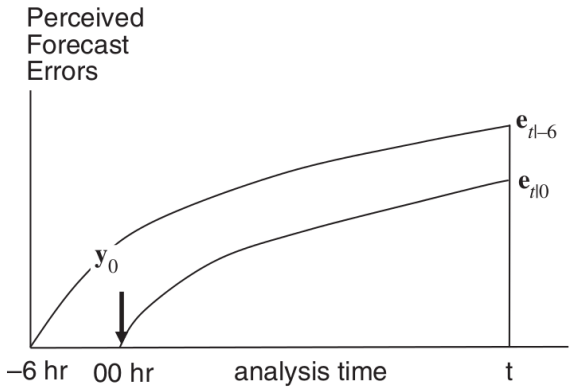

Figure 7.1: Schematic of the perceived forecast errors verified against the analysis at the verification time t from two forecasts started from the analysis at $t = 0$ h ($\mathbf{e}_{t|0}$), and from the analysis at $t = -6$ h ($\mathbf{e}_{t|-6}$). The only difference between the two forecasts is the assimilation of the observation $\mathbf{y}^o$ at $t = 0$ h. Adapted from Kalnay et al. (2012).

Following the derivation in Kalnay et al. (2012), the cost function can be approximated by:

$$\Delta e^2 \cong \frac{1}{K-1} \delta \mathbf{y}^T \, \mathbf{R}^{-1} \, \mathbf{Y}^a \, \mathbf{X}_{t|0}^{f\,T} \, C\left(\mathbf{e}_{t|0} + \mathbf{e}_{t|-6}\right), \tag{7.6}$$

where K is the ensemble size, $\delta \mathbf{y} = \mathbf{y}^o - \bar{\mathbf{y}}^b = \mathbf{y}^o - \overline{H(\mathbf{x}^b)}$ is the innovation vector, and $\mathbf{R}$ is the observation error covariance matrix as defined in Chapter 1.3. $\mathbf{Y}^a = \left[\mathbf{y}^{a(1)} - \bar{\mathbf{y}}^a, \ldots, \mathbf{y}^{a(K)} - \bar{\mathbf{y}}^a\right]$ is the matrix consisting of columns of analysis observation perturbations, and $\mathbf{X}_{t|0}^f = \left[\mathbf{x}_{t|0}^{f(1)} - \bar{\mathbf{x}}_{t|0}^f, \ldots, \mathbf{x}_{t|0}^{f(K)} - \bar{\mathbf{x}}_{t|0}^f\right]$ is the matrix consisting of columns of forecast ensemble perturbations started from $t = 0$ h and validated at the time t. With the EnKF system in which the covariance localization is

used, the impact of the lth observation on the forecast at the jth grid point can be computed by:

$$(\Delta e^2)_{j,l} \cong \frac{1}{K-1}(\delta \mathbf{y})_l \left[\rho_j \, \mathbf{R}^{-1} \, \mathbf{Y}^a \left(\mathbf{X}_{t|0}^{f\,T}\right)_j C_{jj} \left(\boldsymbol{e}_{t|0} + \boldsymbol{e}_{t|-6}\right)_j\right]_l , \qquad (7.7)$$

where ρ_j is the localization function on the grid point j. The total impact of a single observation can be obtained by simply summing up over j (grid points), and the total impact of any subset of observations can be obtained by summing up over the set of observations. Note that the localization function in Equation (7.7) may be different from that used in the EnKF analysis; for example, the localization center can be advected with the average wind speed in order to account for the propagation of the observation impact (Ota et al. 2013).

We implement the above formulation of EFSO into our GFS-LETKF system. Yoichiro Ota and Daisuke Hotta kindly provided their EFSO code and much help on this part of work. Note that in our system, the $\mathbf{Y}^a$ that appears in Equations (7.6) and (7.7) is obtained directly from the LETKF analysis equations [refer to Equation (1.6)]:

$$\mathbf{Y}^a = \mathbf{Y}^b \, \mathbf{W}^a , \qquad (7.8)$$

rather than applying the observation operator to the analysis ensemble $[H(\mathbf{X}^a)]$, in order to prevent some practical problems that make the latter way infeasible. For example, if one uses the latter way, the elements of $H(\mathbf{X}^a)$ passing the quality control may be inconsistent to the elements of $\mathbf{Y}^b$ passing the same quality control, so we are not able to obtain the complete set of the observations in the analysis. Besides, for a time-integral quantity such as the 6-hour accumulated precipitation, it is also impossible to compute $\mathbf{Y}^a$ through the observation operator applied to the analysis ensemble.

7.3 Experimental design

According to our purpose, we need to first obtain a large sample of the observation impact of each single precipitation observation. We would like to have the EFSO values not only for the good precipitation observations, but also for the other bad observations, in order to comprehensively assess the usefulness of all precipitation data in every situation. Therefore, we decide to dismiss all quality control criteria previously used in our precipitation assimilation (e.g., the 24mR criterion and the Corr0.35 criterion; refer to Section 6.2.2) except the basic gross error control. However, if we conduct a cycling assimilation of precipitation without using these criteria, the analysis and thus the background would become very bad after a few cycles, which would be not representative of a "normal" model background. To solve this problem, cycling assimilation of precipitation is intentionally avoided; instead, each cycle of assimilation of precipitation is separately initialized from the ensemble analyses of an independent rawinsonde-only GFS-LETKF cycling run, and the EFSO values for each observation are thus computed from these discontinuous cycles. This procedure is shown in Figure 7.2, which is actually an extension of the procedure used to generate the sample for the Gaussianity statistics described in Chapter 5.4. Step by step, in each (discontinuous) cycle, 9-hour ensemble GFS forecasts are conducted (blue lines in Figure 7.2), and the observations are assimilated with the LETKF (black dashed lines in Figure 7.2), and then the additional ensemble forecasts initialized from the LETKF analysis (red lines in Figure 7.2) and also the ensemble mean forecast initialized from the LETKF first guess (or the LETKF analysis in the previous cycle; cyan lines in Figure 7.2) are conducted. The results

after the above steps are therefore sufficient to compute the EFSO for the observations assimilated in the second step (black dashed lines in Figure 7.2). As we did with the Gaussianity statistics in Chapter 5.4, in order to save computational time but still collect samples over one year, this EFSO computation is conducted by skipping 4 of every 5 cycles (30 hours) in the year 2008. The use of 30 hours instead of a multiple of a day is to avoid always computing the EFSO in the same time of the diurnal cycle.

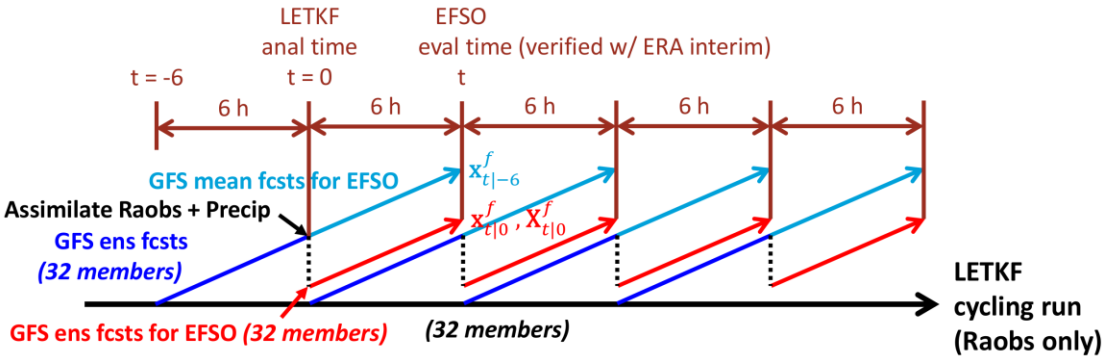

Figure 7.2: Formation of samples of observation impacts computed by the EFSO. Note that in our study, cycles in between every 5 cycles are skipped in order to save computational time.

Ota et al. (2013) used 24 hours as the evaluation forecast time. Inspired by the research carried out by Daisuke Hotta, in this study we compared the precipitation EFSO results using a 6-, 12-, and 24-hour evaluation forecast time and, in agreement with his previous results, we found that there are qualitatively no distinct differences among these choices (no shown). As pointed out by Hotta, there are several advantages to use a shorter evaluation time: First, the EFSO computation becomes computationally cheaper; Second, the advection of localization functions (Ota et al.

2013) may not be required since the observation impacts have not propagated far away; Third, it also benefits the implementation of the proactive quality control (Ota et al. 2013; Hotta et al. 2013). Therefore, the evaluation forecast time t of the EFSO computation is set to 6 hours (as shown in Figure 7.2), and the advection of localization functions (Ota et al. 2013) is not used.

7.4 Results

7.4.1 Global distributions of precipitation observation impacts

Based on the 1 year (30 hourly) samples of the precipitation EFSO described above, Figure 7.3 shows the maps of average observation impacts (i.e., changes in 6-hour forecast errors) of precipitation measured by the MTE norm, using the GTbz transformation of precipitation. Figure 7.3a shows the results with all precipitation observations (passing the basic gross error control in the LETKF) and Figure 7.3b shows the results with only precipitation observations passing the 24mR criterion (more than 23 precipitating members in the background). Green (red/yellow) shading colors stand for the positive (negative/neutral) impacts or reduction (increase/no change) in forecasts errors. Overall, the areas most benefitted by the precipitation assimilation are the storm-track regions, located within 30–50 degree north and south over the three major oceans. Most of the ocean shows positive impacts. The tropical region and the land show marginal or negative impacts. Particularly, the marine stratocumulus regions, Africa, and the Tibetan Plateau show the worst impacts. The magnitudes of impacts in terms of forecast errors are very non-uniform, with average error reduction as much as 60×10^{-4} J kg^{-1} in the extratropical storm-track regions

but less than $\pm 5 \times 10^{-4}$ J kg^{-1} in many other regions (note that the color scale in the figure is nonlinear). It is important to note that Figure 7.3 suggests that precipitation observations at latitudes beyond 50 degree north and south may lead to large positive impacts as well. These regions are not covered by the TMPA data since the orbit of the TRMM satellites has lower inclination, but the incoming data from the GPM mission will cover these higher-latitude regions. The global distribution of these EFSO results is somewhat similar to the non-Gaussianity map shown in Chapter 5.4 and the correlation map shown in Section 6.2.2, but differences still exist. Comparison among these figures will be discussed in Chapter 7.5.

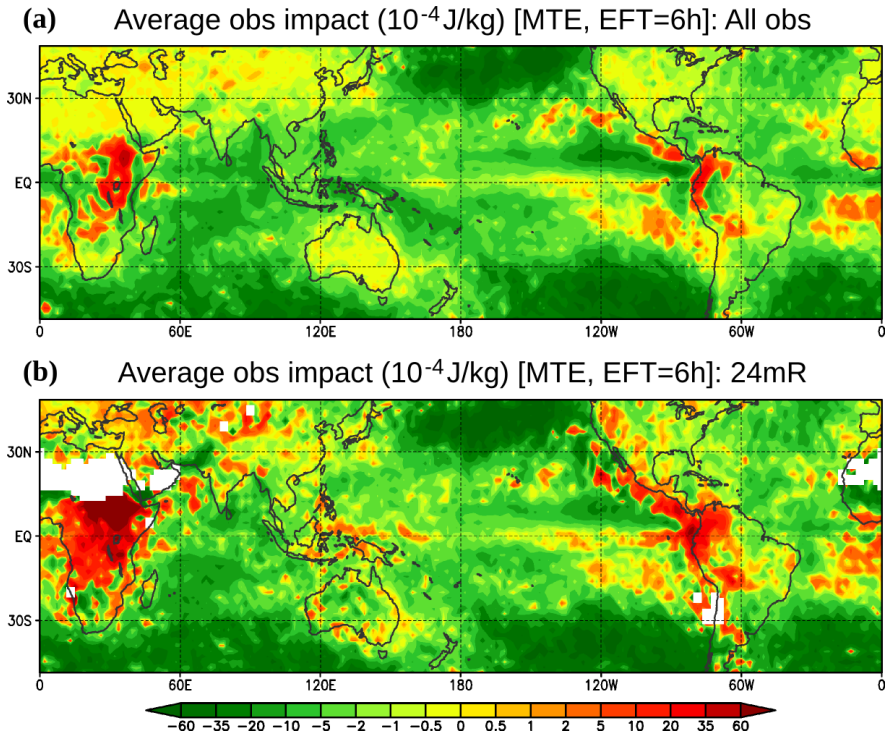

Figure 7.3: The maps of average observation impacts (i.e., change in 6-hour forecast errors) of precipitation measured by the moist total energy norm (10^{-4} J kg^{-1}). (a) All precipitation observations; (b) precipitation observations with more than 24 precipitating members in the background. The GTbz transformation of precipitation is used.

Interestingly, over those negative impact regions, the average negative impacts of only the precipitation observations passing the 24mR criterion is even larger (Figure 7.3b) than those of all precipitation observations. This is probably because the 24mR criterion only picks up observations with sufficient ensemble spread in the background, so it actually tends to pick up the high-impact (both positive and negative impacts) observations, thus the net effect is to amplify both the positive and negative impacts. Note that in our cycling precipitation assimilation experiments in Chapter 6, the precipitation observations in the average negative impacts areas are mostly not assimilated because of the use of the Corr0.35 criterion.

The overall effect of the precipitation assimilation can also be shown with the rate of observations leading to positive impacts (i.e., reduction in 6-hour forecast errors). For a type of observations with very non-uniform impacts, this index could lead to different pictures of effectiveness of assimilating observations than the simple arithmetic mean error reduction. As shown in Figure 7.4, the distribution of the positive impact rate is generally similar to the average impacts (Figure 7.3), but the "bad" regions over the land are much clearly highlighted with the positive impact rate. If no background based quality control (XmR criterion) is used, the positive impact rate is less than 50% in almost all land regions. However, the 24mR criterion can greatly increase the positive impact rate, leading to much wider areas having greater-than-50% positive impact rates, even over the land.

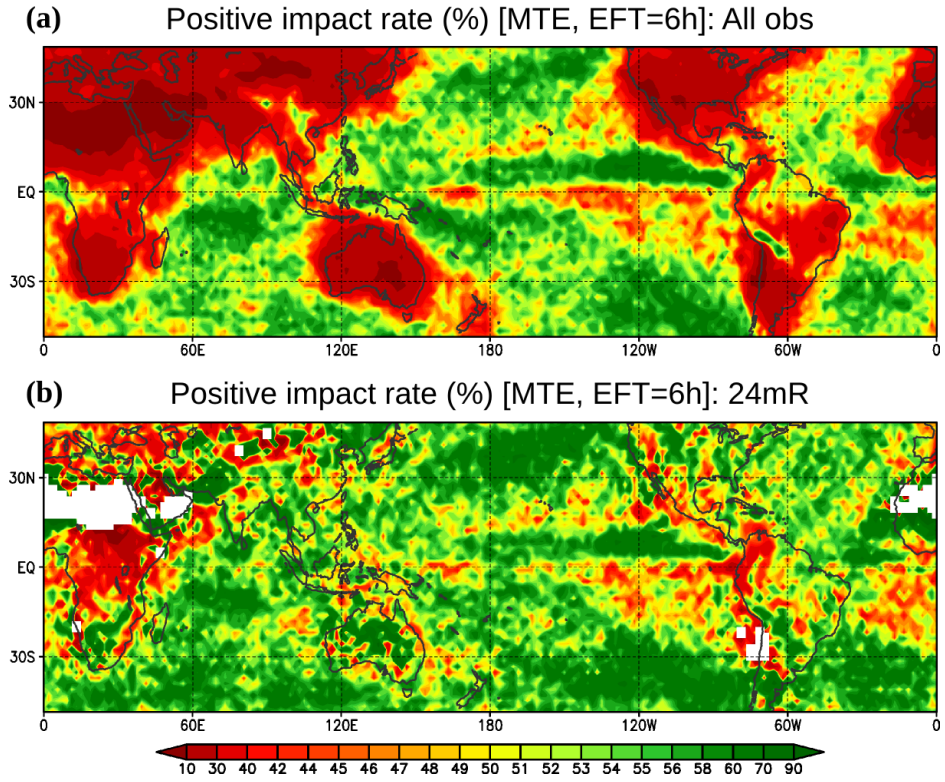

Figure 7.4: As in Figure 7.3, but for the percentage (%) rate of observations leading to positive impacts (i.e., reduction in 6-hour forecast errors).

7.4.2 Observation impacts with respect to precipitating members

In addition to spatially averaging the observation impacts computed by the EFSO, we can also average them in terms of other factors, such as the numbers of precipitating members in the background, and the observed precipitation amounts. This can be a powerful methodology to verify the conclusions we reached in the previous assimilation experiments. In this section, we show the results with respect to the number of precipitating members.

Figure 7.5 shows the average observation impacts of precipitation (10^{-4} J kg^{-1}), measured by different energy norms, versus the numbers of precipitating members in

the background. The GTbz transformation of precipitation is used in the assimilation. It is found that, in terms of all energy norms, the forecast error reduction increases with the number of precipitating members when it is less than about 16–24 (out of 32), and then slightly decreases when the number increases from 24 to 32. When the precipitating members are few, the average impacts are very small or even negative (in the KE norm), which is consistent to our previous finding that assimilating precipitation with too few background precipitating members can be harmful (Section 3.5.1). On the other hand, a possible explanation of the decreasing trend of the error reduction when the number of precipitating members increases from 24 to 32 is that the model background is already accurate in this regime, so the average impacts by assimilating the precipitation observations are smaller. Comparing among the KE, PE, and ME norms, it is found that the impact on the KE norm is the largest, the impact on the ME norm is the second, and the impact on the PE norm is the smallest, roughly with a ratio of 4:3:2. The large impact on the KE norm would be critical for improving the longer-term model forecasts, and the also large impact on the ME norm indicates the benefits of precipitation assimilation on improving the moisture field. Besides, the maximum moist error reduction is found more towards fewer precipitating members (about 16), as compared to other energy norms. The DTE (i.e., KE + PE) and MTE (i.e., KE + PE + ME) represent the combined effects of these independent norms. In our other figures in this chapter, we only show the results with the MTE norm.

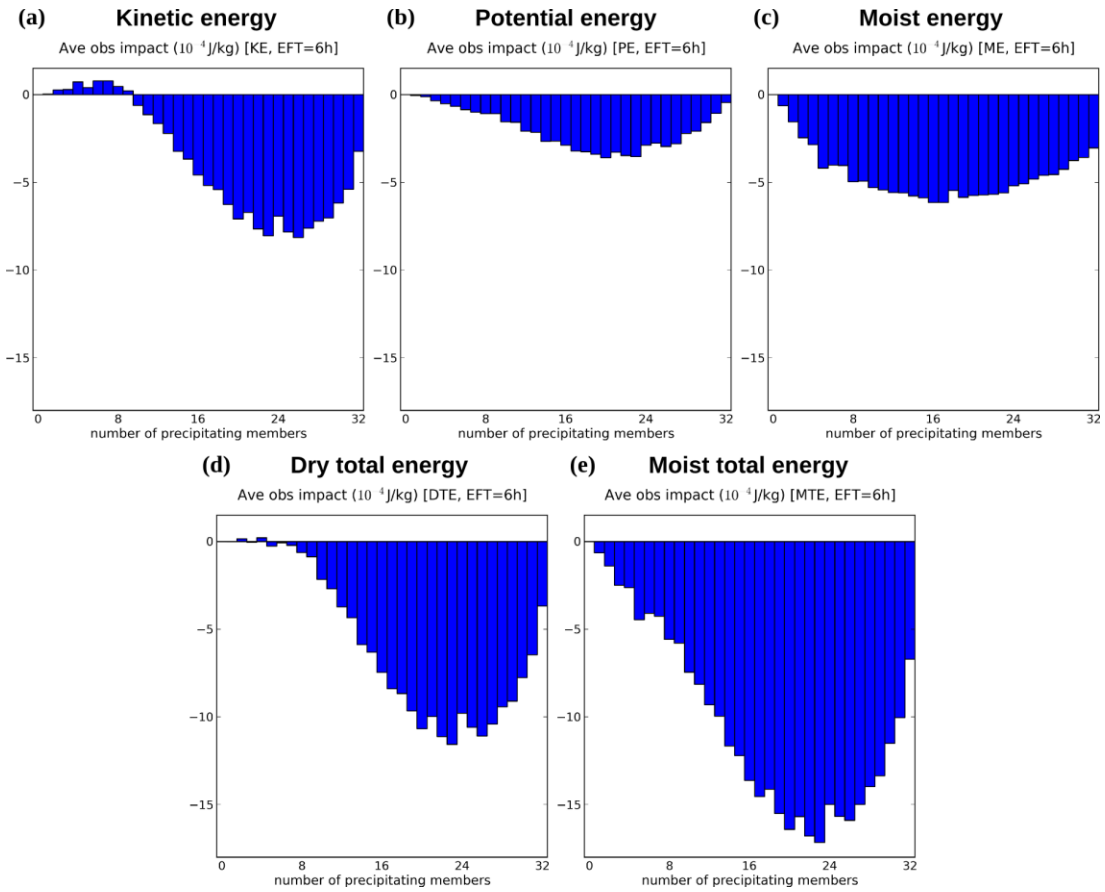

Figure 7.5: The average observation impacts of precipitation (10^{-4} J kg^{-1}), measured by (a) the kinetic energy norm, (b) the potential energy norm, (c) the moist energy norm, (d) the dry total energy norm, and (e) the moist total energy norm, versus the numbers of precipitating members in the background. The GTbz transformation of precipitation is used.

In addition to the average observation impacts, the rate of observations leading to positive impacts, in terms of the MTE norm, versus the number of precipitating members is shown in Figure 7.6d. This index also displays an increasing trend with the increasing precipitating members. The positive impact rate is about 54% when all background members are precipitating. However, it is a little bit surprising that the greather-than-50% positive impact rates are seen at all numbers of precipitating

members except only for completely all zero precipitation in the background ensemble. This is in contrast with our experimental results with the SPEEDY and GFS models, where the precipitation observations with too few background precipitating members are actually difficult to use.

In the other subplots in Figure 7.6, we add a condition of observed zero or positive precipitation in the EFSO statistics. In the case of the positive precipitation observations, both the average error reduction and the positive impact rates are much larger than when all observations are considered. The average error reduction peaks at 17 precipitating members, and the positive impact rate can be as large as 60–70%. On the other hand, in the case of zero precipitation observations, the positive observation impact is smaller. The average impact becomes negative when the number of precipitating members is less than or equal to 20. The positive impact rate is also less than 50% when the number of precipitating members is less than 28. These results lead to a conclusion that the zero precipitation observations are more difficult to use in the data assimilation, which is consistent to our experience. However, when there are enough members having positive precipitation values in the background, the zero precipitation observations can still be useful and lead to positive impacts of 6-hour forecast errors because they can correct large model forecast errors.

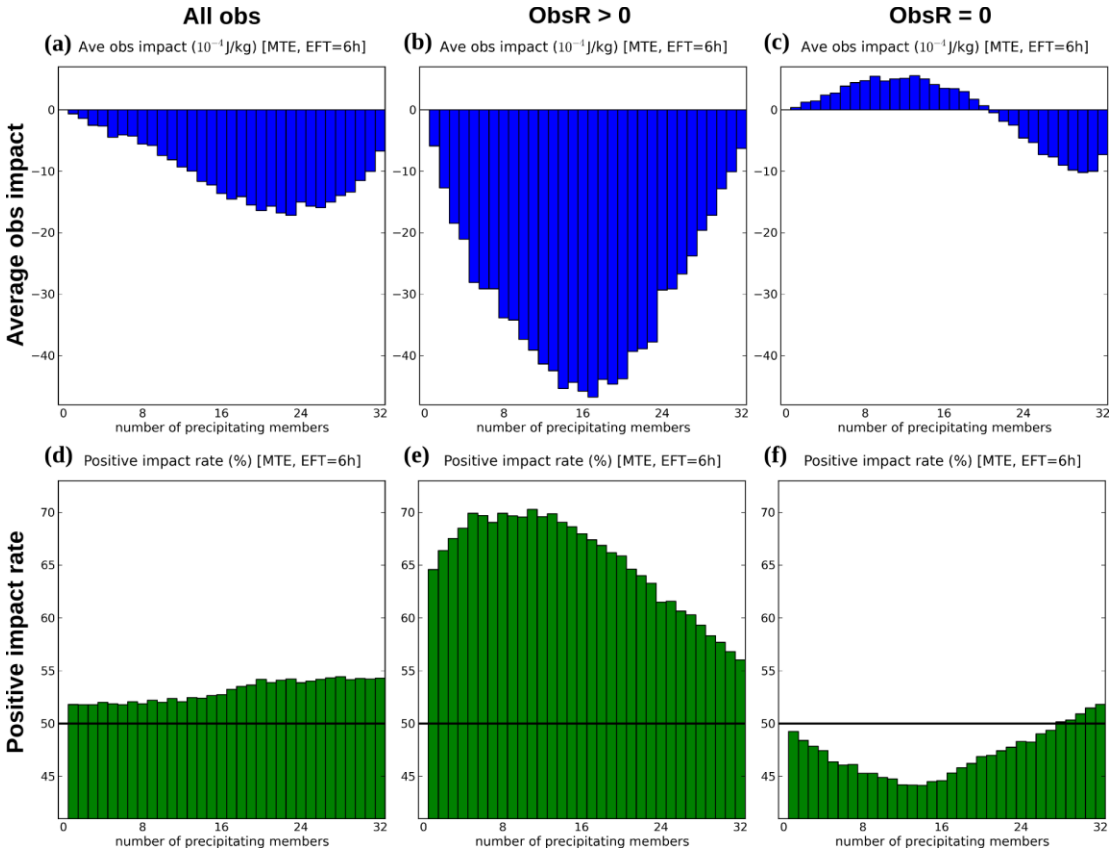

Figure 7.6: (a)–(c) The average observation impacts of precipitation (10^{-4} J kg^{-1}) and (d)–(f) the rate (%) of observations leading to positive impacts, measured by the moist total energy norm in 6-hour forecasts, versus the numbers of precipitating members in the background. (a) (d) All precipitation observations; (b) (e) positive precipitation observations; (c) (f) zero precipitation observations. The GTbz transformation of precipitation is used.

7.4.3 Observation impacts with respect to observed precipitation values

Figure 7.7 shows the average observation impacts of precipitation and the rate of observations leading to positive impacts with respect to the precipitation amount in the observations. In Figure 7.7a, c, all observations are considered (passing the basic gross error control that observations whose innovation magnitudes are greater than 5

times of the observation errors are discarded); in Figure 7.7b, d, only the observations passing the 24mR criterion are considered. The GTbz transformation of precipitation is still used. It is shown that the average observation impacts generally increase with the observed precipitation amount, but become saturated near 10 mm $(6h)^{-1}$. The positive impact rates can be higher than 60% when the observed precipitation amounts are greater than 1.2 mm $(6h)^{-1}$. The zero precipitation observations are not very useful. When no background based quality control is applied, the average observation impact is marginal but the positive impact rate is only 36%; when the 24mR criterion is imposed, the average forecast error reduction becomes notable and the positive impact rate becomes slightly greater than 50%. Therefore, the conclusion regarding the effectiveness of the zero precipitation observations is the same as the previous subsection: they can be useful only when the ensemble model background have enough positive precipitating members.

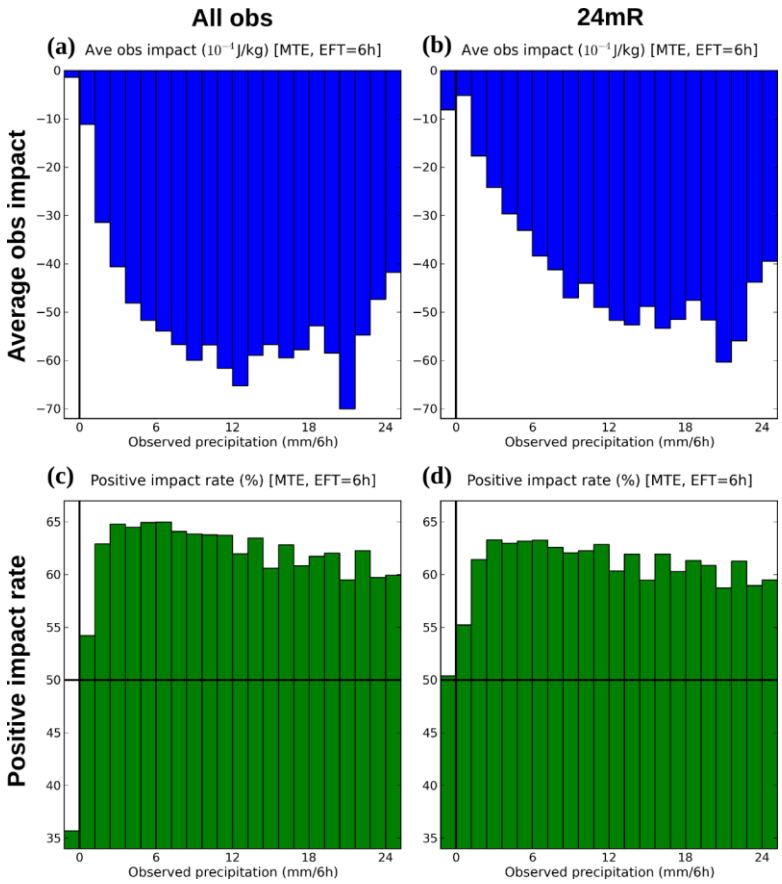

Figure 7.7: (a) (b) The average observation impacts of precipitation (10^{-4} J kg^{-1}) and (c) (d) the rate (%) of observations leading to positive impacts, measured by the moist total energy norm in 6-hour forecasts, versus the observed precipitation values [mm $(6h)^{-1}$]. (a) (c) All precipitation observations; (b) (d) precipitation observations with more than 24 precipitating members in the background. The GTbz transformation of precipitation is used.

7.4.4 Observation impacts using different transformation methods

Figure 7.8 shows the average observation impacts of precipitation using different transformation methods in the LETKF assimilation. The two Gaussian transformation methods with different algorithms to transform the zero precipitation lead to very similar EFSO results, both in the magnitudes of the average impacts and in the

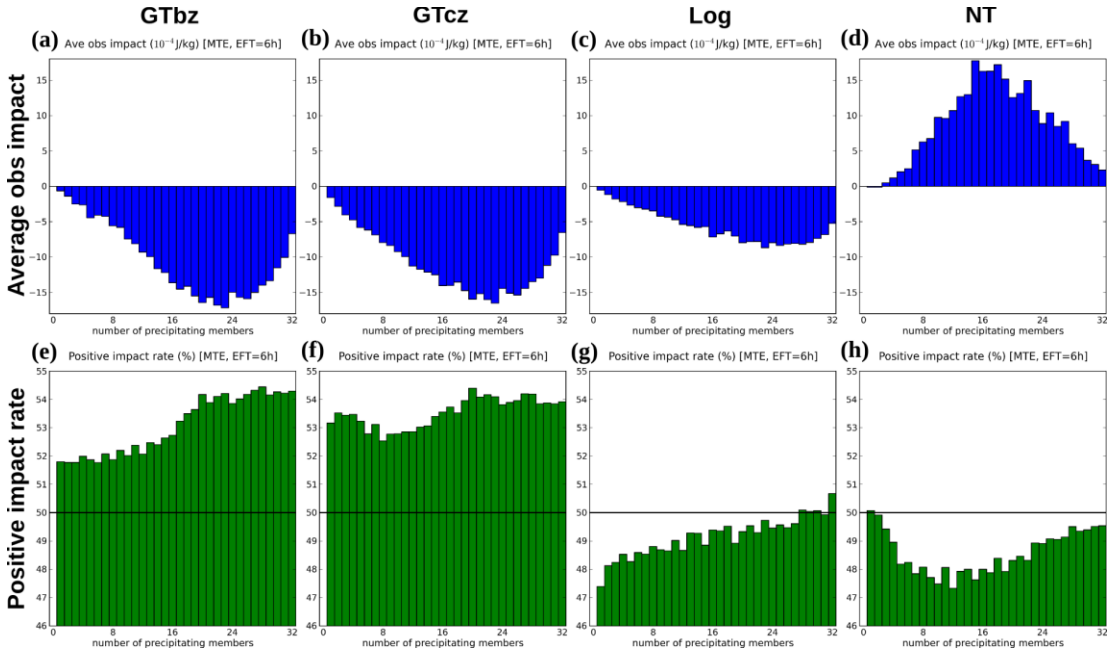

Figure 7.8: (a)–(d) The average observation impacts of precipitation (10^{-4} J kg^{-1}) and (e)–(h) the rate (%) of observations leading to positive impacts, measured by the moist total energy norm in 6-hour forecasts, versus the numbers of precipitating members in the background, using (a) (e) the GTbz, (b) (f) the GTcz, (c) (g), the logarithm, and (d) (h) no transformation of precipitation.

relationship with number of precipitating members in the background. Specifically, the GTbz method shows slightly better impacts when the background precipitating members are many but the GTcz method performs slightly better when the background precipitating members are few. The logarithm transformation (Log) also results in average positive impacts and also favors more background precipitating members, while the positive impact rates are only close to or less than 50%. However, if no transformation of precipitation is used (NT), the EFSO results are very bad. The observation impacts are all negative (increase in forecast errors), regardless of the

number of precipitating members in the background. Looking at the contribution of separate energy norms, we find the precipitation assimilation without transformation is most deteriorating in the ME norm and also the PE norm (not shown). With this comparison of the EFSO results with different transformation methods, we reach the same conclusion regarding the effects of the precipitation transformations as what we found in the real precipitation assimilation experiments (Section 6.3.1). Therefore, the usefulness and the accuracy of the EFSO computation are confirmed.

7.5 Reconsideration of the quality control criteria

So far we have seen several similar maps showing the geographic distributions of different factors regarding the effectiveness of the precipitation assimilation, including the correlation between the model background precipitation and precipitation observations in long-term samples (Figure 6.1), the average (non)Gaussianity of the background errors of precipitation (Figure 5.12), the average observation impacts (Figure 7.3) and the positive impact rates (Figure 7.4) of precipitation observations computed by the EFSO method. We put these figures together in Figure 7.9 for comparison. To make the comparison easier, the same color sequence is used. The green shading colors represent "good" numbers for the precipitation assimilation: high correlation between the model backgrounds and observations, high Gaussianity of the background errors, large forecast error reductions, and high positive impact rates; the red shading colors represent the opposite directions ("bad" numbers); and the yellow shading color is in between.

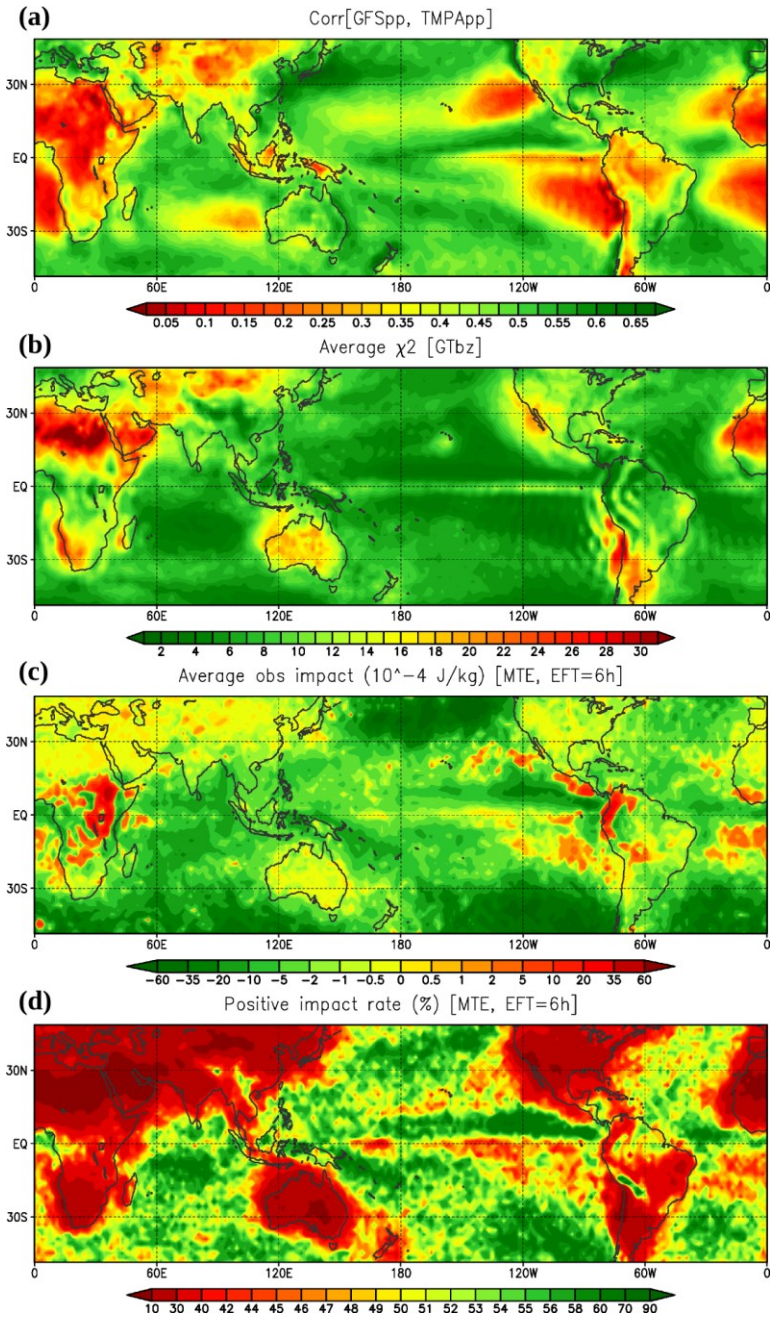

Figure 7.9: The maps of (a) correlation between precipitation in the GFS model backgrounds and in the TMPA observations, (b) the average χ^2 values (a measure of non-Gaussianity) of background precipitation errors, (c) the average observation impacts of precipitation (10^{-4} J kg^{-1}), and (d) the rate (%) of observations leading to positive impacts measured by the moist total energy norm in 6-hour forecasts during (a) the 2001–2010 period, (b)–(d) the year 2008. The GTbz transformation of precipitation is used in all figures.

All of these figures show that the precipitation assimilation is generally more useful over the ocean than the land. The tropical region, the marine stratocumulus regions, Africa, and the Tibetan Plateau are the regions where the precipitation assimilation could be harmful. Among the four figures, the correlation map (Figure 7.9a) and the average EFSO map (Figure 7.9c) are the two that most resemble each other, but it is noted that the color scale is linear in the correlation map but very nonlinear in the EFSO map. The Gaussianity map (Figure 7.9b) is similar to the previous two in most regions, but it does not show warning signs over the marine stratocumulus regions, where the precipitation assimilation should be very difficult because of the large inconsistency between the model precipitation climatology and the observation climatology. The tropical ocean is also too "good" compared to the previous two maps. It is not surprising that this Gaussianity figure cannot show bad signals over these regions, since it is the only factor among four that only considers the model background but does not take into account the observations, so it does not "know" about the inconsistency between the model and the observations. Lastly, the positive impact rate map (Figure 7.9d) puts too much highlight over the bad regions. Almost all land areas show less-than-50% rates of positive impacts. It may be a widely used index for us to present the EFSO results but may not be a good index to indicate the effectiveness of precipitation assimilation.

In all, we think the correlation map and the average EFSO map are the two maps that better indicate the "good" and "bad" regions for assimilating precipitation. In our real precipitation assimilation experiments, we actually used the correlation as the index to define the Corr0.35 quality control criterion (i.e., precipitation is assimilated

only at where the correlation between the model backgrounds and observations are higher than 0.35) and thus obtained good results of the precipitation assimilation (Section 6.2.2). One of the advantages of this choice is that the correlation map can be easily computed given the long-term samples of the model background and observations. In contrast, the EFSO may be the best index of the effectiveness of the precipitation assimilation since it is exactly the estimate of the forecast error reduction, but the computation is more complex and may not be possible to prepare it in advance of the precipitation assimilation. However, the "proactive quality control" method proposed by Ota et al. (2013) and Hotta et al. (2013) that uses short-term EFSO to refine the quality control should be a promising method for the precipitation assimilation.

7.6 Summary and discussion

The ensemble forecast sensitivity to observations (EFSO) method is used in this chapter to gain more insights on the precipitation assimilation. It is a powerful technique to systematically estimate the impact on the short-range forecasts by any subset of observations in the same time, with only a small amount of additional computation. We computed the 6-hour EFSO for every single precipitation observation every 30 hours over one year. Since all good and bad precipitation observations are assimilated in order to compute their EFSO, we do not carry out cycling assimilation so that the continuous degradation of the analysis and the background is prevented.

By averaging the observation impacts in terms of various factors, such as geographic locations, numbers of precipitating background members, and the

observed precipitation amounts, the findings coming from the EFSO and our previous precipitation assimilation experiments regarding the effectiveness of the precipitation assimilation in every situation are found to agree well. The spatial map of the average EFSO is similar to the map of correlation computed between the long-term samples of GFS model background precipitation and the TMPA data, showing the best impacts over most ocean areas, marginal impacts in the tropics, and the worst impacts over the marine stratocumulus regions, Africa, and the Tibetan Plateau areas where the model precipitation is not accurate when compared to observations.

The forecast error reduction increases with the number of precipitating members when it is less than about 16–24 (out of 32), and then slightly decreases with the number when it is close to all-member precipitation. The precipitation assimilation helps to reduce the 6-hour forecast errors measured by all of the KE norm, PE norm, and ME norm, while the impacts on the KE norm is the largest and the impact on the PE norm is the smallest. The zero precipitation observations are more difficult to use in the data assimilation than the positive precipitation observations. The existence of clear positive impacts by zero precipitation observations is only possible when the majority of the members has positive precipitation values in the background (i.e., when most of the forecasts are wrong). In addition, among the different precipitation transformation algorithms, the GTbz and GTcz methods result in quite similar observation impacts. The logarithm transformation also works for precipitation assimilation, but with smaller impacts. The precipitation assimilation without using any transformation leads to very poor results.

All of the results are generally consistent to what we found with the SPEEDY OSSEs and the GFS model experiments. One of the notable differences here is that the precipitation EFSO results seem to indicate that the average impact of precipitation assimilation can be still positive when there are fewer (i.e., 8–16) precipitating members in the background, while in our experience this category of observations can lead to degradation. We think that the EFSO results may be too optimistic compared to reality, but it may also indicate that there are still room for improvement if we can make better use of the precipitation observations in this category.

This chapter also provides a demonstration of how the EFSO can be used to analyze the effectiveness of ineffectiveness of a new observing system. In this dissertation, we first conducted a great number of the assimilation experiments before doing the EFSO computation and then used the EFSO to verify our assimilation strategies, but the opposite route may also be workable. Since we are able to efficiently obtain a grand picture of the observation impacts by the EFSO method without conducting many computationally expensive OSEs, appropriate assimilation strategies for a new observing system may be developed faster. In addition, the proactive quality control based on the EFSO may also be implemented to further improve the data assimilation results.

Chapter 8: Summary and future directions

8.1 Summary

This dissertation investigates the assimilation of global large-scale satellite precipitation data using the LETKF. Assimilation of precipitation has been a difficult topic because of the nonlinear observation operator related to the model precipitation parameterization, the non-Gaussianity of precipitation variables, the large and unknown model errors and observation errors. Most of the past studies to assimilation precipitation have used nudging or variational methods, and the general experience is that it is relatively easier to force the forecasts of precipitation to be close to the observed precipitation during the assimilation, but the resulting forecast impacts quickly decay after a day or less.

In this study, we use the LETKF method to assimilate the precipitation. The LETKF does not require linearization of the model, and the ensemble can give the "error correlation of the day", essential to produce optimal analyses. Therefore, the EnKF is expected to be able to more efficiently improve all "master" variables in the model compared to nudging or variational approaches, and thus lead to improvement in longer-term model forecasts. In addition to using the LETKF, we propose to use the Gaussian transformation for precipitation based on its climatological distribution in the model and observations, and also some quality control criteria specialized for precipitation. The precipitation observations are assimilated only when there are enough background members having positive precipitation (XmR criterion) and, in the case that the model or observation may have large errors, only at the location

where the model climatology and the observation climatology show adequate correlation (CorrX criterion).

We test our ideas of precipitation assimilation in two systems of different complexity. The proof-of-concept experiments are conducted with the SPEEDY model, which is a simplified but still realistic GCM. Within an identical-twin OSSE framework, we achieve larger improvement in both the analysis and the 5-day forecasts by assimilating global precipitation. The effect of precipitation assimilation is largest in the southern hemisphere extratropical region where the rawinsonde observations are sparse. The tropical region shows the least improvement probably because of its prevailing convective precipitation type.

After the success in this proof-of-concept system, the precipitation assimilation experiments are further conducted with the NCEP GFS model, assimilating the real TMPA satellite precipitation data. Since the model errors and observation errors are large in the real case, a naïve replication of the SPEEDY model experiments would not lead to acceptable results. Therefore, we first compute several statistics with the precipitation variable in the model background and observations from the point of view of the LETKF data assimilation. Based on the insight gained from the statistical results, we refine the Gaussian transformation method considering both the model climatology and the observation climatology to better extract information form the "useful" part of the observation data, and define effective quality control criteria to reject the other "difficult-to-use" part of observation data. Consequently, we obtain, for the first time, positive results using a realistic model (GFS) and real data (TMPA). The GFS model experiments show improvements in both the analysis and 5-day

forecasts, which is qualitatively comparable to our results of the SPEEDY model experiments.

In the last part of this dissertation, the EFSO of a sample of precipitation data is computed. By averaging the observation impacts in terms of various factors, the validity of our methods of precipitation assimilation, such as the XmR and CorrX criteria, and the Gaussian transformation of precipitation, are verified. The EFSO approach, as demonstrated here, has been shown to be an efficient way to assess the effectiveness of any new observing system, and thus to develop appropriate assimilation strategies of it, rather than the standard observing system experiments normally used to estimate the impact of the new type of observations on the forecasts.

We note that although we test the precipitation assimilation not only in the idealized system but also in the realistic system, the complexity of our realistic system is still less than operational NWPs. The resolution of the GFS model used in our study is still low, and we use a rawinsonde-only experiment as the baseline in order to have large room for improvement. In addition, we only focus on the assimilation of the global low-resolution precipitation data to improve the large-scale analysis and forecasts. The observation data are made by conducting spatial/temporal averages of the high-resolution raw data. Therefore, our strategies need to be modified in order to be applicable to the assimilation of convective scale precipitation, such as meteorological radar observations.

Nevertheless, this dissertation shows, for the first time, the great potential of the remote-sensed precipitation data to improve the medium-range model forecasts. A more in-depth understanding of the merit and the limitation of the precipitation

assimilation has been gained, especially for the ensemble data assimilation systems. Many assimilation and diagnostic methods used in this study can only be implemented with ensemble systems, such as the quality control based on the number of precipitating members in the background, the Gaussianity statistics of the background error distribution, and the EFSO diagnostics. Therefore, this study contributes to our knowledge of the precipitation assimilation using the ensemble data assimilation methods.

8.2 Future directions

In the short term, we would like to finish some parts of work that are closely related to the outline of this dissertation but have not yet been done, including the verification of the precipitation forecasts and the separation of large-scale and convective precipitation during the assimilation. We showed the precipitation assimilation improves the 5-day forecasts in the GFS model in terms of winds, temperature, and moisture variables, but did not show the verification of the precipitation forecasts. It is not good to verify the precipitation by computing the RMS errors and biases as we did for other variables because of the very non-uniform characteristics of the precipitation field. Some other scores such as the equitable threat score (ETS; Hamill and Juras 2006) may be used.

In Chapter 6, we defined the quality control of precipitation assimilation based on the number of the precipitating members in the background and the correlation between the model background and the observations in long-term samples, and in Chapter 7, we compared the average observation impacts using the EFSO method, grouped by these factors. Our results suggest that the precipitation types (e.g.,

stratiform or convective precipitation) can be another important factor that can help us to refine the assimilation of precipitation. After examining the statistical characteristics of different precipitation types, we can adopt separate procedures to different precipitation types. This separate consideration of different types of precipitation data would be advantageous to gain more understandings of the precipitation assimilation and could lead to additional improvement of the model analysis and forecasts.

As to the longer-term directions, we would like to exploit more the power of the ensemble data assimilation. The precipitation in the model is a diagnostic variable that does not affect the subsequent model forecasts; therefore, in our study, the precipitation variable is not updated during the LETKF assimilation. This leads to no improvement of the model precipitation in the analysis time ($t = 0$). However, with the ensemble method, we can easily apply a no-cost smoother (Kalnay et al. 2007) so that the model can "reproduce" the precipitation output at the analysis time based on the improved first guess 6 hours ago, thus we should be able to obtain better precipitation analyses. Besides, since the precipitation is tightly related to the past trajectory of the model moist physics, more sophisticated methods, such as the "running in place" (RIP; Kalnay and Yang 2010; Yang et al. 2012), could also be used in order to more efficiently adjust the past model trajectory towards the observations. These techniques may not necessarily bring advantages over the operational NWP, but they can be very useful in creating a global precipitation analysis that is consistent to both the model dynamics and the source observations.

Additionally, as demonstrated in Chapter 7, the EFSO method is a very promising tool to systematically investigate the effectiveness or ineffectiveness of a new observing system. A more in-depth study of the application of the EFSO to the precipitation assimilation is recommended. In particular, Ota et al. (2013) and Hotta et al. (2013) proposed the proactive quality control method based on the EFSO, which can pick up good observations for data assimilation and use them in a cycling run. By this method, we may be able to know the potential "best" impact of an observation dataset given the existent data assimilation system.

The other possible future directions are listed as follows:

- After we are confident with our method of precipitation assimilation, we can use a more accurate baseline experiment instead of the rawinsonde-only experiments in Chapter 6, and assimilate precipitation on top of it. This can help us to gain an idea about the benefits of the precipitation assimilation in the state-of-the-art operational NWP when many other types of observations are already used.
- The determination of the observation errors of the precipitation observations is a topic that we have not addressed in this dissertation. A better way to investigate this issue would be to use some kind of adaptive methods to objectively determine the observation error under the assimilation system. For example, following Li et al. (2009), the optimal observation errors can be estimated based on the innovation vector statistics with an ensemble data assimilation system.

- The proposed Gaussian transformation is a general transformation method that can be applied to any variable as long as we know its long-term cumulative distribution in the model and/or the observation data. It would be worthwhile to apply this technique to other highly non-Gaussian variable, especially for those moisture-related variables.
- The Global Precipitation Measurement (GPM) mission is the successor of the TRMM project. It is expected to be able to provide more accurate real-time precipitation estimates at a better spatial/temporal coverage. Therefore, using the GPM data that will be available in the near future, larger impacts of the assimilation of precipitation are expected. In particular, the GPM can measure the precipitation at the latitudes beyond 50 degree north and south. Based on our EFSO results, these extratropical precipitation data may be very valuable for data assimilation.
- In addition, as indicated before, combining the power of the LETKF and GPM and other satellite precipitation estimations can create a more accurate global reanalysis of precipitation and its properties.

Bibliography

Anderson, J. L., 2010: A non-Gaussian ensemble filter update for data assimilation. *Mon. Wea. Rev.*, **138**, 4186–4198, doi:10.1175/2010MWR3253.1.

Bauer, P., J.-F. Mahfouf, W. S. Olson, F. S. Marzano, S. D. Michele, A. Tassa, and A. Mugnai, 2002: Error analysis of TMI rainfall estimates over ocean for variational data assimilation. *Quart. J. Roy. Meteor. Soc.*, **128**, 2129–2144, doi:10.1256/003590002320603575.

Bauer, P., G. Ohring, C. Kummerow, and T. Auligne, 2011: Assimilating satellite observations of clouds and precipitation into NWP models. *Bull. Amer. Meteor. Soc.*, **92**, ES25–ES28, doi:10.1175/2011BAMS3182.1.

Bengtsson, L., K. I. Hodges, and L. S. R. Froude, 2005: Global observations and forecast skill. *Tellus A*, **57**, 515–527, doi:10.1111/j.1600-0870.2005.00138.x.

Bocquet, M., C. A. Pires, and L. Wu, 2010: Beyond Gaussian statistical modeling in geophysical data assimilation. *Mon. Wea. Rev.*, **138**, 2997–3023, doi:10.1175/2010MWR3164.1.

Bowman, K. P., 2005: Comparison of TRMM precipitation retrievals with rain gauge data from ocean buoys. *J. Climate*, **18**, 178–190, doi:10.1175/JCLI3259.1.

Chao, W. C., 2013: Catastrophe-concept-based cumulus parameterization: Correction of systematic errors in the precipitation diurnal cycle over land in a GCM. *J. Atmos. Sci.*, **70**, 3599–3614, doi:10.1175/JAS-D-13-022.1.

Dai, A., 2006: Precipitation characteristics in eighteen coupled climate models. *J. Climate*, **19**, 4605–4630, doi:10.1175/JCLI3884.1.

Davolio, S., and A. Buzzi, 2004: A nudging scheme for the assimilation of precipitation data into a mesoscale model. *Wea. Forecasting*, **19**, 855–871, doi:10.1175/1520-0434(2004)019<0855:ANSFTA>2.0.CO;2.

Ebert, E. E., J. E. Janowiak, and C. Kidd, 2007: Comparison of near-real-time precipitation estimates from satellite observations and numerical models. *Bull. Amer. Meteor. Soc.*, **88**, 47–64, doi:10.1175/BAMS-88-1-47.

Ehrendorfer, M., R. M. Errico, and K. D. Raeder, 1999: Singular-vector perturbation growth in a primitive equation model with moist physics. *J. Atmos. Sci.*, **56**, 1627–1648, doi:10.1175/1520-0469(1999)056<1627:SVPGIA>2.0.CO;2.

Errico, R. M., D. J. Stensrud, and K. D. Raeder, 2001: Estimation of the error distributions of precipitation produced by convective parametrization schemes. *Quart. J. Roy. Meteor. Soc.*, **127**, 2495–2512, doi:10.1002/qj.49712757802.

Errico, R. M., P. Bauer, and J.-F. Mahfouf, 2007: Issues regarding the assimilation of cloud and precipitation data. *J. Atmos. Sci.*, **64**, 3785–3798, doi:10.1175/2006JAS2044.1.

Eyink, G. L., and S. Kim, 2006: A maximum entropy method for particle filtering. *J. Stat. Phys.*, **123**, 1071–1128, doi:10.1007/s10955-006-9124-9.

Falkovich, A., E. Kalnay, S. Lord, and M. B. Mathur, 2000: A new method of observed rainfall assimilation in forecast models. *J. Appl. Meteor.*, **39**, 1282–1298, doi:10.1175/1520-0450(2000)039<1282:ANMOOR>2.0.CO;2.

Gelaro, R., R. H. Langland, S. Pellerin, and R. Todling, 2010: The THORPEX observation impact intercomparison experiment. *Mon. Wea. Rev.*, **138**, 4009–4025, doi:10.1175/2010MWR3393.1.

Greybush, S. J., E. Kalnay, T. Miyoshi, K. Ide, and B. R. Hunt, 2011: Balance and Ensemble Kalman Filter Localization Techniques. *Mon. Wea. Rev.*, **139**, 511–522, doi:10.1175/2010MWR3328.1.

Guttman, N. B., 1999: Accepting the Standardized Precipitation Index: A calculation algorithm. *JAWRA J. Amer. Water Resour. Assoc.*, **35**, 311–322, doi:10.1111/j.1752-1688.1999.tb03592.x.

Hamill, T. M., and J. Juras, 2006: Measuring forecast skill: is it real skill or is it the varying climatology? *Quart. J. Roy. Meteor. Soc.*, **132**, 2905–2923, doi:10.1256/qj.06.25.

Hotta, D., E. Kalnay, Y. Ota, and T. Miyoshi, 2013: Ensemble forecast sensitivity to observations (EFSO) and proactive quality control. *Second Annual CICS-MD Science Meeting*, College Park, MD, Cooperative Institute for Climate & Satellites-Maryland.

Hou, A. Y., S. Q. Zhang, and O. Reale, 2004: Variational continuous assimilation of TMI and SSM/I rain rates: Impact on GEOS-3 hurricane analyses and forecasts. *Mon. Wea. Rev.*, **132**, 2094–2109, doi:10.1175/1520-0493(2004)132<2094:VCAOTA>2.0.CO;2.

Hou, A. Y., G. Skofronick-Jackson, C. D. Kummerow, and J. M. Shepherd, 2008: Chapter 6: Global precipitation measurement. *Precipitation: Advances in Measurement, Estimation and Prediction*, Springer, 131–164.

Huffman, G., R. Adler, D. Bolvin, and E. Nelkin, 2010: The TRMM Multi-Satellite Precipitation Analysis (TMPA). *Satellite Rainfall Applications for Surface Hydrology*, M. Gebremichael and F. Hossain, Eds., Springer Netherlands, 3–22.

Huffman, G. J., and D. T. Bolvin, 2013: *TRMM and other data precipitation data set documentation*. Laboratory for Atmospheres, NASA Goddard Space Flight Center and Science Systems and Applications.

Huffman, G. J. and Coauthors, 2007: The TRMM Multisatellite Precipitation Analysis (TMPA): Quasi-global, multiyear, combined-sensor precipitation estimates at fine scales. *J. Hydrometeor.*, **8**, 38–55, doi:10.1175/JHM560.1.

Hunt, B. R., E. J. Kostelich, and I. Szunyogh, 2007: Efficient data assimilation for spatiotemporal chaos: A local ensemble transform Kalman filter. *Physica D*, **230**, 112–126, doi:10.1016/j.physd.2006.11.008.

Ide, K., P. Courtier, M. Ghil, and A. C. Lorenc, 1997: Unified notation for data assimilation : Operational, sequential and variational. *J. Meteor. Soc. Jpn.*, **75**, 181–189.

Jones, P. D., and R. S. Bradley, 1992: Chapter 13: Climatic variations in the longest instrumental records. *Climate Since A.D. 1500*, Routledge, London, 246–268.

Kalnay, E., and S.-C. Yang, 2010: Accelerating the spin-up of Ensemble Kalman Filtering. *Quart. J. Roy. Meteor. Soc.*, **136**, 1644–1651, doi:10.1002/qj.652.

Kalnay, E., H. Li, T. Miyoshi, S.-C. Yang, and J. Ballabrera-Poy, 2007: Response to the discussion on "4-D-Var or EnKF?" by Nils Gustafsson. *Tellus A*, **59**, 778–780, doi:10.3402/tellusa.v59i5.15171.

Kalnay, E., Y. Ota, T. Miyoshi, and J. Liu, 2012: A simpler formulation of forecast sensitivity to observations: application to ensemble Kalman filters. *Tellus A*, **64**, 18462, doi:10.3402/tellusa.v64i0.18462.

Kang, J.-S., E. Kalnay, J. Liu, I. Fung, T. Miyoshi, and K. Ide, 2011: "Variable localization" in an ensemble Kalman filter: Application to the carbon cycle data assimilation. *J. Geophys. Res.*, **116**, D09110, doi:201110.1029/2010JD014673.

Kleist, D. T., 2012: An evaluation of hybrid variational-ensemble data assimilation for the NCEP GFS. University of Maryland, 149 pp.

Kleist, D. T., D. F. Parrish, J. C. Derber, R. Treadon, W.-S. Wu, and S. Lord, 2009: Introduction of the GSI into the NCEP Global Data Assimilation System. *Wea. Forecasting*, **24**, 1691–1705, doi:10.1175/2009WAF2222201.1.

Koizumi, K., Y. Ishikawa, and T. Tsuyuki, 2005: Assimilation of precipitation data to the JMA mesoscale model with a four-dimensional variational method and its impact on precipitation forecasts. *Sola*, **1**, 45–48, doi:10.2151/sola.2005-013.

Kucharski, F., F. Molteni, M. P. King, R. Farneti, I.-S. Kang, and L. Feudale, 2013: On the need of intermediate complexity general circulation models: A

"SPEEDY" example. *Bull. Amer. Meteor. Soc.*, **94**, 25–30, doi:10.1175/BAMS-D-11-00238.1.

Langland, R. H., and N. L. Baker, 2004: Estimation of observation impact using the NRL atmospheric variational data assimilation adjoint system. *Tellus A*, **56**, 189–201, doi:10.1111/j.1600-0870.2004.00056.x.

Van Leeuwen, P. J., 2009: Particle filtering in geophysical systems. *Mon. Wea. Rev.*, **137**, 4089–4114, doi:10.1175/2009MWR2835.1.

Leon, D. C., Z. Wang, and D. Liu, 2008: Climatology of drizzle in marine boundary layer clouds based on 1 year of data from CloudSat and Cloud-Aerosol Lidar and Infrared Pathfinder Satellite Observations (CALIPSO). *J. Geophys. Res.*, **113**, D00A14, doi:10.1029/2008JD009835.

Li, H., E. Kalnay, and T. Miyoshi, 2009: Simultaneous estimation of covariance inflation and observation errors within an ensemble Kalman filter. *Quart. J. Roy. Meteor. Soc.*, **135**, 523–533, doi:10.1002/qj.371.

Li, H., J. Liu, and E. Kalnay, 2010: Correction of "Estimating observation impact without adjoint model in an ensemble Kalman filter." *Quart. J. Roy. Meteor. Soc.*, **136**, 1652–1654, doi:10.1002/qj.658.

Li, X., and J. R. Mecikalski, 2010: Assimilation of the dual-polarization Doppler radar data for a convective storm with a warm-rain radar forward operator. *J. Geophys. Res.*, **115**, D16208, doi:10.1029/2009JD013666.

Li, X., and J. R. Mecikalski, 2012: Impact of the dual-polarization Doppler radar data on two convective storms with a warm-rain radar forward operator. *Mon. Wea. Rev.*, **140**, 2147–2167, doi:10.1175/MWR-D-11-00090.1.

Liu, J., and E. Kalnay, 2008: Estimating observation impact without adjoint model in an ensemble Kalman filter. *Quart. J. Roy. Meteor. Soc.*, **134**, 1327–1335, doi:10.1002/qj.280.

Lopez, P., 2011: Direct 4D-Var assimilation of NCEP stage IV radar and gauge precipitation data at ECMWF. *Mon. Wea. Rev.*, **139**, 2098–2116, doi:10.1175/2010MWR3565.1.

Lopez, P., 2013: Experimental 4D-Var assimilation of SYNOP rain gauge data at ECMWF. *Mon. Wea. Rev.*, **141**, 1527–1544, doi:10.1175/MWR-D-12-00024.1.

Lopez, P., and E. Moreau, 2005: A convection scheme for data assimilation: Description and initial tests. *Quart. J. Roy. Meteor. Soc.*, **131**, 409–436, doi:10.1256/qj.04.69.

Lorenz, E. N., and K. A. Emanuel, 1998: Optimal sites for supplementary weather observations: Simulation with a small model. *J. Atmos. Sci.*, **55**, 399–414, doi:10.1175/1520-0469(1998)055<0399:OSFSWO>2.0.CO;2.

Maggioni, V., M. Sapiano, R. Adler, Y. Tian, and G. Huffman, 2013: An error model for uncertainty quantification in high-time resolution precipitation products. *EGU General Assembly 2013*, Vienna, Austria, European Geosciences Union.

Mahfouf, J., B. Brasnett, and S. Gagnon, 2007: A Canadian precipitation analysis (CaPA) project: Description and preliminary results. *Atmosphere-Ocean*, **45**, 1–17, doi:10.3137/ao.v450101.

McKee, T. B., N. J. Doesken, and J. Kleist, 1993: The relationship of drought frequency and duration to time scales. *Proc. 8th Conference on Applied Climatology*, Boston, MA, American Meteorological Society, 179–183.

Mesinger, F. and Coauthors, 2006: North American Regional Reanalysis. *Bull. Amer. Meteor. Soc.*, **87**, 343–360, doi:10.1175/BAMS-87-3-343.

Miyoshi, T., 2005: Ensemble Kalman filter experiments with a primitive-equation global model. University of Maryland, 197 pp.

Miyoshi, T., 2011: The Gaussian approach to adaptive covariance inflation and its implementation with the local ensemble transform Kalman filter. *Mon. Wea. Rev.*, **139**, 1519–1535, doi:10.1175/2010MWR3570.1.

Miyoshi, T., and K. Aranami, 2006: Applying a four-dimensional Local Ensemble Transform Kalman Filter (4D-LETKF) to the JMA Nonhydrostatic Model (NHM). *Sola*, **2**, 128–131, doi:10.2151/sola.2006-033.

Molteni, 2003: Atmospheric simulations using a GCM with simplified physical parametrizations. I: model climatology and variability in multi-decadal experiments. *Clim. Dyn.*, **20**, 175–191, doi:10.1007/s00382-002-0268-2.

Ota, Y., J. C. Derber, E. Kalnay, and T. Miyoshi, 2013: Ensemble-based observation impact estimates using the NCEP GFS. *Tellus A*, **65**, 20038, doi:10.3402/tellusa.v65i0.20038.

Reynolds, C. A., P. J. Webster, and E. Kalnay, 1994: Random error growth in NMC's global forecasts. *Mon. Wea. Rev.*, **122**, 1281–1305, doi:10.1175/1520-0493(1994)122<1281:REGING>2.0.CO;2.

Saha, S. and Coauthors, 2010: The NCEP Climate Forecast System Reanalysis. *Bull. Amer. Meteor. Soc.*, **91**, 1015–1057, doi:10.1175/2010BAMS3001.1.

Schöniger, A., W. Nowak, and H.-J. Hendricks Franssen, 2012: Parameter estimation by ensemble Kalman filters with transformed data: Approach and application

to hydraulic tomography. *Water Resour. Res.*, **48**, W04502, doi:10.1029/2011WR010462.

Simon, E., and L. Bertino, 2009: Application of the Gaussian anamorphosis to assimilation in a 3-D coupled physical-ecosystem model of the North Atlantic with the EnKF: a twin experiment. *Ocean Sci*, **5**, 495–510, doi:10.5194/os-5-495-2009.

Simon, E., and L. Bertino, 2012: Gaussian anamorphosis extension of the DEnKF for combined state parameter estimation: Application to a 1D ocean ecosystem model. *J. Mar. Syst.*, **89**, 1–18, doi:10.1016/j.jmarsys.2011.07.007.

Szunyogh, I., E. J. Kostelich, G. Gyarmati, E. Kalnay, B. R. Hunt, E. Ott, E. Satterfield, and J. A. Yorke, 2008: A local ensemble transform Kalman filter data assimilation system for the NCEP global model. *Tellus A*, **60**, 113–130, doi:10.3402/tellusa.v60i1.15270.

Tian, Y., and C. D. Peters-Lidard, 2010: A global map of uncertainties in satellite-based precipitation measurements. *Geophys. Res. Lett.*, **37**, L24407, doi:10.1029/2010GL046008.

Tian, Y. and Coauthors, 2009: Component analysis of errors in satellite-based precipitation estimates. *J. Geophys. Res.*, **114**, D24101, doi:10.1029/2009JD011949.

Treadon, R. E., H.-L. Pan, W.-S. Wu, Y. Lin, W. S. Olson, and R. J. Kuligowski, 2003: Global and regional moisture analyses at NCEP. *Proc. ECMWF/GEWEX Workshop on Humidity Analysis*, Reading, United Kingdom, ECMWF, 33–48.

Tsuyuki, T., 1996: Variational data assimilation in the tropics using precipitation data. Part II: 3D model. *Mon. Wea. Rev.*, **124**, 2545–2561, doi:10.1175/1520-0493(1996)124<2545:VDAITT>2.0.CO;2.

Tsuyuki, T., 1997: Variational data assimilation in the tropics using precipitation data. Part III: Assimilation of SSM/I precipitation rates. *Mon. Wea. Rev.*, **125**, 1447–1464, doi:10.1175/1520-0493(1997)125<1447:VDAITT>2.0.CO;2.

Tsuyuki, T., and T. Miyoshi, 2007: Recent progress of data assimilation methods in meteorology. *J. Meteor. Soc. Jpn.*, **85B**, 331–361, doi:10.2151/jmsj.85B.331.

vanZanten, M. C., B. Stevens, G. Vali, and D. H. Lenschow, 2005: Observations of drizzle in nocturnal marine stratocumulus. *J. Atmos. Sci.*, **62**, 88–106, doi:10.1175/JAS-3355.1.

Wackernagel, H., 2003: *Multivariate Geostatistics*. Springer, 408 pp.

Wang, X., D. Parrish, D. Kleist, and J. Whitaker, 2013: GSI 3DVar-based ensemble-variational hybrid data assimilation for NCEP Global Forecast System: Single-resolution experiments. *Mon. Wea. Rev.*, **141**, 4098–4117, doi:10.1175/MWR-D-12-00141.1.

Weygandt, S. S., S. G. Benjamin, T. G. Smirnova, and J. M. Brown, 2008: Assimilation of radar reflectivity data using a diabatic digital filter within the Rapid Update Cycle. *12th Conference on IOAS-AOLS*, New Orleans, LA, American Meteorological Society.

Whitaker, J. S., T. M. Hamill, X. Wei, Y. Song, and Z. Toth, 2008: Ensemble data assimilation with the NCEP Global Forecast System. *Mon. Wea. Rev.*, **136**, 463–482, doi:10.1175/2007MWR2018.1.

Yang, S.-C., E. Kalnay, and B. R. Hunt, 2012: Handling nonlinearity in an ensemble Kalman filter: Experiments with the three-variable Lorenz model. *Mon. Wea. Rev.*, **140**, 2628–2646, doi:10.1175/MWR-D-11-00313.1.

Zhang, F., C. Snyder, and J. Sun, 2004: Impacts of initial estimate and observation availability on convective-scale data assimilation with an ensemble Kalman filter. *Mon. Wea. Rev.*, **132**, 1238–1253, doi:10.1175/1520-0493(2004)132<1238:IOIEAO>2.0.CO;2.

Zhang, S. Q., M. Zupanski, A. Y. Hou, X. Lin, and S. H. Cheung, 2013: Assimilation of precipitation-affected radiances in a cloud-resolving WRF ensemble data assimilation system. *Mon. Wea. Rev.*, **141**, 754–772, doi:10.1175/MWR-D-12-00055.1.

Zupanski, D., and F. Mesinger, 1995: Four-dimensional variational assimilation of precipitation data. *Mon. Wea. Rev.*, **123**, 1112–1127, doi:10.1175/1520-0493(1995)123<1112:FDVAOP>2.0.CO;2.

Zupanski, D., S. Q. Zhang, M. Zupanski, A. Y. Hou, and S. H. Cheung, 2011: A prototype WRF-based ensemble data assimilation system for dynamically downscaling satellite precipitation observations. *J. Hydrometeor.*, **12**, 118–134, doi:10.1175/2010JHM1271.1.